Characterizing Heterogeneous Defect Structures in Spinel Oxides Disordered *via* Extreme Conditions

A Dissertation Presented for the

Doctor of Philosophy

Degree

The University of Tennessee, Knoxville

John Michael Hirtz

December 2025

ACKNOWLEDGMENTS

The research presented in this dissertation would not be possible without the effort of collaborators who contributed above and beyond with long hours and fruitful discussion particularly: Eric O'Quinn, Matthew Tucker, Guido Baldonozzi, Yuanpeng Zhang, Joerg Neuefeind, Michelle Everette, Dayton Kizzire, Maksim Eremenko, Emily Van Auken, Malcom Guthrie, Bianca Haberl, Arianna Minelli, Zachary Morgen, Christina Trautmann, Antonio M. dos Santos, Huibo Cao, and Feng Ye. I would especially like to thank my advisor Dr. Maik Lang for his guidance and support, as well as, fostering invaluable research opportunities and collaborations. I also thank my committee members, Kurt Sickafus, Matthew Tucker, Eric O'Quinn, and Steven Zinkle. Thank you to Matthew Tucker and the diffraction section, as well as, Reinhard Boehler for being so welcoming during my fellowships and internships at Oak Ridge National Laboratory. I've had the pleasure to work alongside many colleagues particularly Cale Overstreet, Jacob Minette, George Adamson, Igor Gussev, William Reed, Kenneth Sanders, Eric Kadel, Savannah Watson, Pradyumna Parshi, Alex Solomon, Will Cureton, Jackson Cagle, Casey Corbridge, Mason King, Zachary Chaney, Evan Williams, Patrick Huston, Devon Drey, Will Gardner, Casey MacDonald-Risner, and Katherine Parker-Repsher. Additionally, I'd like to thank my friends in Knoxville for the many, many free rides to the airport and house sitting, especially Rachel Incorvati, Finally, I'd like to thank my parents Greg and Sara Hirtz and my family for their unconditional help and support. This work would not have been completed without the help of all mentioned here.

This research was supported by: The U.S. Department of Energy, Office of Science, Basic Energy Sciences under Award #DE-SC0020321, DOE/NNSA and the Chicago / DOE Alliance Center through cooperative agreement DE-NA0003975, Department of Energy (DOE) Office of Nuclear Energy's Nuclear Energy University Program (NEUP) under US-DOE, contract DE-NE0008895, Graduate Advancement and Training Education fellowship provided by The Science Alliance, which is a Tennessee Higher Education Commission Center of Excellence administered by The University of Tennessee–Oak Ridge Innovation Institute. Some results presented here were performed at the X0-beamline of the UNILAC at the GSI Helmholtzzentrum für Schwerionenforschung, Darmstadt (Germany) in the frame of FAIR Phase-0. This research used resources at the Spallation Neutron Source a DOE Office of Science User Facility operated by the Oak Ridge National Laboratory. The beam time was allocated to NOMAD, CORELLI, and SNAP on proposal numbers IPTS-35763, IPTS-28343, IPTS-31950, IPTS-33112, IPTS-16464, IPTS-14164, IPTS-11800.

ABSTRACT

The development of advanced energy technologies requires carefully designed materials for use in harsh operating conditions, such as high temperatures, high pressures, and extreme radiation fields. Complex oxides are promising candidate materials for use in such advanced energy technologies; however, they are prone to disorder and defects which form during exposure to these extremes. Over time, such structural modifications build up and modify the properties of materials and eventually lead to their degradation. Thus, understanding the underlying atomic-scale mechanisms of defect formation is essential to, not only predict how these materials degrade, but also to develop new, more robust materials. Using neutron total scattering, both the long-range coherent structure and the local atomic arrangements can be measured simultaneously, with high sensitivity to both cations and anions; this presents a great advantage over more conventional characterization techniques. Neutron scattering has been used to analyze the unique local defect structures in spinel disorder through high temperature and through intense ionizing irradiation. Preliminary work was also performed, to expand this scattering technique to enable the study of materials disordered through high pressure.

TABLE OF CONTENTS

LIST OF TABLES

LIST OF FIGURES

Chapter 1

Introduction

Overview

Complex oxides that adopt the spinel (AB_2O_4) structure are used in numerous engineering applications due to favorable physical, magnetic[1], electronic[2], optical[3] and catalytic[4] properties. For these reasons, spinel oxides are employed in a wide range of devices for data storage[5], dielectrics[6], transparent conductors[7], and lasers[8], as well as, catalysts[9] for chemical reactions and protective coatings[10]. Spinel oxides are also important metamorphic minerals where these properties can affect mantle physics[11]. In many of these environments, spinel is exposed to extreme conditions and understanding how they degrade is vitally important for their prospective use and behavior.

These physics properties, however, are dependent on the intrinsic amount of disorder present in the spinel oxide. Spinels are able to accommodate large amounts of disorder through cation anti-site defects, commonly referred to as inversion, where the A site cation occupies the B site and vice versa[12]. There is a great interest, therefore, in characterizing the amount of inversion in a spinel sample, and how the cation distribution changes when exposed to operating environments. Designing experiments to measure *in situ* changes in inversion has proven difficult for many spinel compositions, like $MgAl_2O_4$, where the A and B cations have similar atomic numbers. Traditional techniques like x-ray diffraction are unable to distinguish between similar cations and perform poorly on materials with low electron densities like complex oxides. Other methods that measure secondary phenomena like electric resistivity[13] or oxygen position[14] were used to approximate inversion with moderate success. Using neutron diffraction, which is sensitive

to the nuclear structure, the number of anti-site defects in spinel samples disordered through various means could be characterized[15].

Previous thermodynamic studies have noted that the disordering process in spinel may be more complex as there is a high likelihood that ionic inverse spinels would display some amount of short range ordering[16]. Phase transformations as a result of this ordering have been reported for some spinel compositions[17], but a unified model that covers all inversion in the 2-3 spinel system has not been experimentally determined and tested. Using neutron total scattering, both the long-range repeating structure and the local cation arrangements can be measured simultaneously for the spinel type mineral $MgAl_2O_4$. Using this method to collect data from spinel samples disorder through high temperature, high pressure, and coupled extreme conditions, it would be possible to determine and compare the local ordering in each instance.

The Spinel Crystal Structure

The spinel crystal structure, determined independently by Bragg[18] and Nishikawa[19] in 1915, has a cubic unit cell consisting of 8 formula units which form an alternating pattern of A_2O_4 and B_4O_4 building blocks. The resulting crystal structure is described by the cubic $Fd\bar{3}m$ space group with the anions on the 32*e* Wyckoff site in a pseudo-cubic close-packed (ccp) configuration, A-cations on the 8*a* site in tetrahedral coordination with oxygen, and B cations on the 16*b* site in octahedral coordination. This configuration can be imagined as a 2x2x2 superstructure of rocksalt ($Fm\bar{3}m$) that contains cations in tetrahedral coordination and ordered cation vacancies (16*c*). The spinel structure is fully described by only 3 structural parameters: (*1*) the size of the unit cell, determined by the unit-cell

parameter, *a*, (*2*) the anion distortion away from an ideal cubic close packing configuration given by the anion parameter, *u*, and (*3*) the degree of cation disorder in the structure assessed by the inversion parameter, *i*.[20]

The process by which increasing disorder is accommodated in the spinel structure is through the exchange of the two cations between the A and B sites (cation antisite defects). The inversion parameter (*i*) quantifies the degree of disorder and is defined by the fractional occupancy of the A site by B cations. Thus, the fractional occupancy of each cation site by each cation species can be represented solely by the inversion parameter:

$$(A_{1-i}B_i)\left(B_{1-i/2}\,A_{i/2}\right)_2 O_4 \qquad \text{[Eq 1]}$$

Perfect fully ordered, "normal" spinels have an inversion parameter of $i = 0$ with all A-sites occupied by A-cations and all B-sites occupied by B-cations, while completely "inverse" spinels have an inversion parameter of $i = 1.0$ with all A-sites occupied with B-cations and a random distribution of cations across the B-sites. A fully disordered spinel has an inversion of $i = 0.67$, with a random distribution of the two cations amongst the two available sites. The cation exchange also influences the anion parameter due to the size difference of the replaced cations; the size mismatch causes the anion to relax along the <111> direction.

Disordering Mechanisms

High Temperature

The high melting point, chemical stability, and strength of $MgAl_2O_4$ make it a favorable material for use as coatings[21], windows[22], and catalysts[23] for high temperature applications. These chemical and physical properties, however, can be altered by the slight changes in unit cell and polyhedral size caused by the formation of anti-site defects at temperature. These same changing properties are also of interest in geosciences as $MgAl_2O_4$ is an important metamorphic mineral[11], which is found within the earth's mantle under a wide range of temperature conditions. Thus, there is an interest in understanding the details of cation inversion and disordering at high temperatures.

Early studies on $MgAl_2O_4$ spinel at high temperature used a myriad of techniques to determine the occupancy changes of Magnesium and Aluminum at their respective sites, due to the similar scattering strength of Magnesium and Aluminum to X-ray diffraction. Specifically, nuclear magnetic resonance on quenched samples and electric resistivity measurements were used. Early electric resistivity results by Suzuki[24] (1980) and Weeks and Sonder [13] (1980), were the first to show a change in behavior around 600 °C and equated it to a potential phase transition. Although unable to measure the cation partitioning, Yamanaka and Takeuchi[14] (1983) reported changes to the oxygen position and thermal expansion of $MgAl_2O_4$ starting in the same temperature region. The procedure for determining the fractional occupancies of Magnesium and Aluminum using nuclear magnetic resonance was outline by Gobbi[25] (1985) and demonstrated on a synthetic and

natural spinel sample. The use of NMR was then expanded by Wood[26] (1986) which measured the amount of inversion in rapidly quenched synthetic $MgAl_2O_4$ samples between 700°C and 900°C.

These early high temperature crystallographic studies were performed to confirm earlier Calorimetry work. A thermodynamic treatment in simple spinel for determining cation distribution was presented by Callen[27] (1956) and refined by Navrotsky and Kleppa[28] (1967), which represented spinel as a simple chemical equilibrium where the entropy change from disordering is equated to only configuration entropy. The model was further updated by O'Neill and Navrotsky[16] (1983) to instead use lattice energy, which could be determined simply by chemical composition and inversion using Shannon[29] ionic radii. Both models, although successful with other compositions, were unable to completely capture the inversion behavior of $MgAl_2O_4$, which was understood at the time to plateaued at low and high temperatures with a dramatic increase between 600℃ and 900℃. It was unclear whether these differences were a result of kinetic factors, a second-order phase transition, or short-range ordering.

These inconsistencies in the behavior of $MgAl_2O_4$ at high temperature were predominately a result of the experimental techniques used to measure inversion. The cation distribution of $MgAl_2O_4$ as a function of temperature between 600℃ and 1000℃ was successfully measured *in situ* using neutron diffraction by Peterson[15] (1991). The temperature range was then expanded in a similar experiment by Redfern[30] (1999) to 300℃ to 1900℃, which accurately measured the change in inversion in $MgAl_2O_4$ spinel at high temperature. In synthetic spinel samples, the level of inversion is dependent on the

synthesis conditions and particularly the heat treatment.[31] During the first heating cycle, the cation anti-site defects in the highly disordered precursor material are annealed until the temperature is sufficiently high to induce subsequent disordering. In the "normal" $MgAl_2O_4$ spinel, for example, cation inversion increases linearly with temperature above 600°C, until a random distribution of cations across both sites is achieved ($i = 0.67$). When slowly cooled, the inversion in $MgAl_2O_4$ is reduced in the same linear manner with temperature until 600°C, below which inversion no longer changes upon further cooling.[30] An inverted behavior is observed for "inverse" spinels with $i > 0.67$, heating above a critical temperature leads to a reduction of inversion until full randomization of cations is reached ($i = 0.67$). An example is the "inverse" $NiAl_2O_4$ spinel, with a high degree of quenched disorder from the synthesis process ($i \sim 0.8$-0.9). During heating, the amount of inversion in the sample begins to decrease above 800°C, where cation diffusion becomes sufficiently high to allow for cation exchange towards a fully random distribution.[32, 33]

With the cation distribution as a function of temperature in $MgAl_2O_4$ determined, the discrepancy between the amount of inversion predicted by thermodynamic studies and the amount that is measured should be reexamined. The prediction that $MgAl_2O_4$ undergoes a second order phase transition at 600℃ that ends at 900℃ is unlikely as the high temperature plateau at 900℃ was shown to be a result of *ex situ* measurements that relied on quenching inversion to room temperature. The plateau at low temperature and the sharp increase at 600℃, however, are still present in the *in situ* neutron diffraction data. Further work needs to be performed, to understand the role of local cation ordering and kinetics to this low temperature behavior of $MgAl_2O_4$ spinel oxide.

High Pressure

As an important aluminum containing geologic mineral, the pressure response of spinel is as important as the high temperature behavior in understanding seismic discontinuities in mantle physics[34]. This necessitates understanding potential phase transitions, as well as, the compressibility of spinel structures, which is dependent on the amount of cation disorder present in the crystal. Thus, there has been significant interest in the geological community to determine the pressure response of spinel oxides.

Early high-pressure studies of the type mineral $MgAl_2O_4$ were prompted by observed seismic discontinuities at depths of 400 km and 650 km. The 400 km discontinuity was determined to be associated with the olivine-spinel phase transformation[34]; therefore, the 650 km discontinuity was proposed to be related to further phase transformations in spinel. These high-pressure studies found that $MgAl_2O_4$ decomposes at high pressure into the simple oxides periclase (MgO) and corundum (Al_2O_3) above ~13 GPa at high temperatures[35]. Disproportionation in spinel is common in aluminates and has been reported in $MnAl_2O_4$, $FeAl_2O_4$, $CoAl_2O_4$ and $NiAl_2O_4$[36]; however, chromate spinel have been reported to have increased stability at high pressure in DFT studies[37].

Further transformations to a dense spinel structure with an orthorhombic unit cell was predicted by Reid[38] (1969) after shock wave data at pressures greater than 68 GPa determined that spinel transforms into phases more dense than the mixed oxides[39]. This structure was first measured under static compression by Liu[40] (1978). The high-pressure

phase was then confirmed to be the $CaFe_2O_4$ structure through high pressure *in situ* x-ray diffraction and TEM[41].

The influence of inversion on these high-pressure processes in $MgAl_2O_4$, however, was not well understood. Due to the difficulty in measuring inversion with conventional high pressure techniques, including Raman spectroscopy and synchrotron X-ray diffraction. Early studies, therefore, relied on measuring the oxygen parameter u to estimate the cation partitioning at pressure using a linear relationship measured in high temperature studies. The first *in situ* XRD study in a diamond anvil cell (DAC) up to 4 GPa at room temperature by Finger[42] (1986) found a slight increase in inversion with pressure. Similar studies by Pavese[43] (1999), Levy[44] (2003), Kudoh[45] (2007), and Nestola[46] (2007), however, found that inversion either slightly decreased or did not follow any statistically significant trend. The insignificant effect of high pressure on inversion in $MgAl_2O_4$ is caused by the inability of cation anti-site defects to drastically change the unit cell parameter of the crystal due to the similar ionic radii of Magnesium and Aluminum[26]. This behavior may be altered by heating $MgAl_2O_4$ at pressure where significant increases in inversion were reported at 2.6 GPa and 1600 K[47]. Further studies are required to determine the effect of coupling extreme pressure and temperature on the cation distribution in $MgAl_2O_4$.

Swift Heavy Ion Irradiation

$MgAl_2O_4$ has been considered for deployment as an advanced nuclear ceramic due to its structural, mechanical, optical, and electrical properties. Nuclear ceramics are proposed to be used as waste forms, transmutation matrices, optical and RF windows, and as electrical insulators. In these applications spinel would be exposed to high temperature,

high stresses, and intense irradiation fields. Understanding the radiation resistance of spinel to multiple forms of radiation is crucial for ensuring its safety and reliability.

Spinel's potential use as a structural ceramic in fusion applications has led to a significant body of work on its response to high doses of thermal and fast neutron irradiation. Studies at HFIR and EBRII reported strong amorphization resistance in stoichiometric and non-stoichiometric $MgAl_2O_4$[48-50]. Damage to the crystal structure is preferentially accommodated through vacancy-interstitial recombination preventing the formation of significant extended defects. The result is negligible swelling in single crystals with slight swelling being reported in polycrystalline samples, which are shown in TEM to stem from planar arrays of voids adjacent to grain boundaries[50]. Under extreme neutron doses inversion increases drastically with measured ranges of i = 0.59 to i = 0.69 in samples irradiated to 53 and 249 dpa, respectively[51].

The resistance of spinel to neutrons and low energy ions, however, is temperature dependent. Yu *et al.*[52] (1994) found for the first time that after irradiation with low energy ions at 100-120 ℃, spinel amorphized after a transformation to a potential metastable phase. This result was repeated in a non-stoichiometric sample by Devanathan (1995)[53]. Changing the stoichiometry improved amorphization resistance, but the phase transformation, previously reported, still occurred[54]. The phase was then studied using transmission electron microscopy by Ishimaru[55] (2000) and determined to be a disordered rock salt phase. In this metastable phase, the oxygen relax to an ideal cubic close packed lattice and the tetrahedral A site cation migrates to the *16c* octahedral vacant site. The resulting structure, therefore, appears to be a defect NaCl rock salt structure with cations, and

vacancies, randomly occupying *16d* and *16c* octahedral sites in the $Fd\bar{3}m$ structure. This increase in symmetry changes the space group to $Fm\bar{3}m$ and halves the unit cell parameter.

Spinel oxide has also been proposed as a potential inert matrix fuel (IMF) for the transmutation of minor actinides and burning ^{239}Pu[56]. In this application the spinel structure would not only need to be highly resistant to neutron irradiation, but also, the swift heavy ions produced from fission. Neutron irradiation and low-energy ions lose energy in a material through nuclear interactions. This mechanism directly knocks atoms in a material off their lattice positions creating large cascades of interstitials and vacancies[57]. Instead, swift heavy ions (~1 Mev u^{-1}) interact with matter through electronic mechanisms. These ions deposit substantial energy into the electronic subsystem of a material over sub-picosecond timescales. The transfer of energy causes electron excitation and ionization processes, which can drastically heat the atomic lattice through electron-phonon coupling[58]. This intense localized heating can form cylindrical tracks of a few nanometers in diameter containing point defects, phase-phase transformations[59] and crystalline-amorphous transformations[60] along the path of the ion [58].

The response of spinel to swift heavy ions deviates significantly from previous work using neutrons and low energy ions. Significant unit cell swelling was measured for single crystals exposed to high fluences (10^{16}) of 72 MeV Iodine ions[61]. At higher ion energies amorphization, volumetric expansions of 35%, and metastable phase formation were characterized with TEM[62]. This metastable phase was determined to resemble the defective rock salt structure previously only reported in low temperature irradiations[63]. The formation of the defective rock salt phase after room temperature irradiation, however, was

actively debated in literature[64, 65]. The measurement of the rock salt structure is reported to be dependent on the measurement technique. For example, spinel which had been confirmed to transform into defective rock salt through x-ray diffraction has been shown to still resemble a spinel structure locally when measured through Raman spectroscopy[66]. Therefore, in order to completely describe the structure of spinel oxides disordered through extreme conditions a technique sensitive to more than the average structure is required.

Local Cation Ordering in Spinel

The potential for local cation ordering in inverse spinel oxides is often discussed in thermodynamic studies[16, 26]. In the inverse structure, two unique cations both occupy the same octahedrally coordinated *16d* Wyckoff position; therefore, if the two cations are significantly dissimilar in size or oxidation state, it would be expected that the *16d* site would split into two unique sites that could accommodate each cation individually. It has been reported that with decreasing temperature highly ionic 4-2 spinels undergo a phase transition to a tetragonal $P4_322$ structure with two non-equivalent octahedral sites[67]. The transition temperature for the phase change was found to be depended on the ionic radii of the A and B site cations with the highest reported temperature being 770℃ for Mn_2TiO_4[68].

The formation of this long range tetragonal phase transition in these highly ionic 4-2 spinels is often cited as evidence for local ordering in less ionic 2-3 spinel oxides, which was used to explain discrepancies between the residual entropy deduced from phase equilibrium experiments and spectroscopic measurements on $MgAl_2O_4$[26]. Raman spectroscopy experiments on "inverse" 2-3 spinels ($NiAl_2O_4$ and $NiFe_2O_4$) revealed a greater number of active Raman modes than allowed for the $Fd\bar{3}m$ space group,[17, 69] which

is indicative of a lower symmetry space group. A proposed lower symmetry structure, tetragonal $P4_122$, was shown to be the lowest energy configuration for "inverse" spinel by DFT calculations.[70] This $P4_122$ structure is the chiral pair of the $P4_322$ structure. Distinguishing between these two structures is very difficult with most characterization techniques and contemporary sources denote only the $P4_122$ structure when referencing local ordering in spinel.

Neutron total scattering experiments with pair distribution function (PDF) analysis performed by O'Quinn *et al.*[71] provided direct insight into the atomic arrangement of ordered and disordered spinels in the $Mg_xNi_{1-x}Al_2O_4$ series with high sensitivity to both cation anti-site defects and oxygen sublattice relaxations. The local structure of the analyzed spinel compositions were best modeled by two distinct phases (with varying fractions): (*1*) ordered, "normal" spinel ($Fd\bar{3}m$), with A and B cations on the A- and B-sites, respectively, and (*2*) disordered, "inverse" spinel ($P4_122$)[71], which was also shown in XANES experiments performed on a similar chemical series.[72] The local atomic configuration in disordered spinels and the associated phase change were explained as a direct consequence of Pauling's 1st and 2nd rules.[73, 74] The $P4_122$ tetragonal structure was also shown to be the ground state of highly ionic inverse spinels.[75] The relative fraction of the tetragonal phase across the short-range was shown to scale directly with the inversion parameter, *i*, at the long-range, and the latter can be understood as a consequence of the atomic rearrangements. Interestingly, the long-range structure does not show any evidence of the local tetragonal phase, which implies that disorder in spinel is heterogeneous across different length scales with a higher degree of order locally then suggested by the long-

range behavior and cation exchange mechanism. This structural heterogeneity, which explains the discrepancy in previous studies, must be considered for a full description of physical properties in spinels[76] and contributes to an improved understanding of local cation ordering in complex oxides in general.[75]

Summary

This dissertation reports the results of studies on the local structure of disordered spinel oxides with a focus on the $MgAl_2O_4$ - $NiAl_2O_4$ chemical solution series studied through neutron total scattering techniques. The experimental methods used to this end are described in Chapter 2. A note on previous discrepancies in the proposed space group of spinels is presented in Chapter 3 along with results of neutron single crystal diffraction performed on CORELLI at the SNS. The local structure of spinel *in situ* at high temperature is reported in Chapter 4. The response of the local structure of spinel to coupled extremes induced by swift heavy ion irradiation is covered in Chapter 5. Chapter 6 focuses on the small structural changes seen in the local structure of $Y_2Zr_2O_7$ defect fluorite during extreme compression. Included in the chapter is an expanded description of performing neutron total scattering at high pressure; the challenges involved, proposed experimental method, and an examination of the capabilities of the high pressure SNAP diffractometer at the Spallation Neutron Source (SNS). Finally, Chapter 7 presents conclusions and provides perspective into further avenues of study on the topic of disorder in 2-3 spinel oxides. The publications which have resulted from my graduate work in the Nuclear Engineering Department at the University of Tennessee are listed here:

[1] Hirtz, J.; O'Quinn, E. C.; Gussev, I. M.; Neuefeind, J. C.; Lang, M., Cation Short-Range Ordering of MgAl2O4 and NiAl2O4 Spinel Oxides at High Temperatures via In Situ Neutron Total Scattering. *Inorganic Chemistry* **2022,** *61* (42), 16822-16830. [77]

[2] Hirtz, J.; O'Quinn, E. C.; Gussev, I. M.; Neuefeind, J. C.; Lang, M., Local Defect Structure of $Mg_{1-x}Ni_xAl_2O_4$ Spinel Irradiated with Swift Heavy Ions Analyzed *via* Neutron Total Scattering. (***in preparation***)

[3] Hirtz, J.; Overstreet, C.; O'Quinn, E. C.; dos Santos, A. M.; Tucker, M. G.; Lang, M., Measuring Structural Heterogeneity at High Pressure: Neutron Total Scattering using the Spallation Neutrons and Pressure (SNAP) diffractometer at Oak Ridge National Laboratory. (***in preparation***)

[4] Chaney, D. Z.; Hirtz, J.; Williams, E.; Minnette, J.; Cureton, W. F.; O'Quinn, E. C.; Zhao, X.; Guo, X.; Matsuoka, T.; Koehler, M., Grain size dependence of thermally induced oxidation in zirconium carbide. *Journal of Materials Science* **2023,** *58* (6), 2439-2455.

[5] O'Quinn, E. C.; Hirtz, J. M.; Overstreet, C. C.; Cureton, W. F.; Gussev, I. M.; Solomon, A. P.; Toimil-Molares, M. E.; Lang, M. K., Neutron Total Scattering Analysis of Materials for the Nuclear Fuel Cycle. *Nuclear Science and Engineering* **2025**, 1-15.

[6] Adamson, G.; Hirtz, J.; Overstreet, C.; O'Quinn, E. C.; Kinsler-Fedon, C.; Simon, P.; Park, C.; Wang, X.; Liang, T.; Xu, H.; Keppens, V.; Page, K.; Lang, M., Influence of Compositional Complexity on Amorphization Resistance of Swift Heavy Ion Irradiated Titanate Pyrochlores. *Inorganic Chemistry* **2025** *(submitted)*

[7] Farraj, H.; Hirtz, J.; Sunariwal, N.; Ahart, M.; Lang, M.; Tucker, M. G.; Hemley, R. J.; Cabana, J., Short-Range Ordering in Li_2CoO_2F from X-ray and Neutron Scattering. ***(in preparation)***

Chapter 2

Experimental Methods

Pristine Sample Synthesis

The $Mg_xNi_{(1-x)}Al_2O_4$ samples were produced *via* the conventional solid-state synthesis route. The MgO, NiO, and Al_2O_3 powders were purchased from Alfa Aesar and mixed in the appropriate stoichiometric ratio:

$$MgO + Al_2O_3 \xrightarrow{yields} MgAl_2O_4 \quad \text{[Eq 2]}$$

$$NiO + Al_2O_3 \xrightarrow{yields} NiAl_2O_4 \quad \text{[Eq 3]}$$

The samples were heated, reground, and heated again to ensure a complete reaction, which can be confirmed by laboratory X-ray diffraction (XRD) experiments.[78, 79] The produced powders were used for the *in situ* heating study and the irradiation study.

Neutron Total Scattering Theory

The pristine and disordered samples generated for this research were characterized using neutron total scattering techniques. A total scattering experiment is performed to extract both the Bragg diffraction used to analyze the symmetry of a crystallite and diffuse sample scattering under the Bragg peaks, which are related to the local atomic arrangements. Accurately distinguishing between the diffuse scattering of the sample compared to the diffuse scattering of the sample container or instrument is a significant challenge that separates this advanced characterization technique from commonly performed diffraction experiments. In theory, total scattering experiments attempt to generate an exact total scattering pattern, also known as a structure function, that accurately

represents a sample, shown in equation 4. Where I(Q) is the normalized, background subtracted, sample signal and < b > is the average neutron scattering length of the sample.

$$S(Q) = \frac{I(Q) + < b >^2 - < b^2 >}{< b >^2} \quad \text{[Eq 4]}$$

The structure function only arises after careful background subtraction and normalization, which is dependent on the sample chemistry, sample mass, sample geometry, and the incoming neutron energy spectra. In practice, collected total scattering patterns are often only background subtracted and normalized using an uncorrected vanadium measurement to approximate the neutron energy spectra. This rough pattern has no sample mass and chemistry considerations or corrections for neutron absorption and double scattering and must be scaled and corrected to form an approximate S(Q) using a program like StoG provided by RMCProfile[80, 81].

The local atomic arrangements can be determined through analysis of the pair distribution function (PDF) generated for the sample[82]. A PDF is a histographic representation of the atom pair distances in a sample in real space. The collected approximate neutron structure functions are converted into arbitrary scaled pair distribution functions, by Fourier transform as shown in equation 5.

$$G(r) = \frac{2}{\pi} \int_{Q_{min}}^{Q_{max}} Q[S(Q) - 1]\sin(Qr)dQ \quad \text{[Eq 5]}$$

where Q represents the scattering vector, $4\pi \sin(\theta)/\lambda$, for a neutron of wavelength λ, scattered at an angle θ, and r represents the pair distance in real space.

The quality of the transformed PDF is highly dependent on instrument and sample loading. This is especially challenging for neutron total scattering experiments on samples

disordered *via* extreme conditions as generally little sample mass is produced. The small sample mass results in a lower number of scattering events, which significantly increases the intensity of noise. This effect is most significant in the high Q range of the collected structure function where the neutron flux is lower. This high Q noise is not a factor in determining the average structure as generally no Bragg peaks are present in this region. The noise, however, can cause significant challenges for PDF analysis of the local atomic arrangements.

Several techniques are employed to diminish the effect on the transformed PDF. During scaling in StoG, additional Fourier filters and cut offs are applied. The filter cutoff denotes a point in real space, below which, peaks in the PDF cannot be related to the structure of the sample and must be the result of noise, artifacts from the experimental procedure, and truncation ripples. The applied Fourier filter than attempts to remove these peaks and ripples. The most straightforward method to prevent noise from effecting the transformed PDF is to not transform it. By setting the Q_{max} of Eq 5 to below the point where the structure function is mostly noise, a clearer PDF is generated. This technique was employed in section 2.6 to find the ideal integration range for data collected on SNAP. For the data presented in this dissertation the integration was performed over a Q range of 0.2 to 31.4 Å^{-1} for the data collected at NOMAD. PDFs generated at SNAP were integrated over a Q range of 0.98 to 18 Å^{-1}. Additionally, the truncation ripples in the PDF can be reduced by applying a Lorch function to the collected S(Q)[83]. The Lorch function gradually aligns the collected data to the self-scattering level of the sample, greatly reducing

truncation ripples form the Fourier transform. This process, however, significantly reduces the resolution of the transformed PDF.

Disordering via Temperature

Neutron total scattering data was collected using the Nanoscale-Ordered Materials Diffractometer (NOMAD) at the Spallation Neutron Source (SNS) located at Oak Ridge National Laboratory. The data was obtained *in situ* at high temperature using an Institut Laue-Langevin (ILL) – type vacuum furnace.[84] Both samples were measured for 48 minutes at each temperature step, with $MgAl_2O_4$ measured at 200, 300, 425, 500, 600, 650, 700, 750, 800, 875, 950, and 1000°C, and $NiAl_2O_4$ measured at 100, 200, 300, 425, 500, 600, 650, 700, 750, 850, 950, and 1000°C. An empty vanadium can was also measured to account for background signal. The total scattering structure function, S(Q), was generated by merging the diffraction data from the six detector banks of NOMAD. Before combining, the data from each bank will have its background removed experimentally using the empty vanadium can measurement and the scattering intensity will be normalized by the scattering intensity of a vanadium rod.

Disordering via Irradiation

Ion irradiation was performed with 2.2 GeV Au ions under vacuum and at room temperature using the X0 beamline of the Universal Linear Accelerator (UNILAC) at the GSI Helmholtz Center for Heavy Ion Research in Darmstadt Germany. The microcrystalline powder samples were uniaxially pressed with a hydraulic press (pressure of 25MPa) into a 1 cm diameter, 75-micron machined impression in 9 aluminum holders.

Each holder was wrapped with an aluminum foil of 10 μm thickness, which reduced the ion energy at the sample surface down to 2.0 GeV. Multiple holders were used to maximize sample volume for neutron total scattering experiments. The amount of material that was pressed in each holder was determined using the SRIM 2008 code[85] and limited such that the ions fully penetrated all samples given their range of 110 μm and 96 μm, for $MgAl_2O_4$ and $NiAl_2O_4$, respectively. The energy loss was approximately constant across the sample pellets with average values of 34.2 keV/nm and 38.6 keV/nm for both endmembers. The nine holders were mounted on a 5 cm × 5 cm aluminum plate and together exposed to a fluence of 6×10^{12} ions/cm^2, which is sufficiently high to cover the entire sample area with ion tracks, based on previous work.

The irradiated powder samples, along with their unirradiated reference counterparts, were loaded into quartz capillaries (2 mm outer diameter, 0.01 mm wall thickness), using all 9 aluminum holders for the irradiated samples and an equivalent amount of pristine material per capillary. Neutron total scattering analysis was performed at room temperature, using the Nanoscale-Order Materials Diffractometer (NOMAD) instrument[84] of the Spallation Neutron Source at Oak Ridge National Laboratory. Samples were measured for 2 hours, which resulted in 6 Coulombs of measured proton charge on the spallation target. The measured proton charge is directly proportional to neutron fluence the sample receives. Scattering from an empty quartz capillary was subtracted from the scattering collected from the sample within a capillary and the resulting data were normalized to the scattering from a vanadium rod yielding the neutron total scattering structure function, S(Q).

Spinel Structure Refinement

Rietveld refinement[86] of the neutron diffraction patterns was performed using the software package GSAS II.[87] The average, long-range structure was modeled as a $Fd\bar{3}m$ unit cell. The unit-cell parameter, anion parameter, 6 component background, scale factor, and inversion parameter, defined as the fraction of tetrahedral sites occupied by Al^{3+} ions, were refined. The cation sites were confined to be fully dense, and the associated thermal parameters were related to the crystallographic site rather than the atomic occupant. The microstrain present in the sample was also refined.

The short-range structure of the samples was extracted by small box refinement of pair distribution functions using PDFgui.[88] The local structure was modeled with a two-phase approach for both samples using "normal" cubic ($Fd\bar{3}m$) and "inverse" tetragonal ($P4_122$) atomic arrangements. In the model, the "normal" phase was restricted to only have Mg/Ni on the *8a* site and Al on the *16d* site, whereas the "inverse" phase restricted Mg/Ni to the octahedral site *4a* site with Al occupying the *4b* and *4c* sites. Twenty-two parameters were used in the refinement. In the "normal" phase, the unit-cell parameter (a=b=c), global scale factor, correlated motion parameter, anion parameter, and 1 atomic displacement parameter for each Wykoff site (U_{11}=U_{22}=U_{33}) were refined. In the "inverse" phase, the unit-cell parameter was fixed by the "normal" phase, and the square base was constrained to $\sqrt{2}a_c = \sqrt{2}b_c = c_c$. The global scale factor and the correlated motion parameter were also fixed by the "normal" phase. The atomic positions were refined with 9 parameters, *4c* (x=y), *4a* (y), *4b* (y), and *8d* ($x \neq y \neq z$). Five atomic displacement parameters were used

with a cubic approximation, leaving one parameter for each Wyckoff site ($U_{11}=U_{22}=U_{33}$). The fractions of the “inverse” and “normal” phases were also refined.

Chapter 3

A Note on the Structure of Spinel

Abstract

The space group of the spinel structure was at one point actively debated in literature. The catalyst for which were the results of physical property measurements that could only be explained through atomic distortions not possible in the $Fd\bar{3}m$ space group. These structural irregularities appeared to be confirmed through electron diffraction measurements where reflections forbidden in the $Fd\bar{3}m$ space group were observed. These inconsistencies with the space group of the spinel structure were resolved by a proposed $F4\bar{3}m$ structure. These forbidden reflections, however, were not reproducible when neutron scattering was employed. This inconsistency was attributed to neutron sources of the 1970s not being intense enough to measure these reflections in $MgAl_2O_4$. We have used the CORELLI instrument at the Spallation Neutron Source at Oak Ridge National Laboratory to measure single crystals of $MgAl_2O_4$. The reconstruction of the diffraction pattern includes the previously reported forbidden reflections. Additional analysis shows that these reflections are the result of double diffraction processes, and the space group of Spinel is $Fd\bar{3}m$.

Introduction

Although initially describe in 1915, the space group and structure of $MgAl_2O_4$ was significantly debated in literature 60 years after the initial diffraction experiments by Bragg and Nishikawa [89, 90]. The initial motivation to reevaluate the structure were discrepancies in the physical property measurements of the dielectric constant[91], magnetism[92], and heat capacity[93] of some spinel compositions. Discrepancies in the structure were also observed in several spectroscopy techniques including infrared absorption[94] and electron spin

resonance[95]. These inconsistencies were proposed to originate from a distortion of the spinel structure that was not captured by the $Fd\bar{3}m$ space group[91].

The spinel structure (AB_2X_4) as described in 1915 is a cubic unit cell with eight formula units per cell. The most concise description of the arrangement is two interpenetrating tetrahedra. The first tetrahedra has A at the center and X anions on the corners. One of the X anions is the center of the other tetrahedra with A/B cations on the corners. Four of these motifs can be used to form an entire spinel unit cell. The resulting crystal structure can be described by the $Fd\bar{3}m$ space group with the anions in the 32*e* Wyckoff site, A on the 8*a* tetrahedral site, and B on the 16*d* octahedral site. Deviations from this structure can result from cation anti-site defects, where the A site cation occupies the 16*d* site and vice versa. This defect, referred to as inversion, also causes additional anion disorder with the anion position dilating in the <1 1 1> direction to account for different cation sizes[20].

These disordering mechanisms, however, are not able to account for the measured dielectric properties. Peters and Stanley (1958) noted in their low frequency measurements of magnesium manganese ferrite that its magnetic properties are mostly likely explained by a permanent dipole moment[91]. Forming this dipole moment would require distorting the corner atoms of one of the interpenetrating spinel tetrahedra. A spinel structure defined using the $F4\bar{3}m$ space group, which allowed for this distortion and reconciled previous discrepancies was proposed in 1971 by Grimes[94]. The lower symmetry $F4\bar{3}m$ structure has two unique oxygen positions and displacement parameters, which form an additional large tetrahedral site and small octahedral site.

The $F4\bar{3}m$ space group should be easily distinguishable from $Fd\bar{3}m$ in diffraction experiment as they have different selection rules. Using electron diffraction, Hwang *et. al* (1973) reported a (0, 2, 0) reflection in $MgAl_2O_4$, which is forbidden in the $Fd\bar{3}m$ space group[96]. These reflections were also found in electron diffraction patterns collected by Heuer and Mitchell[97] (1975) and Mishra and Thomas[98] (1977). Whether these measured forbidden reflections were real was questioned by Smith (1978), who proposed they were the result of double diffraction, which was measured using electron diffraction by Tokonami and Horiuchi (1980) [99, 100]. Simultaneous to many of these electron diffraction experiments were attempts to measure the forbidden peak with neutron diffraction[101].

Neutron diffraction provides many advantages over electron and x-ray diffraction. Neutrons interact with the nuclear structure of an atom and, therefore, easily distinguish between atoms with low atomic numbers. Importantly, neutron diffraction beamlines commonly use of a time of flight spectrometers, which can separate out harmonic contributions that may cause unusual reflections. This technique was initially applied on magnetite spinel, Fe_3O_4, by Samuelson[102] (1974) where no forbidden (2 0 0) reflection was measured. Samuelson and Steinvoll[103] (1975) repeated this technique on spinel, $MgAl_2O_4$, and were also unable to reproduce the forbidden peaks measured through electron diffraction. The inability to reproduce electron diffraction results using neutron diffraction was address by Heuer and Mitchell[97] (1975) as the result of the weak flux of neutron sources. They argued that the weak, measured intensity of the (2 0 0) peak in electron diffraction would be impossible to distinguish from the background in neutron diffraction

experiments. These discrepancies were never resolved and recent publications still consider the potential for spinel to be better described by the $F4\bar{3}m$ space group[104].

Modern spallation neutron sources, however, have significantly higher neutron fluxes than historic reactor sources. Using the Corelli instrument at the Spallation Neutron Source at Oak Ridge National Laboratory, we have measured multiple Spinel, $MgAl_2O_4$, samples. In these samples, the h + k = 4n + 2 forbidden reflections are present. These peaks are not dependent on the intrinsic amount of disorder in the spinel crystal, are the result of double diffraction, and are not evident of the $F4\bar{3}m$ space group.

Methods

Sample Procurement and Preparation

$MgAl_2O_4$ single crystals were purchased from MSE Supplies, batch number 31221B6. The crystals were 10mmx10mmx0.5mm in size, double sided polished, and cut in the [1 0 0] direction. Samples were then scored and split into two 10mm x ~5mm x 0.5mm sections to create two approximately 100 mg pieces.

Neutron Single Crystal Diffraction and Data Analysis

$MgAl_2O_4$ single crystals were measured using the CORELLI instrument at the Spallation Neutron Source at Oak Ridge National Laboratory[105]. The single crystals were mounted on Aluminum “spoons” using epoxy and an Aluminum band to ensure the attachment. The “spoons” are created at the SNAP beamline by pressing the end of an 35mmx1.5mm aluminum rod in a hydraulic press to form a flat surface for the crystals to be mounted to. The spoon was then affixed to a measured coolant stick and the position of

the inserted spoon was adjusted to center the crystal in the neutron beam. The end of the stick was wrapped in Cadmium to prevent any signal from the holder. The entire assembly was then lowered into the CCR (closed cycle refrigerator) for data collection.

Neutron scattering data was collected at 300K, with the correlation chopper active. The angle of the sample was changed in 1.5° increments and at each step the sample was exposed to neutrons for 50 seconds. This process was repeated for 3 hours and 20 minutes to capture 360 degrees of scattering. A fine mesh scan was also performed at 300K around the 0 -2 0 forbidden reflection, using 0.195° steps with 180 minute exposures. The collected data was transformed with a calculated UB matrix into a 3D reconstruction of the diffraction pattern, which was integrated with no symmetry constraints and refined using the GSASII software package[106].

Results and Discussion

An *hk0* slice of the reconstructed single crystal neutron diffraction pattern of $MgAl_2O_4$ with and without the correlation chopper is shown in Figure 3.1. The diffraction rings present are from the aluminum holder the crystal is affixed to and is unique to each measurement. The “tails” on the diffraction spots are characteristic of CORELLI and are removed by the correlation chopper as shown in the bottom pattern. The correlation chopper also removed the diffuse scattering clouds present around the strong reflections. The h + k = 4n + 2 reflections are present both with and without the correlation chopper. A *h00* line cut of the slice shown in Figure 3.1 without the correlation chopper is shown in Figure 3.2.

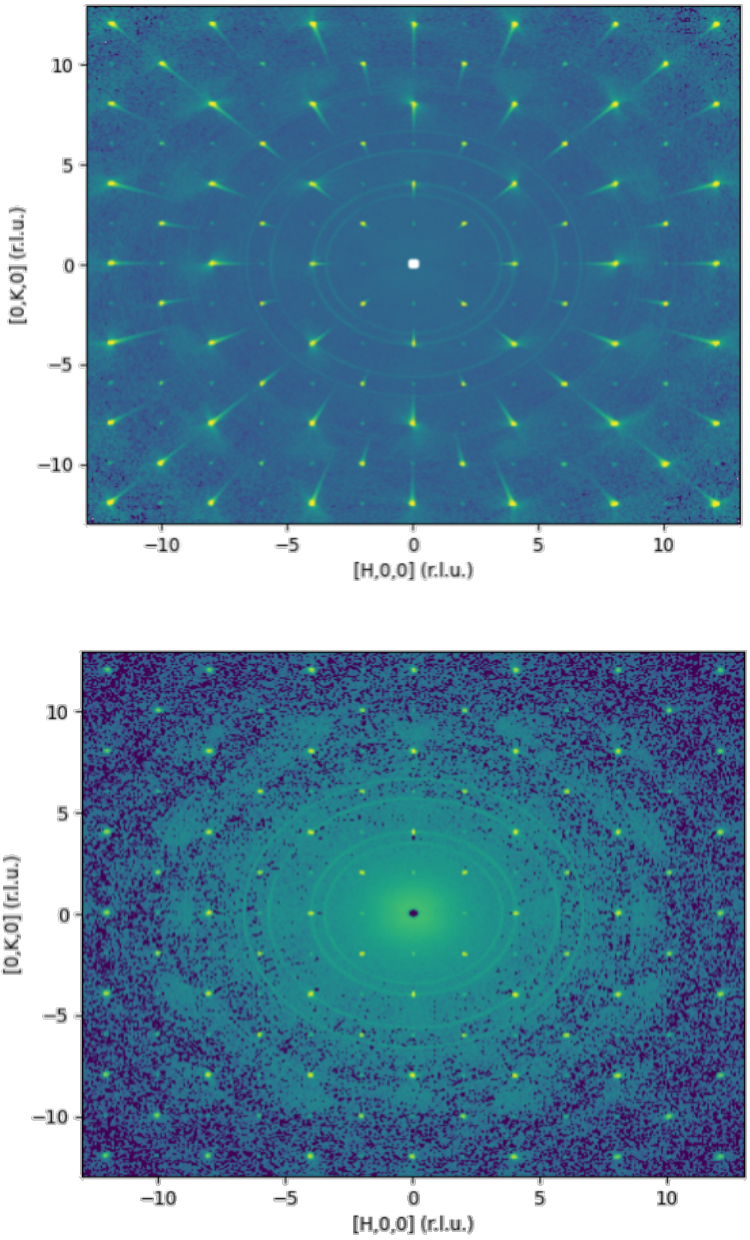

Figure 3.1: Reconstructions of the diffraction pattern of $MgAl_2O_4$ without (top) and with (bottom) the correlation chopper active. Sample was measured at 300K.

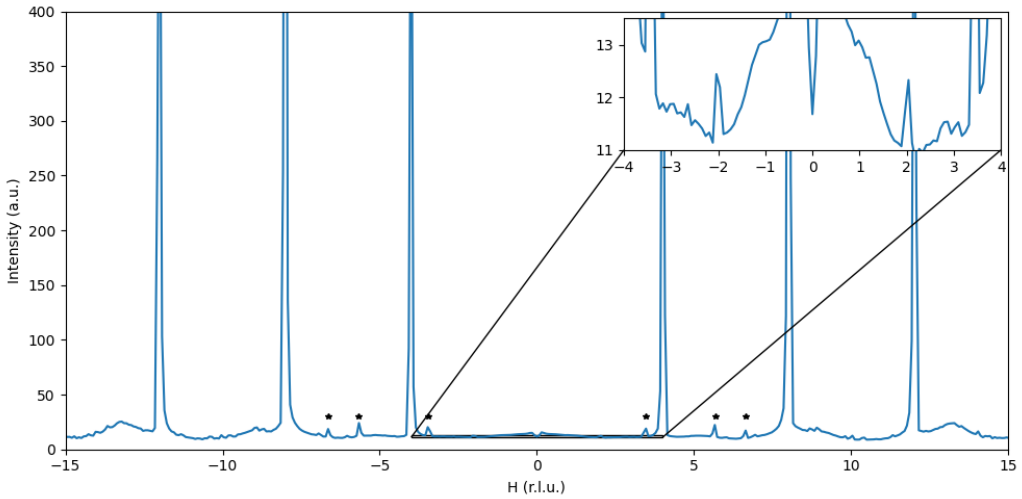

Figure 3.2: An h00 line cut of the slice shown in Figure 3.1. The inset highlights to 200 and -200 peaks. The black stars denote peaks from the aluminum holder.

The strong reflections are associated with the spinel phase described by the $Fd\bar{3}m$ space group |(4 0 0)|, |(8 0 0)|, |(12 0 0)|. Along with these peaks are very weak reflections at |(2 0 0)|, |(6 0 0)|, |(10 0 0)| with the |(2 0 0)| peaks highlighted by the inset.

A fine mesh scan in theta was performed around the (0 -2 0) reflection to determine how the peak intensity varied with neutron wavelength. The small changes in angle select different neutron wavelengths from the white beam which can interact with the (0 -2 0) plane. If the reflection is real, small changes to the wavelength should not affect the peak intensity significantly; however, if the peak is a result of double diffraction, small changes to the wavelength will affect the double diffraction process significantly. The results of the fine mesh scan are shown in Figure 3.3. The intensity of the (0 -2 0) peak is highly dependent on incident neutron wavelength with an oscillatory behavior. It is, therefore, highly likely that this reflection is the result of double diffraction and not a new reflection in $MgAl_2O_4$.

The results of neutron diffraction on a single crystal show that the space group of the spinel is $Fd\bar{3}m$. The measured diffraction peaks, however, only reflected the average structure of spinel. Recent work has shown that inverted spinels display structural heterogeneity where the long range average structure is different from the distinct local atomic arrangements[75, 107]. The local structure of spinel is a tetragonal structure described by the $P4_122$ space group and the averaging of these local domains forms the long range $Fd\bar{3}m$ structure. The phase fraction of the local structure is directly tied to the amount of inversion, cation anti-site defects, in the spinel crystal[77].

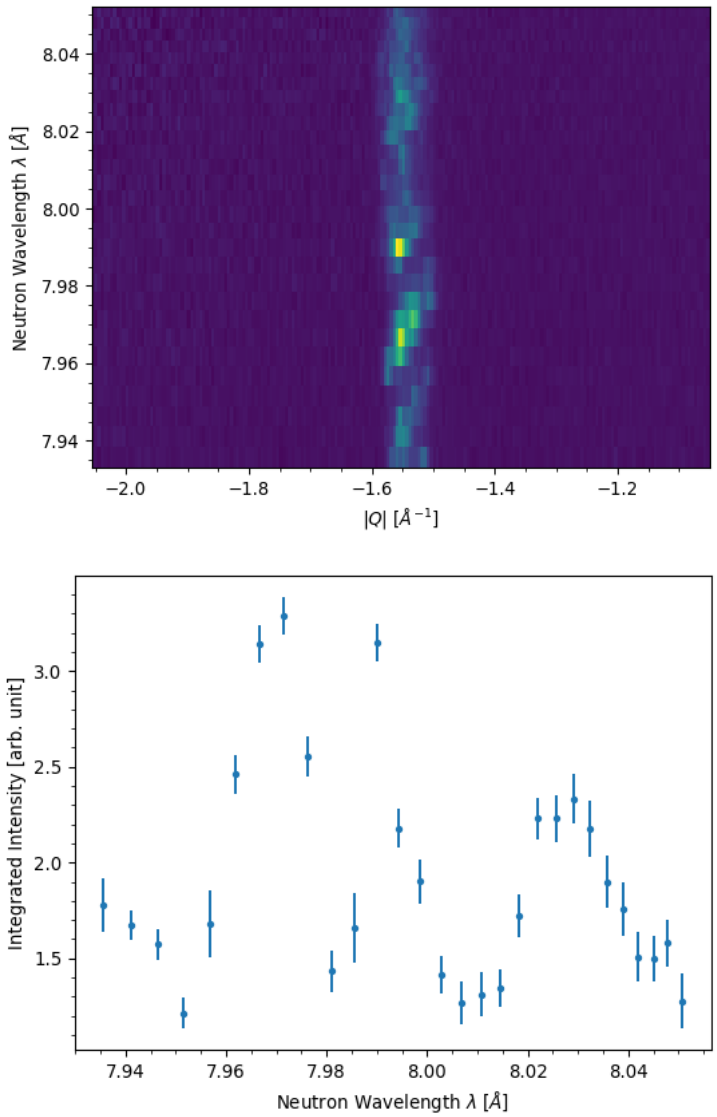

Figure 3.3: Variation in the intensity of the 0 -2 0 reflection when scattering neutrons of different wavelengths.

For the single crystal measured, the level of inversion was determined to be $i = 0.113 \pm 0.021$ from Rietveld refinement. This amount of inversion is common for synthetically synthesized $MgAl_2O_4$ samples.

Whether the amount of inversion in a measured spinel could potential effect the presence and intensity of the forbidden reflections was previously proposed in literature; however, few studies discuss the amount of inversion as it is difficult to determine from electron diffraction experiments alone[108]. The forbidden reflections being dependent on inversion could explain the conflicting results of electron diffraction between compositions and even in identical compositions if they were synthesized differently. This explanation of previous results is likely not correct as we have shown that we can measure the forbidden reflections in $MgAl_2O_4$ with neutron diffraction and shown that they are most likely the result of double diffraction. The variations in results are likely from subtle changes in the experimental setup between authors and samples. As shown in figure 3, double diffraction events are highly depended on the exact experimental conditions and small deviations can drastically change the measured peak intensity.

Although likely not the source of the forbidden reflections, the effect of inversion on distortions in spinel may be useful in understanding physical property measurements that cannot be explained using the $Fd\bar{3}m$ structure. If these properties are affected by the amount of inversion it suggests they are related to the $P4_122$ local structure which is formed as a consequence of the formation of the cation anti-site defect. It is prudent, therefore, to readdress many of these previous property measurements that are dependent on local cation arrangements using the current $P4_122$ local structure.

Conclusions

Spinel single crystals of $MgAl_2O_4$ were measured using neutron diffraction at the CORELLI beamline at the Spallation Neutron Source at Oak Ridge National Laboratory. The normalized reconstruction of the diffraction pattern showed reflections forbidden in the $Fd\bar{3}m$ space group. A fine mesh scan around one of these reflections revealed that the intensity is highly dependent on the neutron wavelength suggesting they are the result of double diffraction processes. The previously measured physical properties, which require atomic distortions not possible in the $Fd\bar{3}m$ space group should be reassess using the new proposed local tetragonal $P4_122$ phase, which has been consistently measured in Spinels with some amount of inversion.

Chapter 4

Short Range Ordering of $MgAl_2O_4$ and $NiAl_2O_4$ at High Temperature

This chapter is reproduced in part with permission from Hirtz, J: O'Quinn, E.C.; Gussev, I.; Neuefeind, J.; Lang, M. "Cation Short-Range Ordering of $MgAl_2O_4$ and $NiAl_2O_4$ Spinel Oxides at High Temperatures via In Situ Neutron Total Scattering." Inorganic Chemistry **61**(42): 16822-16830.[77] Copyright 2022 American Chemical Society.

This chapter has been revised from its published form to present important information to the reader when it is pertinent and to prevent information overlap with other chapters. The extended introduction into the spinel structure and review of the previous high temperature studies has been moved to the introduction and the information on the methodology is presented in the experimental methods section. Presented in this chapter are the abstract, experimental results, discussion, and conclusions. For this published work, J.H, I.G, E.C.O and M.L. conceived the experiment. E.C.O, J.N, and M.L. performed the neutron scattering experiment, J.H analyzed the data, E.C.O., J.H, I.G, and M.L interpreted the data, and J.H wrote the manuscript with input from all authors.

Abstract

Complex oxides that adopt the isometric spinel structure (AB_2O_4) are important for numerous technological applications and are relevant for certain geological processes, which involve exposure to extreme environments such as high pressures and temperatures. Recent studies have shown that the changes to the spinel structure caused by these environments are complex and depend on the material length scale under consideration. In this study we have expanded this approach to the behavior of spinels under high temperature. *In situ* neutron total scattering experiments, coupled with pair distribution

function analysis, performed on two spinel compositions with various levels of pre-existing disorder ($MgAl_2O_4$ and $NiAl_2O_4$) revealed that both compositions trend to a state of maximum disorder where the A and B cations are randomly distributed amongst the two available sites. Temperature-induced cation inversion, conventionally understood as exchange of cations on the A and B sites, is locally expressed as an atomic rearrangement to a tetragonal symmetry, a correlation that is retained up to the maximum temperature studied (1000 °C). A complex thermal expansion behavior is revealed wherein the oxide materials expand heterogeneously at the level of coordination polyhedral with an apparent dependence on bond strength.

Experiment Results

The neutron diffraction patterns of $MgAl_2O_4$ and $NiAl_2O_4$ at 200°C and 1000°C are shown in Figure 4.1*a* and 4.1*b*. With increasing temperature, a change in the diffraction pattern is observed with the diffraction maxima broadening and shifting toward higher *d*-spacing in both samples, which can be attributed to increased thermal vibrations and thermal expansion, respectively. No additional peaks are apparent in the pattern at 1000°C, and no peaks diminish as compared to the data measured at 200°C. Rietveld refinement was performed on the long-range diffraction data measured at all temperatures using the conventional spinel structural model defined in Table 4.1, which yielded the unit-cell parameter, inversion parameter, and anion parameter (Table 4.2).

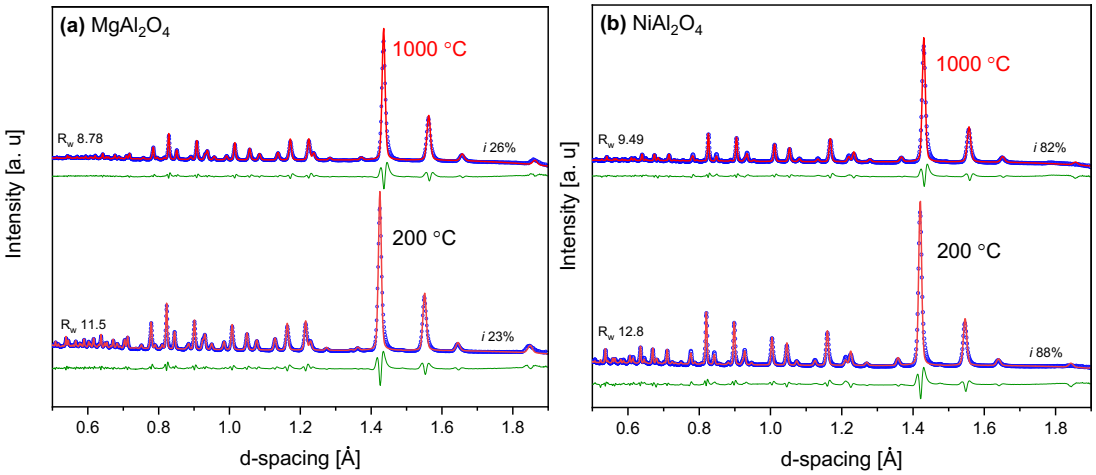

Figure 4.1: Stacked neutron diffraction patterns for (*a*) $MgAl_2O_4$ and (b) $NiAl_2O_4$ spinel at 200°C and 1000°C collected from Bank 5 of the NOMAD detector array. The blue circles represent collected data and the red line depicts the simulated diffraction pattern using the conventional spinel structural model (Table 4.2.1). The green curve represents the difference between observed and calculated diffraction patterns, quantified by the goodness-of-fit-parameter R_w. The parameter *i* denotes the inversion in the spinel compound.

Table 4.1: Cubic $Fd\bar{3}m$ and tetragonal $P4_122$ structural models used for Rietveld (long range) and small-box (short range) refinements of $MgAl_2O_4$ and $NiAl_2O_4$ spinels. Coordination numbers (CN) of different Wyckoff sites are given in parentheses. Bold positional coordinates are free parameters that were fit during refinement.

Wyckoff Equipoints (CN)	Occupant	x	y	Z
	Cubic			
8*a* (4)	Mg / Ni	0.125	0.125	0.125
16*d* (6)	Al	0.5	0.5	0.5
32*e*	O	***0.25***	***0.25***	***0.25***
	Tetragonal			
4*a* (6)	Mg / Ni	0	***0.25***	0
4*b* (4)	Al	0.5	***0.25***	0
4*c* (6)	Al	***0.25***	***0.25***	0.375
8*d*	O	***0.75***	***0***	***0.5***
8*d*	O	***0.25***	***0.5***	***0.5***

Table 4.2: Results of Rietveld refinement of neutron diffraction data for $MgAl_2O_4$ and $NiAl_2O_4$ spinels measured at a range of temperatures up to 1000°C. Shown are unit-cell parameter a_0, inversion parameter i, and anion parameter u; R_w values represent the goodness-of-fit between experimental data and utilized cubic $Fd\bar{3}m$ spinel structural model.

$MgAl_2O_4$	a_0	i	u	R_w	$NiAl_2O_4$	a_0	I	u	R_w
200 °C	8.07360(6)	0.23(3)	0.26162(8)	11.555	**100 °C**	8.04025(6)	0.88(1)	0.2553(1)	12.860
300 °C	8.08051(6)	0.22(4)	0.26161(8)	11.267	**200 °C**	8.04611(6)	0.87(1)	0.2553(1)	12.431
425 °C	8.08955(6)	0.21(4)	0.26159(9)	10.739	**300 °C**	8.05262(6)	0.87(1)	0.2552(1)	12.040
500 °C	8.09506(6)	0.20(4)	0.26160(9)	10.461	**425 °C**	8.06068(6)	0.87(1)	0.2551(1)	11.509
600 °C	8.10286(6)	0.18(4)	0.26166(9)	10.066	**500 °C**	8.06527(6)	0.87(1)	0.2551(1)	11.139
650 °C	8.10653(6)	0.20(4)	0.26149(9)	9.871	**600 °C**	8.07209(6)	0.87(1)	0.2550(1)	10.901
700 °C	8.11018(6)	0.21(4)	0.2613(1)	9.706	**650 °C**	8.07538(6)	0.87(1)	0.2550(2)	10.727
750 °C	8.11395(6)	0.22(5)	0.2612(1)	9.544	**700 °C**	8.07896(6)	0.87(1)	0.2550(2)	10.632
800 °C	8.11773(6)	0.23(5)	0.2610(1)	9.362	**750 °C**	8.08273(6)	0.86(1)	0.2550(2)	10.508
875 °C	8.12357(6)	0.24(5)	0.2609(1)	9.151	**850 °C**	8.09091(7)	0.86(1)	0.2551(2)	10.005
950 °C	8.12957(67)	0.25(56)	0.2607(11)	8.936	**950 °C**	8.09990(7)	0.83(2)	0.2552(22)	9.770
1000 °C	8.13373(67)	0.26(57)	0.2606(12)	8.783	**1000 °C**	8.10478(7)	0.82(21)	0.2552(22)	9.495

As shown for the representative data measured at 200°C and 1000°C (Figure 2.1), this structural model describes the diffraction data well for both compositions at all temperatures.

The structural refinements reveal that the unit-cell parameters of both samples increase with temperature in agreement with the effect of thermal expansion. The change in inversion parameter and anion parameter as a function of temperature is shown in Figure 4.2. The $MgAl_2O_4$ spinel initially has low inversion (i ~ 0.23), which generally remains constant with increasing temperature up to 600°C, where the inversion begins to increase linearly (i ~ 0.26 at 1000°C). The initial level of inversion in $MgAl_2O_4$ is slightly higher than expected for an ordered spinel sample, which may be ascribed to slight non-stoichiometry in the starting material.[30] However, the temperature-dependent behavior of the inversion parameter with a plateau at lower temperatures and a linear increase above 600°C agrees well with previous experiments for $MgAl_2O_4$.[30] The inversion parameter of $NiAl_2O_4$ is significantly higher (i ~ 0.88) than that of $MgAl_2O_4$, indicative of a more "inverse" cation arrangement, and remains relatively constant during the heating process up to 800°C, above which i slightly decreases. The anion parameter, u, highly sensitive to the cation partitioning among the two available sites, is directly correlated with the inversion parameter, i, and exhibits a similar behavior with increasing temperature for both compounds. The anion parameter, u, of $MgAl_2O_4$ remains constant during heating up to 600°C, above which it notably decreases; this decrease is indicative of the anion sublattice trending towards an ideal cubic close-packed arrangement (u = 0.25). In contrast, the anion parameter of $NiAl_2O_4$ is initially much lower and remains generally

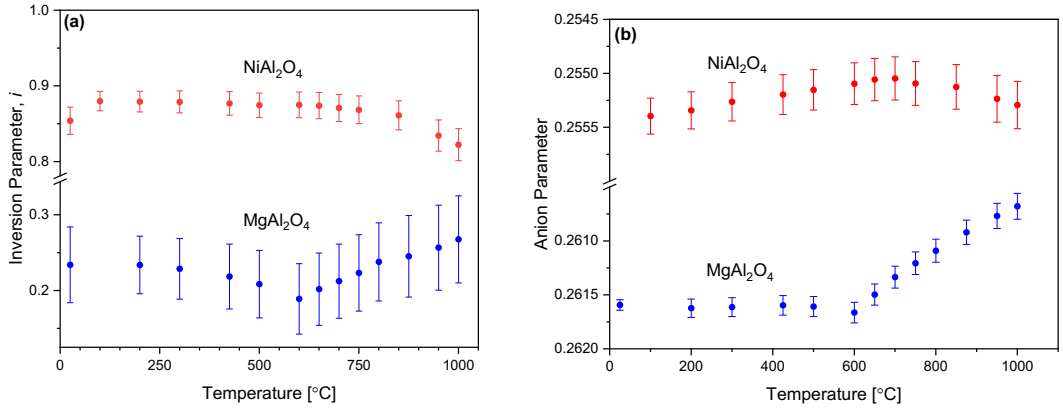

Figure 4.2: (*a*) Inversion parameter and (*b*) anion parameter of $MgAl_2O_4$ (bottom, blue spheres) and $NiAl_2O_4$ (top, red spheres) spinels obtained by Rietveld refinement of neutron diffraction data as a function of temperature. The error bars represent uncertainty of the refinement process and were directly taken from the GSAS II software. Ordinate in (b) is inverted and truncated for clarity and better comparison with (a).

constant until heating above ~800°C, after which it increases. The behavior of all three structural parameters (*a, u,* and *i*) with increasing heating agrees well with previously reported results on thermal- induced disordering in spinel, including critical temperatures of approximately 600°C and 800°C for $MgAl_2O_4$ and $NiAl_2O_4$, respectively.[30, 32]

Employing the structural relations from Sickafus *et al*.,[20] the average volumes of the *8a* and *16d* polyhedra were calculated using the unit-cell and anion parameters. During heating, the polyhedra initially increase in volume, caused by the expanding unit-cell parameter, $u$until the critical temperature is reached and the initial inversion begins to change. At temperatures beyond this point, the change in polyhedral volume is dominated by the anion parameter. This effect is most striking in $MgAl_2O_4$, where the *8a* tetrahedra no longer expand with increasing temperature as the smaller Al cation moves into the *8a* sites.

Further structural insight into local atomic changes during heating was obtained from neutron pair distribution function (PDF) analysis (Figure 4.3). The PDFs of the two compositions are very similar but show some differences in peak width and intensity ratios, which is related to some degree of structural disorder. With respect to the PDF of the samples collected at 200°C, the peaks in the PDF of the samples collected at 1000°C are dampened and broadened.

Small-box refinement was used to analyze all PDFs to determine temperature-induced changes of interatomic distances and local coordination environments in both samples. For this purpose, a two-phase model was utilized consisting of the "normal" cubic ($Fd\bar{3}m$) and an "inverse" tetragonal ($P4_122$) atomic arrangement (Table 4.2) as

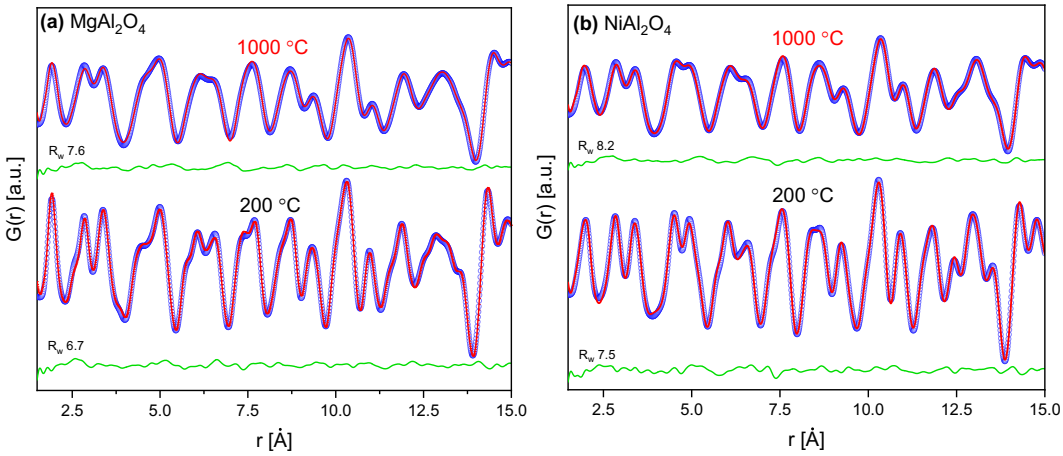

Figure 4.3: Stacked neutron pair distribution functions (PDFs) for (a) $MgAl_2O_4$ and (b) $NiAl_2O_4$ spinels at 200°C and 1000°C. The blue circles represent collected data and the red lines depict the simulated distribution functions using a mixed-phase spinel structural model consisting of cubic $Fd\bar{3}m$ and tetragonal $P4_122$ (Table 4.2). The green curve represents the difference between observed and calculated PDFs., quantified by the goodness-of-fit-parameter R_w.

suggested by a previous study that investigated chemical-induced disordering in these same spinel compounds.[71] The phase fraction and polyhedral volumes were deduced for both compositions at each temperature, and the results are summarized in Table 4.3. As shown in (Figure 4.4), the fraction of the tetragonal (*P4₁22*) phase increased for $MgAl_2O_4$ with temperature at the expense of the cubic phase, while the behavior is opposite for $NiAl_2O_4$.

Discussion of Results

Neutron total scattering was used in this study to characterize the underlying atomic-scale structural changes induced by cation inversion from exposure to high temperature. High sensitivity to the oxygen sublattice and simultaneous access to the short-range and long-range structure permitted comprehensive evaluation of thermally-induced disordering in $MgAl_2O_4$ and $NiAl_2O_4$. The long-range results, assessed by Rietveld refinement of diffraction data over the entire temperature series, agree with previous neutron diffraction studies of both compositions at elevated temperatures.[15, 30] $MgAl_2O_4$ spinel, with an initially low level of inversion, shows increased cation disorder with increasing temperature, structurally changing towards a fully disordered random cation arrangement. $NiAl_2O_4$, with an initially high level of inversion, also further disorders upon heating, with inversion decreasing towards a random distribution of cations across the two available sites. The changes in inversion in both compositions were also reflected in the anion parameter, which is directly related. The diffuse scattering in the neutron structure functions, S(Q), at higher temperature in both samples is indicative of thermally-induced structural changes at the short-range, which are not

Table 4.3: Results of small box refinement from neutron PDFs of $MgAl_2O_4$ and $NiAl_2O_4$ utilizing a mixed-phase spinel structural model consisting of cubic $Fd\bar{3}m$ and tetragonal $P4_122$ (Table 4.1). The phase fraction denotes the relative amount of the tetragonal phase.

$MgAl_2O_4$	**Phase Faction**	**R_w**	**$NiAl_2O_4$**	**Phase Fraction**	**R_w**
200 °C	0.26(4)	0.067	100 °C	0.86(2)	0.075
300 °C	0.26(6)	0.067	200 °C	0.86(2)	0.075
-	-	-	300 °C	0.87(2)	0.074
500 °C	0.26(7)	0.071	425 °C	0.88(2)	0.075
600 °C	0.25(6)	0.069	500 °C	0.88(2)	0.074
650 °C	0.27(6)	0.066	600 °C	0.89(2)	0.75
700 °C	0.28(6)	0.066	650 °C	0.89(2)	0.075
750 °C	0.29(5)	0.070	700 °C	0.89(2)	0.075
800 °C	0.30(6)	0.072	750 °C	0.89(2)	0.075
875 °C	0.32(6)	0.073	850 °C	0.89(3)	0.078
950 °C	0.34(6)	0.075	950 °C	0.88(3)	0.080
1000 °C	0.35(6)	0.076	1000 °C	0.88(3)	0.082

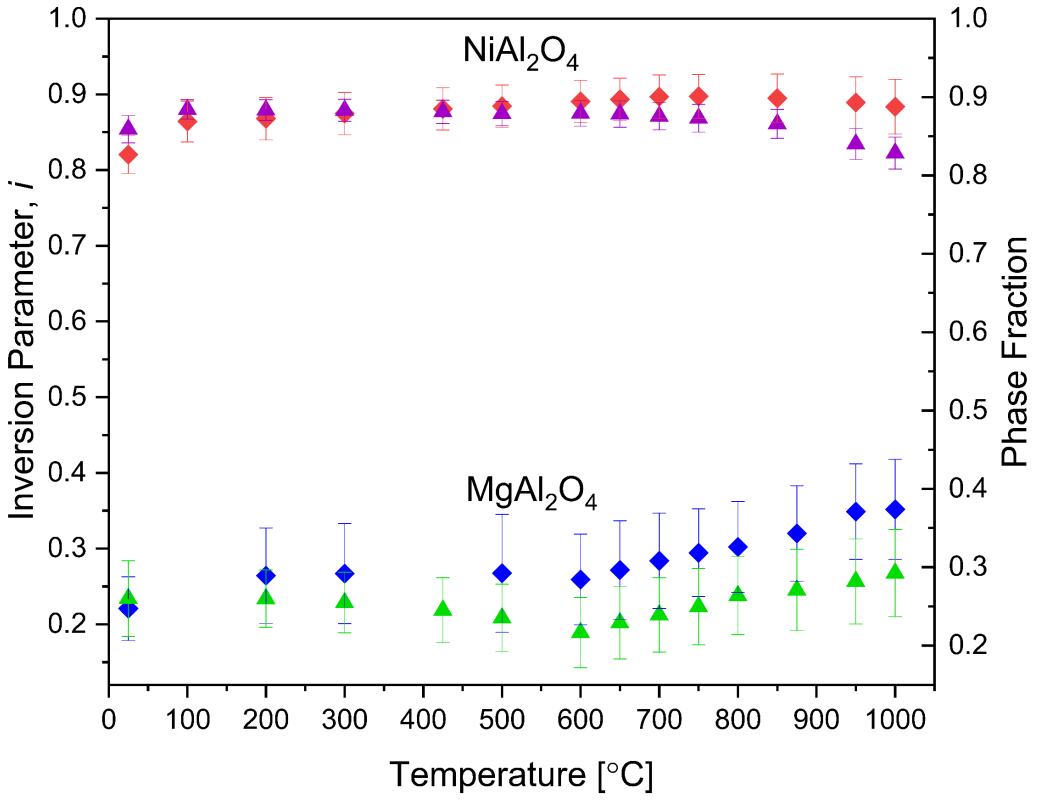

Figure 4.4: Comparison of the local tetragonal phase fraction (blue and red diamonds) from PDF small-box refinement and long-range inversion parameter (green and magenta triangles) from Rietveld refinement of diffraction patterns for $MgAl_2O_4$ and $NiAl_2O_4$ spinels based on neutron total scattering experiments across a range of temperatures. The error bars represent the uncertainty of the refinement process and were taken directly form the GSASII and PDFGUI software packages.

captured by Rietveld refinement of the Bragg peaks alone.[109, 110] A neutron total scattering study recently showed that chemically-induced disorder across the $Mg_{1-x}Ni_xAl_2O_4$ solid-solution series, with Mg being replaced by Ni at room temperature, proceeds at the atomic scale as a phase transition by which the ordered isometric spinel phase is increasingly replaced by a tetragonal phase.[71] The same tetragonal *$P4_122$* structural model[71] was used in the small-box modeling of this study, together with the cubic $Fd\bar{3}m$ phase, to fully capture all changes in the PDFs across different temperatures. This approach significantly improved the fit quality and agreement between experimental data and the structural model, particularly for $NiAl_2O_4$. The fraction of the tetragonal *$P4_122$* phase (Table 4.3) was evaluated together with the inversion parameter (Table 4.2) as a function of increasing temperature to compare thermally induced short- and long-range changes (Figure 4.4). The two parameters exhibit a very similar trend with increasing temperature for both spinel oxides, which agrees very well with the compositional behavior observed in the solid-solution series.[71] This agreement leads to the conclusion that an increase in inversion across the long-range structure, driven by thermal treatment, corresponds to local buildup of a tetragonal phase (and, *vice versa*, less inversion corresponds to decreasing fraction of the tetragonal phase). Thus, inversion and related cation disordering in spinel are described by the same atomic-scale processes, independently of the disordering mechanism (thermally driven as in this study or chemically induced as in[71, 72]).

The use of the *$P4_122$* model for the local atomic arrangement of disorder in spinel can be rationalized by crystal structure theory.[74] Inversion across the long-range is described as cation exchange (*i.e.* for $MgAl_2O_4$, Mg cations move into Al-sites, while Al cations

move into Mg sites). From a local atomic perspective, the size of cations (ionic radius) and available sites must be comparable, and the bonding environment must satisfy local charge balance as outlined by Pauling's first and second rules.[74] The tetragonal phase accounts for these constraints when the structure is disordered across the Mg and Al sites by providing additional cation sites that can accommodate the differently sized cation species, in agreement with Pauling's first rule. The resulting bonding environment of cations and anions cannot exactly satisfy the nominal bond strength sums in the disordered phase (2.0 for fully ordered spinel), but Pauling's second rule is satisfied approximately by a combination of two specific structural motifs.[73] The lower-symmetry tetragonal phase in $MgAl_2O_4$ and $NiAl_2O_4$ is the simplest atomic arrangement with 2 unique oxygen positions with bond strength sums of 1.917 and 2.083, averaging to 2.0.[74] While the driving force of inversion can differ (e.g., intrinsic: changes in chemical composition, or extrinsic: temperature exposure), the final disordered atomic arrangement is described by the same tetragonal structural model, which is a direct consequence of Pauling's rules.

The disordering process and the observed phase changes over the short-range structure can be conventionalized based on transformation of coordination polyhedra. The $P4_122$ space group, used to model the atomic relaxation associated with cation inversion and disorder, exhibits three distinct polyhedra: (*i*) the 4*b* tetrahedra containing a B site cation, (*ii*) the larger 4*a* octahedra containing an A site cation, and (*iii*) the smaller 4*c* octahedra containing a B site cation. A fully ordered, "normal" spinel ($i = 0$), however, only has two distinct polyhedra based on the $Fd\bar{3}m$ space group, the *8a* tetrahedra containing an A site cation and the *16d* octahedra containing a B site cation. There are two octahedra for each

tetrahedron in the cubic phase given by the 1:2 cation stoichiometry, but both octahedra (and the corresponding B site cations) are indistinguishable from each other. The transition from "inverse" $P4_122$ to "normal" $Fd\bar{3}m$ spinel, as observed for $NiAl_2O_4$ with increasing temperature, can be thought of as an exchange of the A site cation in the *4a* octahedra with the B site cation in the *4b* tetrahedra. This exchange creates a new A site cation tetrahedra and two B site cation octahedra that are no longer distinguishable. The new polyhedral configuration is described by the same parameters as a "normal" spinel. The reverse operation, a transition from "normal" to "inverse" spinel as observed for $MgAl_2O_4$ at high temperatures, occurs by a similar exchange process, but it remains unclear which of the two non-distinguishable B site octahedra participate in the exchange with the A site cation.

The average polyhedral volumes, deduced from the long-range structure, have previously been demonstrated to depend only on the unit-cell and anion parameters.[20] Using these relations, it can be seen based on the neutron diffraction data that the structural evolution of coordination polyhedra (Figure 4.5) starts to deviate from a simple, linear thermal-expansion behavior beyond the critical temperature where cation movement further disorders the structure: ~600°C for $MgAl_2O_4$ and ~800°C for $NiAl_2O_4$. In this long-range view, movement of the larger Mg^{2+} cation into the octahedral site (and smaller Al^{3+} cation into the tetrahedral site) causes a contraction in the tetrahedra volume

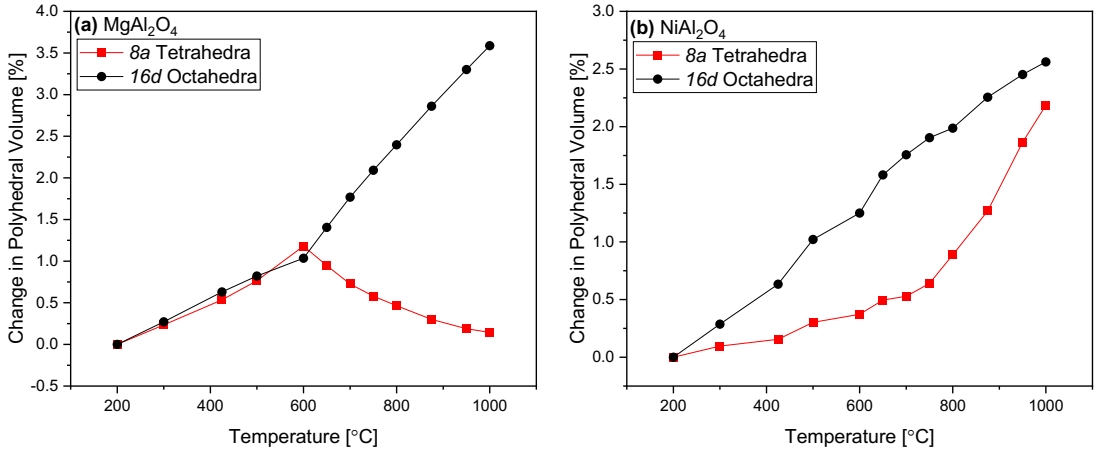

Figure 4.5: Evolution of average volume of coordination polyhedra in (a) $MgAl_2O_4$ and (b) $NiAl_2O_4$ spinel with increasing temperature based on long-range structural data (neutron diffraction). The black circular data points and black line connecting the data points represent the 16d octahedra, and the red squared data points and connecting red line represent the 8a tetrahedra. Occupancy of polyhedra by cations differs in both samples.

and an expansion of the octahedra (Figure 4.5*a*). Disordering for $NiAl_2O_4$ spinel at high temperature results in reduction of inversion, which means for the long-range structure that the smaller Al^{3+} cation moves from its tetragonal site to the octahedral site (Figure 4.5*b*). Beyond the critical temperatures where inversion changes, cation exchange plays a critical role in modifying the size of polyhedra with increasing temperature. In fact, in $MgAl_2O_4$ inversion leads to an increasing contraction of the tetrahedra above ~600°C, while the octahedra volume shows accelerated expansion above that point, which drives the observable net thermal expansion. The effect is opposite for $NiAl_2O_4$, and decreasing inversion above ~800°C leads to reduced expansion of the octahedra and increased expansion of the tetrahedra. The interpretation of the individual polyhedra volumes with respect to inversion in the $Fd\bar{3}m$ long-range structure, however, is indirect as it is based on the diffraction pattern analysis and associated long-range parameters (unit-cell and anion parameters).

Direct evaluation of the volume of all 5 coordination polyhedra existing in the two phases (cubic, $Fd\bar{3}m$ and tetragonal, $P4_122$) in the local structure was assessed in this study by analysis of the the neutron PDF data. Small-box modeling was used to determine the volume of each tetrahedra and octahedra in the mixed normal and inverse spinel configurations. The behavior of the polyhedral volume exhibits a more complex evolution with temperature (Figure 4.6) as compared with the indirect characterization from the long-range structure (Figure 4.5). To better interpret the PDF data, one must consider that changes in the volume of individual polyhedra are caused by two processes: (*1*) thermal expansion (below and above critical temperatures) and (*2*) phase changes

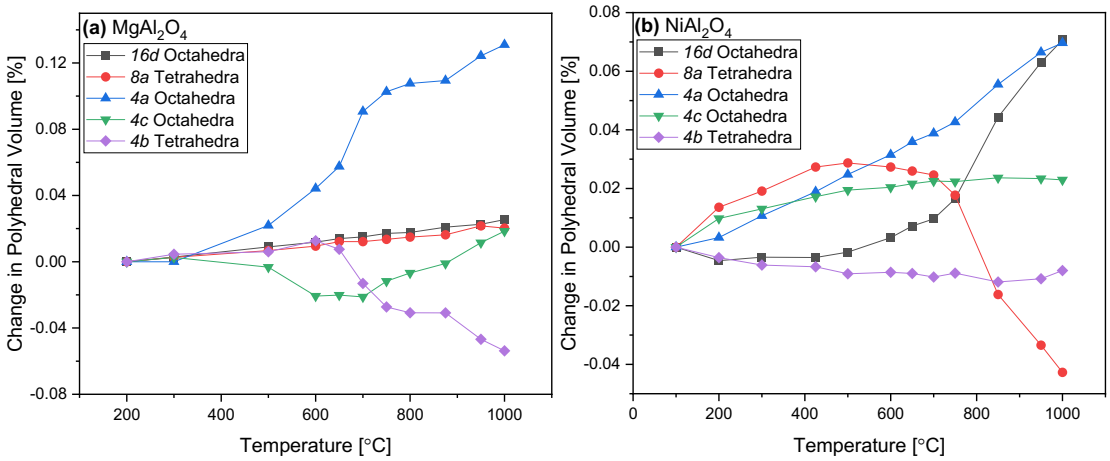

Figure 4.6: Evolution of the volume of local coordination polyhedra with increasing temperature based on small-box modeling of neutron PDF data obtained for (a) $MgAl_2O_4$ and (b) $NiAl_2O_4$ spinel. The black squares represent the 16d octahedra, the red circles represent the 8a tetrahedra, the blue triangles represent the 4a octahedra, the green inverse triangles represent the 4c octahedra, and the purple diamonds represent the 4b tetrahedra. All corresponding colored lines are drawn to guide the eye.

related to inversion (above critical temperatures). The relative abundance of the tetragonal phase (and the associated polyhedra) is increased in $MgAl_2O_4$ and decreased in $NiAl_2O_4$ with increasing temperature. As it was the case for the long-range analysis, the onset of inversion processes and associated cation movement is expressed in each spinel composition by abrupt changes in the polyhedral volume evolution. However, only some coordination polyhedra show this distinct behavior. The polyhedra of the dominant phase in each composition (cubic phase for $MgAl_2O_4$ and tetragonal phase for $NiAl_2O_4$) exhibit a continuous linear change in their volume even beyond the critical temperatures (~600°C for $MgAl_2O_4$ and ~800°C for $NiAl_2O_4$), as shown by the red and black data points in Figure 4.6*a*, as well as the blue, green, and purple data points in Figure 4.6*b*. In contrast, the polyhedra of the minor phase in each composition (tetragonal phase for $MgAl_2O_4$ and cubic phase for $NiAl_2O_4$) change their volumes distinctly above the critical temperatures, as shown by the blue, green, and purple data points in Figure 4.6*a*, as well as the red and black data points in Figure 4.6*b*.

This complex dependence of coordination polyhedra volume as a function of increasing temperature is not fully understood, but it indicates that the ionic radius of the occupying cation may not be the most important parameter to consider as suggested from the long-range structural view (Figure 4.5). For example, the volume of the *8a* polyhedra in $NiAl_2O_4$ decreases as inversion increases (red data points in Figure 4.6*b*) when occupied by the larger Ni ion instead of the smaller Al ion; according to the previous model, the relative volume of this polyhedra should increase in size as the larger Ni atom moves into the *8a* site. Rather than the ionic radius of the cation within the newly formed polyhedra,

the volume appears to be more dependent on the bond strength of the resulting atomic arrangement. The most simple, *ad hoc* calculation for bond strength can be obtained based on Pauling's rules,[73] the *strength of the electrostatic valence bond* is given by the cation's charge divided by its coordination number. However, more recently it has been shown that the strength of a bond in a crystal structure is also related to its length,[111, 112] with ions at shorter distance forming a stronger bond.[113] In the spinel structure, the octahedra have higher coordination numbers and usually longer bond distances between oxygen and cation than the tetrahedra.[114] This, combined with the aliovalency of the cations, results in a variety of bond strengths and complex consequences to their rigidity: the strongest bonds occur in Al^{3+} tetrahedra (bond strength of 0.75 e.s.u.) and the weakest bonds in the Mg^{2+} or Ni^{2+} octahedra (bond strength of 0.33 e.s.u.). During heating, the volume modifications of the 5 polyhedra are consistent with the less rigid octahedra expanding readily with increasing temperature, while the more rigid tetrahedra expand only sluggishly or even shrink as in the case of the Al^{3+} tetrahedra in both samples. Further research of combined experiments and modeling is needed to fully understand the complex behavior of coordination polyhedra volume associated with thermally induced disorder. The data provided by this study, however, show that long-range analysis is insufficient to capture the changes of individual polyhedra that occur with increasing temperature.

Conclusions

In situ neutron total scattering experiments were performed as a function of increasing temperature up to ~1000°C to characterize inversion and the associated atomic-scale disordering processes in spinel during heating. Neutron diffraction results confirm

previously reported long-range structural behavior with ordered, "normal" $MgAl_2O_4$ ($i \sim 0.225$) becoming more inverse above 600°C, while "inverse" $NiAl_2O_4$ ($i \sim 0.875$) shows reduced inversion above 800°C. Beyond these critical temperatures both the inversion parameter, i, and the anion parameter, a, exhibit a linear behavior as a function of increasing temperature, driving the structure towards a fully disordered, random state. Neutron pair distribution function (PDF) analysis reveals that inversion changes during heating are expressed in the atomic-scale structure by a distinct phase transformation process. Increasing inversion and disordering with temperature proceeds in $MgAl_2O_4$ by a transformation of an ordered cubic phase ($Fd\bar{3}m$) to a more disordered tetragonal phase ($P4_122$). The reverse phase behavior is observed in $NiAl_2O_4$, for which inversion is reduced with increasing temperature. These findings are in excellent agreement with previously reported results on spinels disordered by changes in chemical composition. In both cases, the evolution of the inversion parameter (and anion parameter) over the long-range is expressed at the short-range by changes in the $P4_122$ phase fraction. This can be understood by fundamental crystal chemistry rules, independent of whether the disordering process is intrinsic (change in chemical composition) or extrinsic (temperature exposure). Except for fully ordered, "normal" ($i = 0$) and "inverse" ($i = 1.0$) spinels, both cubic and tetragonal phases always coexist, and their relative abundance is a measure of disorder in the structure. This means that the local structure of a partially disordered spinel consists of five distinct coordination polyhedra instead of the two predicted by the conventional long-range view. These polyhedra change their volume upon heating with a complex dependence on thermal expansion, cation movement (inversion), and polyhedral rigidity.

Chapter 5

Neutron Total Scattering Characterization of Irradiated $MgAl_2O_4$ and $NiAl_2O_4$ Spinel Chemical Solution Series

Abstract

Oxides that adopt the spinel crystal structure (AB_2O_4) are used in a variety of industrial applications that depend on their resistance to structural degradation under extreme conditions. Previous studies have shown that the spinel structure is particularly resistant to amorphization, because the oxide can tolerate significant cation disorder without loss of crystallinity through inversion. In this study, we have utilized swift heavy ion irradiation to induced disorder across the cation sublattice of a $Mg_{1-x}Ni_xAl_2O_4$ spinel solid solution series. The large penetration depth of energetic ions produces sufficient powder for neutron total scattering, which allows for the investigation of both the average structure as well as the short range order with excellent resolution to all atomic constituents. After irradiation a significant increase in cation inversion ($i>0.66$) was measured at the long-range, which is accompanied by an increasing tetragonal local phase fraction. This anti-site disordering was accompanied by additional cation Frenkel defects in a normally vacant octahedral site. The additional disorder in the octahedrally coordinated cations appear to be a consequence of the sudden change in inversion when exposed to 2.2 GeV Au ions.

Introduction

Oxides with stoichiometry (AB_2O_4), belong to a family of materials that are isostructural with the mineral magnesium aluminate spinel ($MgAl_2O_4$). These ceramics have desirable physical properties such as high melting temperature, high hardness, low density, enhanced chemical and structural durability, as well as efficient cation transport, which makes them attractive for many technologies related to catalysts[115], protective

coatings[10], battery cathodes[116], and inert actinide transmutation matrix in advance nuclear reactors[117]. Material degradation under harsh environments is a critical concern in many of these applications, and characteristics of the spinel structure, in particular cation vacancies and related disorder, play an important role in the observed material response[118].

The AB_2O_4 spinel structure, a derivative of the rock salt structure, is described by the cubic $Fd\bar{3}m$ space group[18, 19]. In this structure, the oxygen atoms occupy the 32*e* Wyckoff site, forming an almost ideal cubic closed-packed arrangement. This configuration yields 96 total interstices (64 tetrahedral and 32 octahedral) only 24 of which are normally occupied by cations. Eight cations occupy the "A-site" (*8a*) representing an eighth of the tetrahedral interstices and sixteen cations occupy the "B-site" (16*d*), half of the octahedral interstices. The other interstitial sites, normally not occupied in the structure, are the octahedral *16c* and the tetrahedral *8b* and *48f* Wyckoff positions. The spinel structure can normally be described by three structural parameters: (1) the length of the cubic unit cell *a*, (2) the distortion of the oxygen away from an ideal cubic close-packed lattice *u,* (3) and the amount of cation anti-site defects in the structure, represented by the inversion parameter *i,* Eq 1. Inversion is the primary mechanism for disordering in the spinel structure and represents the fractional amount of B cations that are present in the A site [20].

$$[B_i A_{1-i}]^{IV}[A_{i/2}B_{1-i/2}]_2^{VI}O_4 \qquad [1]$$

Spinels are commonly categorized by the inversion parameter with compositions described as "*normal*" for *i*=0 or "*inverse*" for *i*=1, while a true random arrangement of cations occurs for *i*=2/3.

The inversion mechanism, often probed through long-range X-ray or neutron diffraction experiments, is conventionally considered as the exchange of tetrahedrally-coordinated cations with octahedrally-coordinated cations (and *vice versa*). In early thermodynamic studies on $MgAl_2O_4$, however, a discrepancy was found between the residual entropy predicted from phase equilibrium experiments and experimental data from spectroscopic measurements, which was attributed to the ionic nature of the bonding and associated short range cation ordering in a partially inverted spinel structures[26]. Further details on the structure of this local ordering effect was later revealed by Raman spectroscopy on inverse $NiAl_2O_4$ and $NiFe_2O_4$ spinels with spectra that contained a higher number of active Raman modes than permitted by the $Fd\bar{3}m$ space group, indicative of a lower symmetry space group[17, 69]. The lower symmetry structure tetragonal $P4_122$ was proposed based on DFT calculations as being the lowest energy configuration for inverse spinels[70]. The existence of a tetragonal $P4_122$ coordination polyhedra environment was experimentally confirmed through neutron total scattering[71]. Partially disordered spinels with some degree of inversion are characterized locally by a phase mixture of $Fd\bar{3}m$ and $P4_122$ with the phase fraction of the latter being directly tied to the level of long-range inversion, independently whether inversion was induced by intrinsic disordering[71] or extrinsic [77]disordering means. The existence of the tetragonal $P4_122$ coordination polyhedra environment in inverse spinels was explained by straightforward application of Pauling's rules for ionic compounds, suggesting that the atomic arrangement in disordered materials is not represented by the observable long-range structure[74]. Given the distinct

charge and size of the atomic constituents, disorder cannot be random at the local scale and cation exchange is realized by the creation of new atomic sites.

The ability for spinels to accommodate structural disorder without significant change in crystallinity or physical properties has made them attractive materials for application in nuclear environments[119]. For example, it was suggested that damage from neutron irradiation in $MgAl_2O_4$ results in point defect formation with vacancies and interstitials that efficiently recombine with negligible volumetric swelling[50]. The resilience of $MgAl_2O_4$ under neutron irradiation was explained by the ability for Mg and Al to occupy both the 8*a* and 16*d* sites without causing significant changes to the unit cell of the structure [26]. Under extremely intense neutron irradiation, the cations tend to become completely randomly arranged between the available sites (i~0.66), with measured ranges of i=0.59 to i=0.69 after neutron exposure to 53 and 249 displacements per atom (dpa), respectively[51].

The radiation response of spinel, however, is strongly temperature dependent with more pronounced structural changes at lower temperatures which can be attributed to reduced atom mobility, limiting vacancy interstitial recombination. Yu *et al.*[52] demonstrated for the first time that irradiation with low energy ions (400KeV Xe^{2+}) at 100-120K leads to the amorphization of spinel, $MgAl_2O_4$, following a transformation to a potential metastable phase. This result was confirmed during a second experiment on a stoichiometric and a non-stoichiometric spinel sample (400 KeV Xe^{2+} ions, $MgAl_2O_4$ and MgO $3Al_2O_4$) by Devanathan *et al.*[53]. Changing the stoichiometry away from ideal AB_2O_4 improved amorphization resistance, but the previously reported metastable phase still formed after irradiation[54]. This phase was later studied using transmission electron

microscopy by Ishimaru *et al.* [55] and determined to be a disordered rock salt structure (*Fm-3m*), in which oxygen atoms relax to an ideal cubic close packed lattice, and the tetrahedral A-site cation migrates to the *16c* octahedral vacant site. The resulting atomic arrangement is, therefore, isostructural with defect NaCl-type rock salt (*Fm-3m*) with both cations and vacancies, randomly occupying the *4a* octahedral sites. Authors postulate that the rock salt transformation in spinels under irradiation is similar to degradation as seen in Lithium bearing battery spinel materials and spinel after extreme cation movement after extensive cycling, in which they transform into disordered rock salt structures[120].

Early studies on the radiation response of spinel-structured compounds have focused on irradiation with neutrons and low-energy (keV-MeV) ions, which lose their energy in a material predominantly through elastic nuclear interactions. This mechanism directly displaces atoms in a material creating dense cascades of interstitials and vacancies[57]. A significantly different regime is induced in materials by energetic heavy ions which deposit an exceptional amount of energy into the electronic subsystem of a solid over sub-picosecond timescales. This energy deposition causes electronic excitation and ionization processes, which creates an electron-hole plasma and modifies the potential energy landscape with structural relaxations that are otherwise inaccessible[121]. The energy is finally transferred to the atomic subsystem through electron-phonon coupling which triggers lattice heating and rapid quenching processes[58] along the ion path, leading in many insulators to permanent structural modifications within cylindrical tracks of a few nanometers in diameter. Depending on the material, the track-damage morphology can be

characterized by point defects, distinct crystalline phases[59], or crystalline-amorphous transformations[60].

The response of spinel to highly ionizing swift heavy ions appears to deviate significantly from radiation effects induced by displacive neutrons and low energy ions. Unit cell swelling was reported for single crystal $MgAl_2O_4$ exposed at room temperature to 72 MeV Iodine ions[61], and at higher ion energies (350 Mev Au) amorphization with volumetric expansions of 35%, and metastable phase formation was revealed by TEM characterization [62]. This metastable phase was identified as defective rock salt in agreement with previous low-temperature irradiations using low-energy ions[63]. The formation of a defective rock salt phase after room temperature swift heavy ion irradiation was controversially discussed in literature[64, 65] as the occurrence of rock salt was only confirmed across the long-range structure based on x-ray diffraction measurements, while Raman spectroscopy revealed the persistence of the spinel structure across the short-range [66] under the same radiation conditions.

This study presents a comprehensive structural investigation of a $Mg_{(1-x)}Ni_xAl_2O_4$ series with various degree of pre-existing inversion exposed to swift heavy ion irradiation. The use of 1.64 GeV Au ions with a large penetration depth produces sufficient samples mass (~100 mg) for neutron total scattering experiments at the Spallation Neutron Source. The analysis of diffraction and pair distribution function data provides detailed insight into structural modifications across all spatial length scales. The results show that disordering in spinel induced under such highly non-equilibrium conditions is distinct from that obtained by more conventional disordering means (*i.e.*, by chemical substitution or thermal

treatment). The relative radiation resistance increases in the $Mg_{(1-x)}Ni_xAl_2O_4$ series if Mg is replaced by Ni as evidenced by smaller structural modifications when comparing data before and after ion irradiation.

Results

Neutron total scattering structure functions (Figure 5.1) of the unirradiated $Mg_{1-x}Ni_xAl_2O_4$ compounds confirm that all samples have the spinel structure with only minor NiO impurities (<0.02 wt %) in all Ni-bearing samples. A detailed discussion on the structural properties and chemical-induced disorder in this series can be found elsewhere [71]. The overlay of pristine (black) and irradiated data (red) shows the effect of swift heavy ion irradiation across the long-range structure. The intensity of the diffraction peaks is altered by irradiation, and peaks with odd indices broaden slightly. For $MgAl_2O_4$ and $Mg_{0.6}Ni_{0.4}Al_2O_4$ the diffraction peaks shift after irradiation to larger Q values which indicates radiation-induced contraction to the unit cell parameter. For $Mg_{0.4}Ni_{0.6}Al_2O_4$ and $NiAl_2O_4$, the peak shift after irradiation is towards lower Q values associated with unit cell swelling. No peak extinction or appearance of new peaks, characteristic of phase transformations, is observed, and the spinel structure is fully retained after ion irradiation across the long range. No pronounced diffuse scattering of an amorphous phase is apparent in the diffraction data; however, a weak and broad diffuse band is observable around the most intense diffraction peak in all compositions.

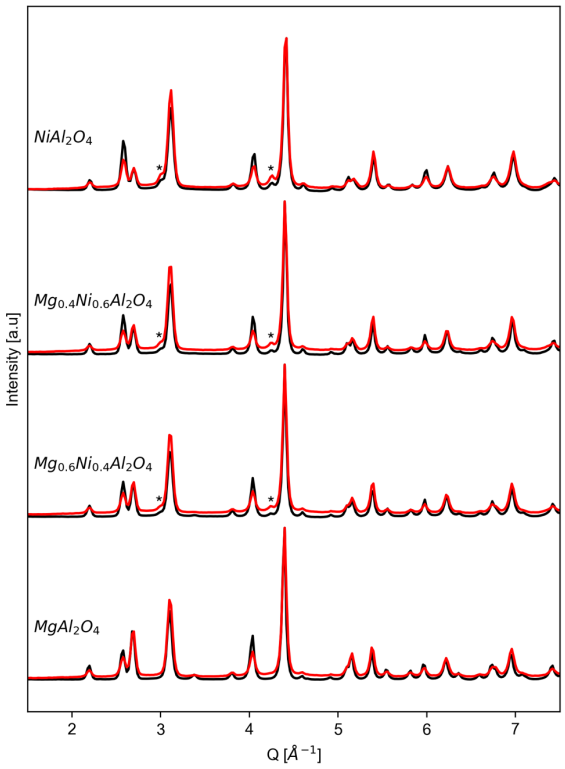

Figure 5.1: Neutron total scattering structure functions of the spinel compositional series before (black) and after (red) swift heavy ion irradiation. Small diffraction peaks denoted with an asterisk are due to a minor NiO impurity phase (less than 0.02 w%).

To better quantify radiation-induced material modifications, Rietveld refinements were performed on the neutron diffraction data before and after irradiation as shown for the $MgAl_2O_4$ sample in Figure 5.2. The conventional $Fd\bar{3}m$ spinel structural model was used (results are summarized in Table 5.1, which includes three important parameters for describing disorder in spinel: unit cell (a), oxygen displacement (u), and inversion (i). The refinement confirms that the diffraction patterns of all irradiated samples can be well modeled with the spinel structure. The unit cell parameter, which prior to irradiation exhibited a decreasing linear trend with increasing Ni content (Figure 5.3a), shows a complex behavior after irradiation, with $MgAl_2O_4$ exhibiting the largest difference to the unirradiated reference samples (Figure 5.3a). The unit cell of the two Mg-rich compounds contracts, while it expands for the two Ni-rich samples. The oxygen displacement parameter (Figure 5.3b) shows a linear decrease in the pristine samples with increasing Ni content, which is also the case after irradiation; however, the values are distinctly lower in the irradiated samples with a reduced slope and smaller changes in u before and after irradiation with increasing Ni content, most pronounced in the $NiAl_2O_4$ endmember. The magnitude of the oxygen displacement, u, is dependent on the radius of cation species occupying the tetrahedral and octahedral sites in spinel [20]. When smaller cations occupy the tetrahedral site, the oxygen relaxes towards that cation reducing the u parameter. This effect is seen in the pristine sample where increasing nickel content increases inversion and, therefore, drives the smaller aluminum cation into this site. An additional reduction in u parameter after irradiation suggests radiation induced changes to the cation partitioning and inversion between sites in the structure.

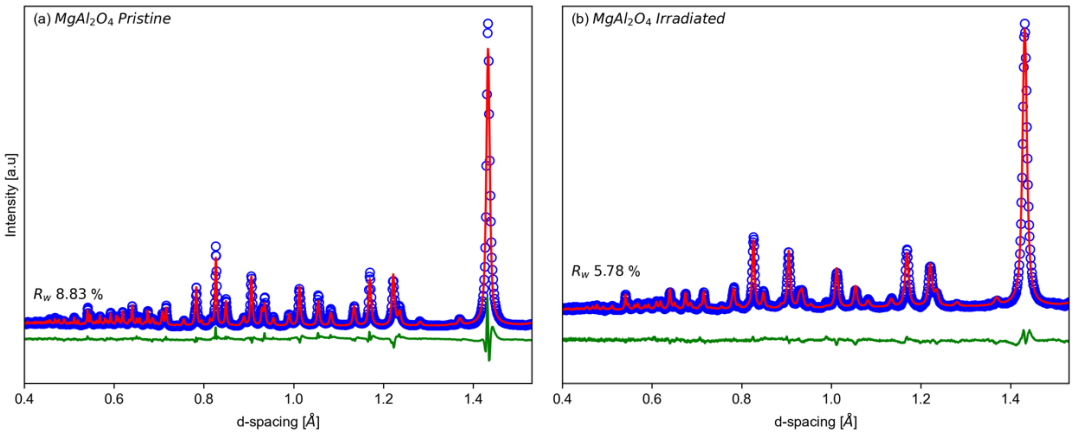

Figure 5.2: Rietveld refinement results from neutron diffraction data on pristine (a) and irradiated (b) $MgAl_2O_4$ spinel. The blue circles represent collected data and the red line the refined structure. The green line is the difference curve between experiment and model as quantified by the goodness-of-fit parameter R_w. All spinel compositions were refined with the same $Fd\bar{3}m$ model and refined parameters are summarized in Table 5.1.

Table 5.1: Rietveld refinement results of neutron diffraction data for all pristine and irradiated spinel compositions. Refinement was solely based on the $Fd\bar{3}m$ cubic spinel structure with no filling of vacant cation sites permitted. Structural parameters obtained are unit cell (a), oxygen displacement (u), and inversion.

Spinel Rietveld Refinement Results

Composition	*a*	*i*	*u*	R_w
		Pristine		
$MgAl_2O_4$	*8.0892(1)*	*0.37(1)*	*0.26093(7)*	*8.83*
$Mg_{0.6}Ni_{0.4}Al_2O_4$	*8.0774(2)*	*0.54(2)*	*0.2593(1)*	*9.29*
$Mg_{0.4}Ni_{0.6}Al_2O_4$	*8.0699(1)*	*0.64(2)*	*0.2578(1)*	*10.81*
$NiAl_2O_4$	*8.05707(1)*	*0.82(2)*	*0.2549(2)*	*8.27*
		Irradiated		
$MgAl_2O_4$	8.0826(1)	0.91(5)	0.2558(1)	5.78
$Mg_{0.6}Ni_{0.4}Al_2O_4$	8.0757(2)	0.96(5)	0.2542(2)	6.21
$Mg_{0.4}Ni_{0.6}Al_2O_4$	8.0714(2)	1.00(6)	0.2526(2)	6.98
$NiAl_2O_4$	8.0586(3)	1.03(3)	0.2508(2)	8.57

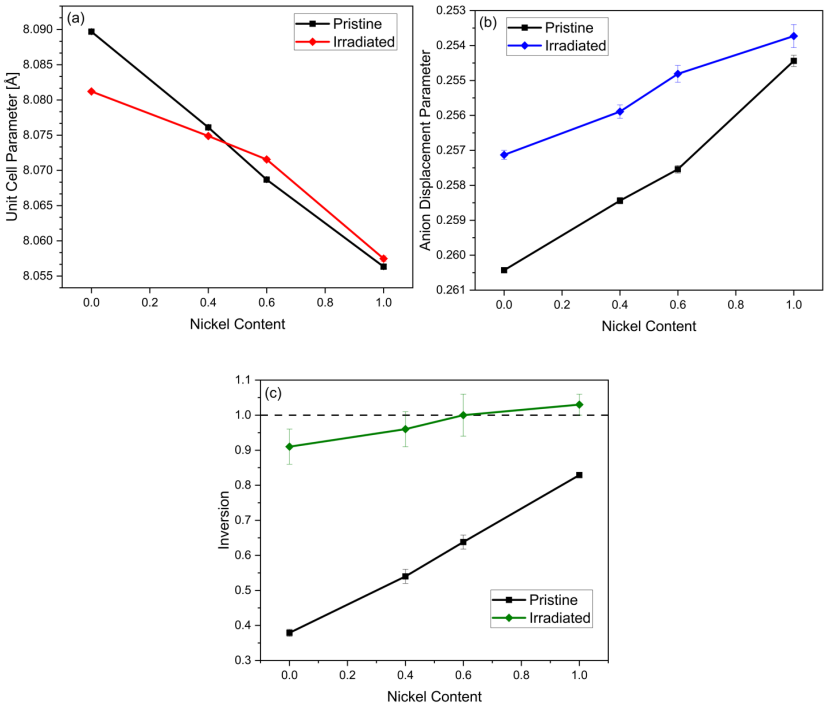

Figure 5.3: Rietveld refinement results of the structure functions of all spinel samples before and after swift heavy ion irradiation with (a) unit cell parameter, a, of pristine (black) and irradiated (red), (b) oxygen displacement parameter, u, of pristine (black) and irradiated (blue) samples, and (c) inversion parameter i of pristine (black) and irradiated (green) samples. All lines are drawn to guide the eyes and error bars represent refinement uncertainties, which are in some cases smaller than the symbol.

The inversion parameter increases linearly in the pristine samples from ~0.4 for $MgAl_2O_4$ to ~0.8 for $NiAl_2O_4$ [71]. Notably, the cation arrangement in the spinel samples does not trend towards a random distribution (i=0.667) after ion irradiation, but instead is driven to a complete inverse configuration (i~1.0 where most tetrahedral coordinated *8a* sites occupied by Al) for all compounds as shown in figure 5.3c. Dramatic increases in inversion after irradiation have been previously reported for $MgAl_2O_4$ [51, 122], with the highest previously reported value or (i = 0.77). These significant inversion values suggest the degree of order is higher compared with a more random cation arrangement.

Previous literature has shown that inversion in spinel is represented locally by a phase transformation to a tetragonal $P4_122$ structure to capture the two unique octahedral sites and the more complex oxygen displacement required to accommodate the anti-site defect [71, 77]. This information can be determined through analysis of the neutron PDFs collected simultaneously with the neutron diffraction data. The PDFs of the $Mg_{1-x}Ni_xAl_2O_4$ spinel series are shown before and after ion irradiation in Figure 5.4. Before irradiation, the peaks present in the PDFs of all samples are well-characterized by the general motif of spinel structure. The first peak at ~ 2 Å encompasses two interatomic distances: the bonds between oxygen and the tetrahedrally- (slightly smaller than 2 Å) and octahedrally-coordinated (slightly larger than 2 Å) cations. The second peak at ~2.85 Å represents the nearest neighbor oxygen-oxygen correlations (in a perfect ccp oxygen sublattice, this distance is $a_0/2\sqrt{2}$ or ¼ of the face diagonal).

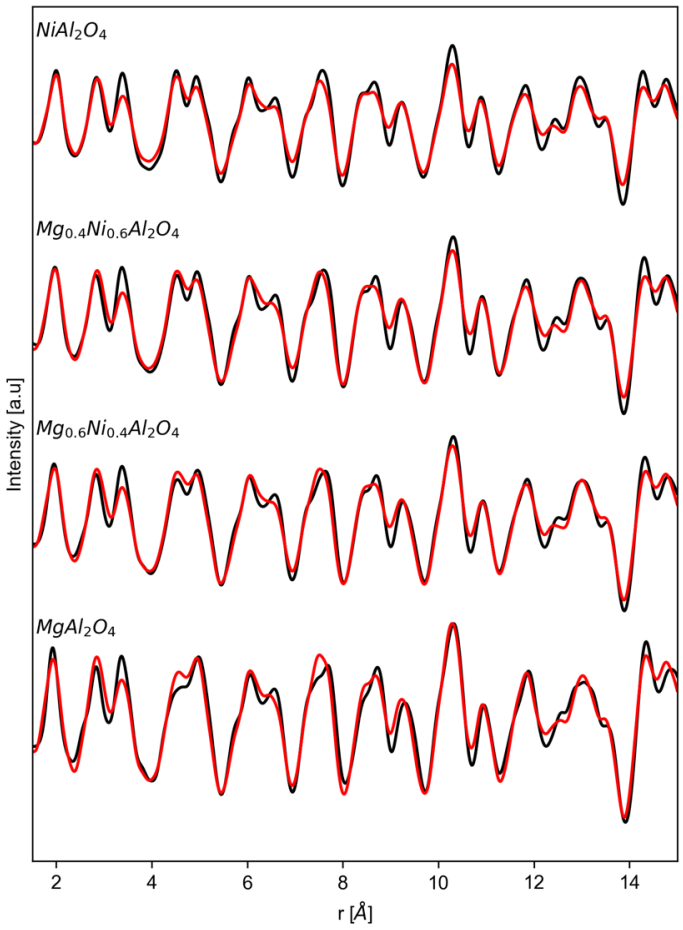

Figure 5.4: Neutron pair distribution functions for the spinel chemical series before (black) and after (red) swift heavy ion irradiation.

The third peak arises from four correlations: the tetrahedrally-coordinated cation (i) with other tetrahedrally-coordinated cations, (ii) with oxygen (2nd nearest neighbor) and (iii) with octahedrally-coordinated cations as well as (iv) octahedrally-coordinated cations with oxygen (2nd nearest neighbor). After irradiation, the relative intensities of the peaks in the PDFs for all compositions exhibit differences from the PDFs of the unirradiated samples, with the most notable features being the relation between the two peaks at ~2.7 (peak 2 above) and ~3.5 Å (peak 3 above) and the three-peak feature at 13 Å. For the PDFs of the more Mg-rich samples, in particular, the first pair correlation at ~2 Å (peak 1 above) is broader after irradiation.

To model these systematic changes to the pair correlations, the pair distribution functions were fit using PDFGUI to extract information on changes to the local atomic ordering, shown in Figure 5.5. A two phase model which includes a "normal" cubic $Fd\bar{3}m$ phase and a "inverse" tetragonal $P4_122$ phase was used, and the results are summarized in Table 5.2. The small box modelling results are in agreement with the Rietveld refinement of the long range structure. The changes seen in the experimental PDFs after ion irradiation are accurately modeled with a tetragonal $P4_122$ phase, which is expected for highly inverted spinels, as shown for the $NiAl_2O_4$ sample in Figure 5.5; however, some deviations between the collected data and the refined structure are apparent after swift heavy ion irradiation which leads to a worse goodness of fit parameter. These differences are most prominent in the region of 8-11 Å where the modelled peak intensity is incorrect for the peaks at 8.45, 8.65, and 9.21 Å.

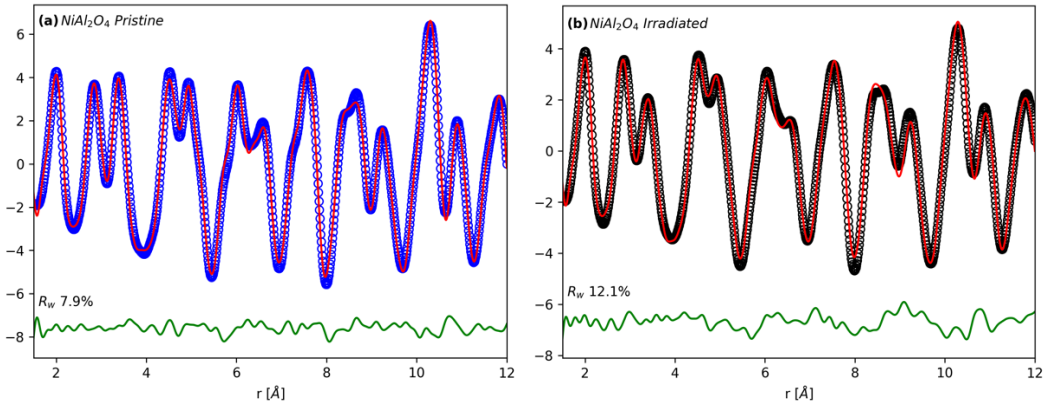

Figure 5.5: Fitted pair distribution functions on the pristine (left) and irradiated (right) $NiAl_2O_4$ spinel sample, using a two phase model. The blue circles represent collected pristine data, the black circle the irradiated, and the red line is the refined structure. The green curve represents the difference between the observed and calculated pdfs.

Table 5.2: Small box modeling results of neutron PDF analysis for all pristine and irradiated spinel compositions. Refinement was based on a two phase model with a "normal" $Fd\bar{3}m$ cubic spinel structure and a "inverse" $P4_122$ tetragonal structure with no filling of vacant cation sites permitted. Structural parameters obtained are unit cell (a) and the phase fraction of the tetragonal phase.

	Pristine			***Irradiated***		
	a	*Phase Fraction*	R_w	*a*	*Phase Fraction*	R_w
$MgAl_2O_4$	*8.089 (0.018)*	*0.39 (0.15)*	*5.28*	*8.0801 (0.02)*	*0.91 (0.5)*	*8.57*
$Mg_{0.6}Ni_{0.4}Al_2O_4$	*8.079 (0.0023)*	*0.52 (0.063)*	*9.26*	*8.081 (0.0027)*	*1.00 (0.0031)*	*8.66*
$Mg_{0.4}Ni_{0.6}Al_2O_4$	*8.073 (0.0021)*	*0.63 (0.062)*	*7.4*	*8.081 (0.0027)*	*1.01 (0.01)*	*10.27*
$NiAl_2O_4$	*8.064 (0.0022)*	*0.86 (0.027)*	*7.89*	*8.0702 (0.003)*	*1.02 (0.02)*	*12.08*

In order to gain more insight into any deviations in the "inverse" tetragonal local arrangement in irradiated spinels, more detailed PDF refinements were done on the series end members ($MgAl_2O_4$ and $NiAl_2O_4$). Although disorder in the spinel structure is primary accommodated through inversion, cation anti-site defects, in extreme disordering processes cation Frenkel defects may potentially form in which a cation is trapped at the otherwise vacant octahedral site. For the tetragonal local structure this cation in the vacant site must originate from one of three distinct starting positions: (1) the octahedrally coordinated Mg/Ni cation (2) the tetrahedrally coordinated Al cation (3) the octahedrally coordinated Al cation. These three potential cation exchange pathways are shown in Figure 5.6. As has been previously shown for unirradiated spinel oxides[74], one of these three defect structures is likely preferred as a result of the strong ionic bonding in these materials. To identify which of these local arrangements is favored in the irradiated spinel oxides, three PDF refinements were done each a distinct defective tetragonal phase that would result from on the of the three possible cation exchanges to account for the local displacement about the cation anti-Frenkel defect. All three models generally reproduce the data well and the differences in the quality between these fits are too subtle to determine simply from the R_w values of the small-box refinement.

To more effectively examine the differences between these structural models, a correlated difference approach was taken (Figure 5.7). This method evaluates not only the difference between the refined and measured structures but also how significant those differences are over certain regions of real space [123].

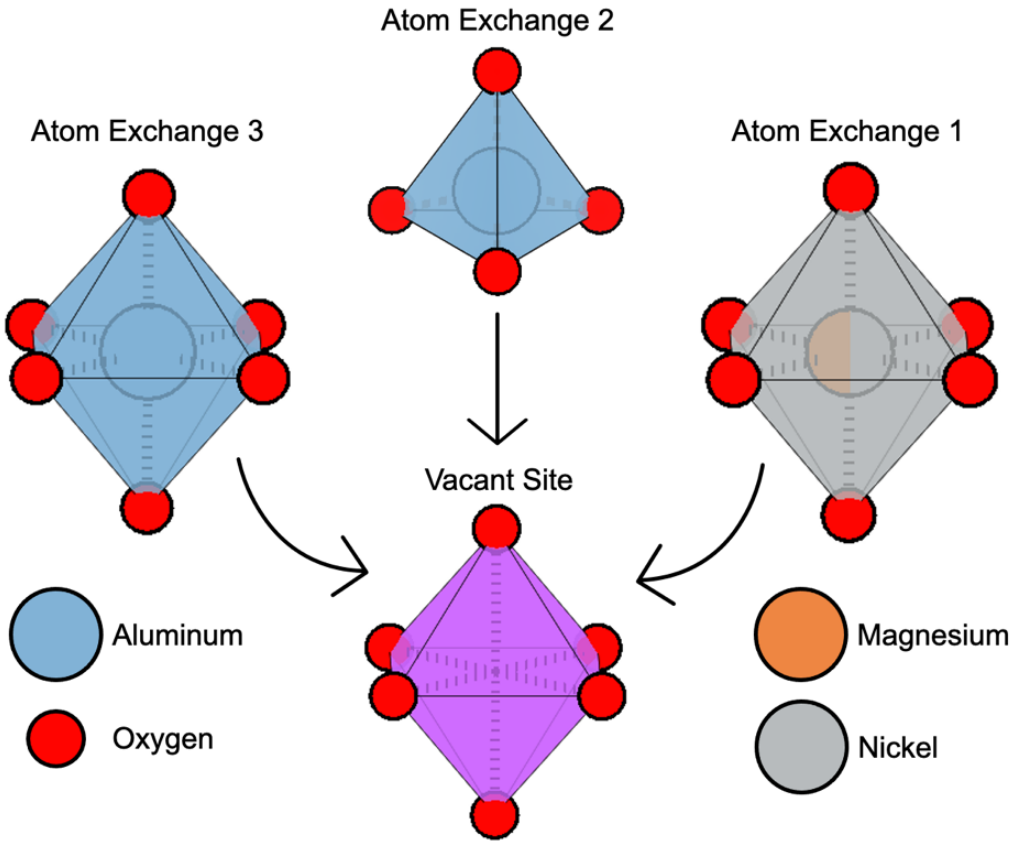

Figure 5.6: Diagram of the possible cation exchanges with the vacant octahedral site in the disordered tetragonal structure. Atomic structures generated using the VESTA software package [124].

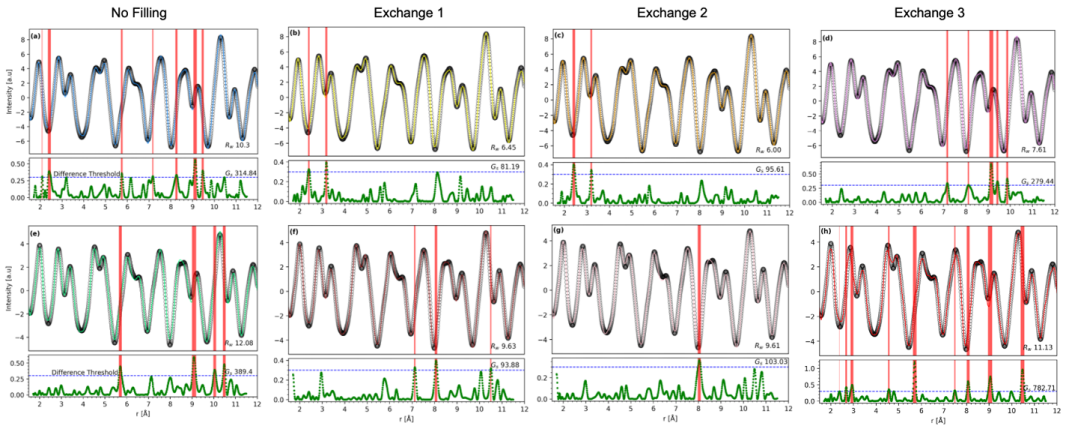

Figure 5.7: Fitted pair distribution functions of irradiated $MgAl_2O_4$ (top) and $NiAl_2O_4$ (bottom) using different disordered tetragonal models, outlined in diagram 8. Black circles represented the collected data from the respective irradiated samples. The colored line is the model fit. The green curve in the lower panel represents the correlated difference and the blue dashed line is the threshold for structural difference, which is determined from the uncertainty in the collected data. Regions where the corelated difference exceeds the threshold are highlighted in red

The advantage of using a correlated reliability factor (G_s), shown in green under the PDF, instead of the conventional R-factor for the PDF analysis is that the R-factor is based on the presupposition of uncorrelated errors, whereas G_s accounts for systematic correlations within the difference curve, distinguishing between insignificant differences caused by statistical artefacts and significant differences caused by mismatches between the experimental data and the models. In Figure 5.7, the regions highlighted in red show areas of the pattern where differences between the model and experimental data are correlated and statistically significant.

For the "inverse" tetragonal models with no Frenkel defects, previously noted significant difference between the fit and the collected data for $MgAl_2O_4$ and $NiAl_2O_4$ between the regions of 8 and 11 Å are highlighted as well as more subtle differences at 5.76 Å and 2.41 Å. These model mismatches are alleviated by refining with a disordered tetragonal structure that allows either cation exchange 1 or cation exchange 2 as diagramed in Figure 5.6. A disordered structure with cation exchange 3, where the Aluminum in the octahedral site can move to the vacant position, produces no significant improvement and is a worse fit than the model with no Frenkel defects for $NiAl_2O_4$. The differences between the disordered models that allow for cation exchange one or cation exchange two are less stark. For both $MgAl_2O_4$ and $NiAl_2O_4$, cation exchange 1 produces a fit that has a lower corelated difference, G_s, to the collected data. The most accurate representation of the local structure of collected data for the irradiated spinels, therefore, is a highly inverted $P4_122$ tetragonal structure with some additional disorder which is best described by cation Frenkel defects between the 4*a* Mg/Ni cation and the otherwise vacant octahedral site, which has a

refined fractional atomic occupancy of 20% Mg and 26% Ni cations in the chemical series endmembers. The Al cations in the disordered structure remain in their respective *4b* and *4c* sites.

To investigate the possibility of radiation-induced cation Frenkel defects effecting the long range refinement, the diffraction data were refined with a structural model that allowed for cation movement into the vacant *16c* site. Since additional cation exchange among *8a* and *16d* sites is permitted as well, site occupancies can no longer be obtained with respect to cation species due to parameter constraints, and only the average cation neutron scattering length at each site determined. Rietveld refinements with an improved goodness of fit were obtained across all irradiated compounds by including cation Frenkel defects and partial filling of the cation vacancy. These results are unique to disordering mechanisms with highly transient regimes and is distinct from chemical-induced [71] or thermal-induced disorder[77], which is only characterized by cation antisites and increased inversion with no model improvement from the addition of cation Frankel defects. The measured neutron scattering length from the vacant site in the spinel chemical solution series is shown in Figure 5.8. With increasing Nickel content, the scattering length at the vacant site increases, which implies either that more cation Frenkel defects are produced (vacant site occupancy increases); or Mg and Al at this site is more and more replaced by Ni (largest scattering length among all three cations). It is likely that the increased scattering length across the chemical series is from a preference for Ni in the vacant site as the Ni containing samples showed little change after irradiation, which suggests that the number of Frenkel defects is not increasing with Ni content.

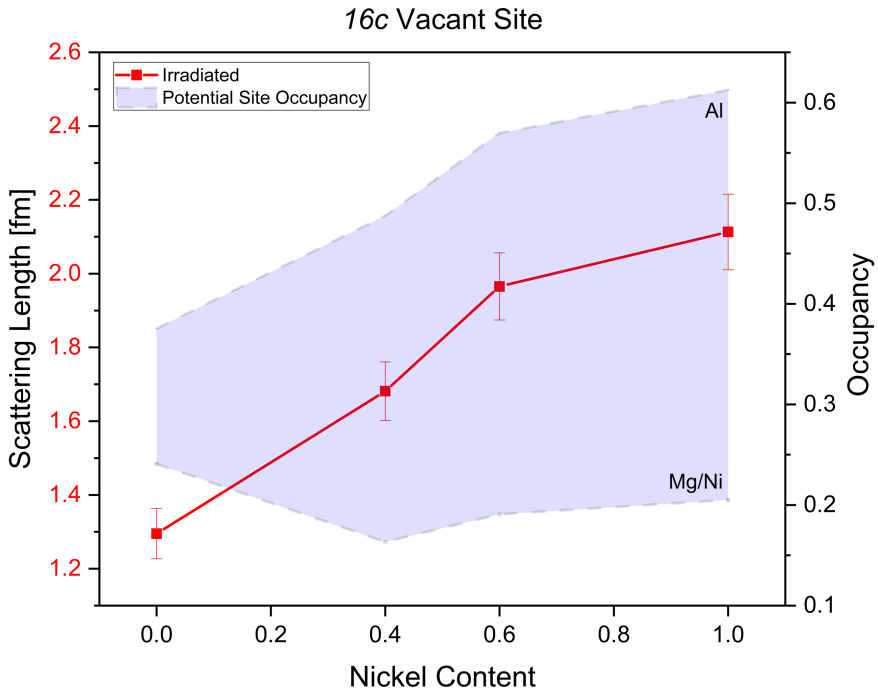

Figure 5.8: Refined average neutron scattering length of the fractional occupant of the normally vacant 16c site after irradiation from neutron diffraction data. The area shaded in blue represents the region of possible occupancy calculated from scattering lengths of all three cations (Al, Mg, and Ni) according to possible distributions (lower bound filled with Mg/Ni and upper bound filled with Al). All error bars represent the uncertainties from the Rietveld refinements.

Given the scattering lengths of each cation, the maximum and minimum occupancies of the *16c* site were determined for different scenarios (blue shaded region). If predominantly the large scatterer Ni/Mg move into this site, an average occupancy of about ~20% can be expected across the series, which agrees with the local defective structure determined through small box modelling.

Additional disordering from cation Frenkel defects is also reflected in the oxygen parameter, *u*, which normally is solely dependent on the inversion parameter[20]. Previously literature on annealing swift heavy ion irradiated spinel ($MgAl_2O_4$, $MgCr_2O_4$) has noted an additional lower temperature recovery step of the oxygen displacement parameter that is not related to inversion [125]. The measured oxygen displacement of the spinel chemical solution series before and after irradiation and a comparison to the derived relationship with from literature is shown in Figure 5.9. In the pristine sample, the oxygen displacement is slightly higher than reported literature values but the trend with changing inversion is consistent with literature. After swift heavy ion irradiation, the oxygen parameter decreases from the measured value before irradiation and deviates from the expected trend with literature. The measured oxygen parameter is larger than would be expected for the cation arrangement post irradiation. This is consistent with additional octahedral cation Frenkel defects as the oxygen atom will relax towards the empty octahedral site and away from the ideal cubic close packed position.

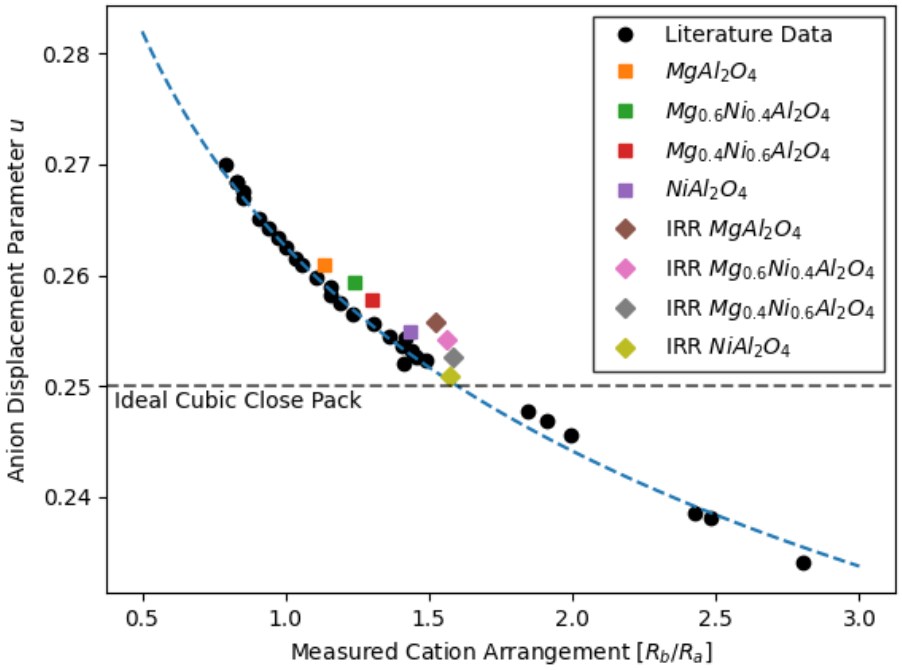

Figure 5.9: Measured anion displacement parameter from Rietveld refinement of neutron diffraction data before and after irradiation. The black circles and the blue dashed line are the data and derived structural relationship between the anion displacement parameter and the measured cation arrangement from Sickafus et. al[20].

Discussion

Exposure to 2.2 GeV Au ions modified the unit cell, atomic positions, and cation partitioning in $Mg_{1-x}Ni_xAl_2O_4$ with no evidence of amorphization. For spinel oxides disordered through high-temperature[77] or neutron irradiation[51], cations generally tend toward a random arrangement (i = 2/3) of magnesium, nickel, and aluminum distributed among the two available sites (*8a* tetrahedra and *16d* octahedra). For "normal" spinels (i = 0), this corresponds to an increase in the inversion parameter and for "inverse" spinels (i = 1), a decrease. In contrast, the results from Rietveld refinement and pair distribution analysis of our data show that the spinels irradiated with 6×10^{12} swift heavy Au ions/cm^2 are all highly inverted ($0.667 < i < 1$). Additionally, both analysis techniques reveal filling of the nominally vacant octahedral *16c* site. These two results, high levels of inversion and the presence of cation Frenkel defects isolated to the octahedrally-coordinated sites and not the tetrahedrally-coordinated sites, are significant deviations from previously reported literature on ion-irradiated spinel oxides.

The energy of ion used for irradiation studies has a significant influence on the volume of ion-matter interaction and the energy density radial profile induced therein. Previous studies on swift heavy ion irradiation effects in spinel used ions in an energy range of 70 MeV - 765 MeV [62, 66, 126, 127] and generally revealed either an increase in disorder through increasing inversion or a phase transition to a disordered rock salt structure after irradiation. The different reported irradiation effects are the result of the *ex situ* technique used to measure the structure. Average structure analysis through x-ray diffraction or electron diffraction report a phase transition to a disordered rock salt structure after

irradiation, whereas, local structural probes like Raman spectroscopy are shown to measure a disordered spinel structure after irradiation. These discrepancies have been cited in literature as the result of the similar scattering intensity of Magnesium and Aluminum and anti-phase boundaries effecting the results of the diffraction techniques [66]. These boundaries are formed between the ion tracks and cause the broadening and eventual extinction of the spinel peaks in samples where the anti-phase boundary density is high.

In the present work, neutron total scattering experiments with excellent cation scattering contrast and oxygen sensitivity provided unprecedented access into the irradiated structure of spinel oxides across multiple structural length scales. This atomic sensitivity is critical in analyzing cation distributions, which strongly affects diffraction peak intensities, and polyhedral geometries, which results in changes to the PDF peak intensities and shape. To generate sufficient sample mass for neutron total scattering (~100 mg) requires the use of extremely energetic 2.2 GeV ions which fully penetrate tens of microns of material. These irradiation conditions result in large, nanometric tracks, though with less intense energy densities than would be induced for lower energy ion irradiations[128] as the higher energy secondary 'delta' electrons travel much further. In our sample, this results in much larger spinel domains and a decrease in anti-phase boundary density, prohibiting the apparent transition into rock salt normally seen in diffraction experiments on irradiated spinel. During the previously reported rock salt transformation, the peaks not associated with the rock salt structure are significantly depressed and the overall position and width of the rock salt superstructure peaks do not change[66]. The measurement of atoms at the *16c*

vacant site in these experiments is reported a result of measurements across the phase boundary and are not actually occupied by a cation.

To confirm if our results of significant changes to inversion and additional cation Frenkel defects are independent of this phenomena, Williamson-Hall analysis was performed before and after irradiation to compare the size broadening of the peaks associated with the rock salt structure, which are maintained across phase boundaries, and the spinel peaks that are diminished by these effects. The spinel reflections are odd indexed, $h + k + l = 2n + 1$, and the rock salt reflections are even indexed, $h + k + l = 2n$. The measured the full width half maxes of the even and odd peaks before and after irradiation are shown in Figure 5.10. Before irradiation the even and odd reflections have similar size and strain broadening, which results in an identical peak broadening relationship with peak position for both sets. Post irradiation, the slope of both the even and odd reflections increases from increasing microstrain broadening. Additionally, the odd reflections are shifted upward and are separate from the even reflections from a decrease in the coherent spinel domain size. From the linear fit, the spinel structure has a coherent domain size of 70nm. This size is large compared to previous irradiations; for instance, Yasuda *et al.* reported disordered spinel domain of 10 nm with a highly disordered core region of 2 nm after an irradiation with 350 MeV Au ions. The size of the spinel domains in our sample is large enough to ensure that the results from pair distribution analysis are not significantly influence by anti-phase boundary effects; therefore, the high levels of measured inversion and cation Frenkel defects are present locally in our irradiated spinel samples.

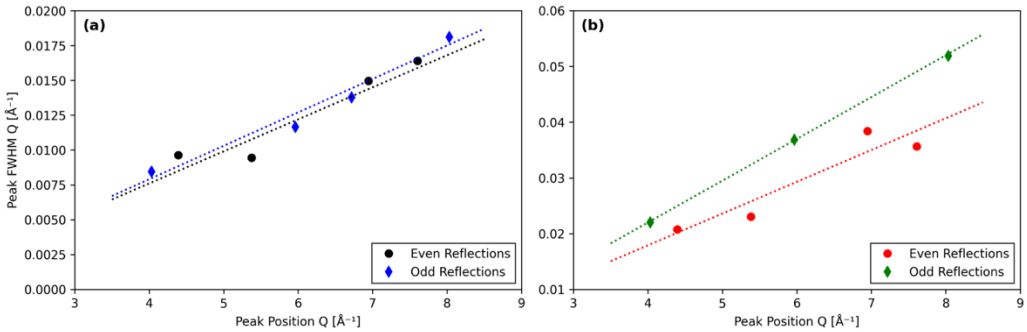

Figure 5.10: Williamson-Hall analysis of even and odd reflections in $MgAl_2O_4$ before (blue and black) and after (red and green) swift heavy ion irradiation. The dashed lines are linear fits to the collected data.

To understand the defect structures created in $Mg_{1-x}Ni_xAl_2O_4$ by 2.2 GeV Au irradiation, it is important to consider that these atomic configurations are not directly created by the ion, itself, but form as the result of rapid quenching through nonequilibrium pathways. Such GeV heavy ions deposit exceptional amounts of kinetic energy to the *electronic* substructure within a few femtoseconds. Here, the spinel samples undergo dense electronic excitations and ionizations which can, in some cases, induce local melting immediately after the energy imparted into the hot electrons couple to the phonons in the lattice. The phases studied in this paper represent the atomic configurations quenched and recovered through structural transition pathways otherwise inaccessible. It is, therefore, necessary to instead think about how the process from the amorphous structure to spinel proceeds and what interrupted that process to create the measured quenched structure.

The complete description of the unirradiated spinel structure contains 5 distinct polyhedral configurations: "normal" *8a* Mg/Ni tetrahedra, "normal" *16d* Al octahedra, *4b* "inverse" Al tetrahedra, *4a* "inverse" Ni/Mg octahedra, *4c* "inverse" Al octahedra [77] .The stability of these polydedra is correlated with the strength of the bonds that form them, which is related to the length of the bonds in the structure[111],[112]. Using the Shannon radii for the cations (Mg,Ni,Al) in tetrahedral and octahedral coordination [29], the tightest bonded polyhedral in the spinel structure is the "inverse" *4b* Al tetrahedra. The fraction of this Al tetrahedra, which is not present in the defective rocksalt structure, appears to increase significantly after irradiation from the increase in inversion seen in both the short-range and long-range refinements. This could be the result of preferred formation of this tightly bound polyhedra during the initial stages of the recovery from the hot amorphous structure.

The initial formation of individual polyhedral after amorphization through swift heavy ion irradiation is seen in other complex oxides, the resulting local structure still contain atoms bonded into polyhedra, but often these polyhedra are unable to connect in a repeating pattern, leading to a quenched amorphous structure. In the case of these spinel compositions, the quenching process could proceed with first the formation of the Al tetrahedrals, which are interlink together to from the cubic close pack anion lattice then the remaining cations position themselves in octahedral sites to approximately maintain local charge balances. The recovery proceeding in a manner similar to this would explain the very high levels of inversion measured after swift heavy ion irradiation as opposed to a random arrangement of cations.

An implication of aluminum preference for tetrahedra is the prevention of the material from adopting the rocksalt structure locally after irradiation. The presence of the spinel structure locally after swift heavy ion irradiation would be consistent with literature. In previous irradiation studies the local spinel phase was confirmed with Raman spectroscopy[66] and TEM images of the spinel structure inside of ion tracks, where the rock salt structure would have been most likely to be found, were also produced which suggested additional disordering of octahedral coordinated cations[62].

The formation of cation Frenkel defects may also be a result of the inversion process itself. During the rapid quenching after swift heavy ion irradiation cations in the process of swapping sites may be frozen in the *16c* octahedra before completing the inversion process. The local structure found after irradiation where the Ni/Mg cation is moved from its normal octahedral position to the *16c* site equivalent in the $P4_122$

tetrahedral structure is consistent with the lowest energy inversion process determined through kinetic Monte Carlo computer simulations on inverse $NiFe_2O_4$ [129]. The authors determined that the inversion process is triggered by the movement of the B site cation into the *16c* site in a face sharing position with the *8a* tetrahedral A site cation. From this high energy position, the two cations swap positions and the A site cation then migrates from the *16c* site to the *16d* site. Therefore, the most common cation pair to be occupying the *16c* and *8a* sites in our case is the observed Mg/Ni and Al cation instead of a random distribution where there is a 50% chance the pair is Al and Al, suggesting that the occupant of the octahedral sites is not random.

From the results of the chemical series, it appears the introduction of an atom that forms strong ionic bonds suppresses the structural disorder and phase transformations that arise in applications that involve extreme cation movement. The increased presence of Al tetrahedra after irradiation suggests that their inclusion in the starting structure through inversion may prevent large changes to the structure from swift heavy ion exposure. The mechanism for the inversion levels remaining above a random distribution $i = 0.66$ and the formation of Frenkel defects in the quenched sample is still not well understood; however, it is likely that at the high ion energies used in this study that these results are a frozen defect structure during the back transformation of a highly inverted spinel formed during irradiation to a normal configuration.

Conclusions

A solid solution series of spinel oxides ($Mg_{1-x}Ni_xAl_2O_4$) was exposed to highly ionizing radiation (2.2 GeV Au ions) and characterized by neutron total scattering experiments with high cation contrast and sensitivity to oxygen. The collected data, neutron diffraction patterns and pair distribution functions, were analyzed to determine both the average structure after irradiation and the local atomic arrangements through small-box refinement. The diffraction data indicate that these spinel structures exhibit resistance to amorphization but exhibit a decrease in measured peak intensity and an increase in broadening. From Rietveld refinement of the neutron diffraction patterns, the refined structure showed a significant increase in inversion not normally seen in heavily disordered spinel samples, which normally trend towards a random cation arrangement after irradiation. These changes in the spinel structure after irradiation were also observed in a similar refinement of the local cation arrangements using neutron pair distribution function analysis. In both refinement methods an improvement in the fit quality was attained through introducing additional cation Frenkel defects through the occupation of an ordinarily vacant octahedral site in the spinel structure.

From the short range modeling, local defect structure includes additional octahedral disorder with between the normally vacant site and Mg/Ni octahedral in "inverse" spinel. The origin for this defective structure may be from the preferred formation of the Al tetrahedra during the irradiation process and the filling of the normally vacant site is a consequence of quenching the inversion process itself as the material attempts to transition back into a "normal" structure. The introduction of a Ni dopant into

the $MgAl_2O_4$ spinel structure, which increase the starting inversion of the sample, appears to increase the structural resistance of the oxide to swift heavy ion irradiation, although it is unclear whether this is the result of increasing starting inversion itself or a chemical effect from the dopant.

Chapter 6

Neutron Total Scattering Study of Defect Fluorite at High Pressure

Abstract

High pressure structural transformations can cause significant, favorable changes to the physical, electronic, and magnetic properties of materials. Understanding these modifications will be critical for designing next generation materials, however, complete structural characterization at high pressure is challenging, especially on lighter elements. Neutron total scattering is a powerful tool for simultaneously analyzing both the long range average structure and the distinct local atomic arrangements, which are responsible for property changes. Despite this, neutron total scattering experiments at pressure have remained rare due to the increased complexity compared to measurements at other extreme conditions. The SNAP instrument at the Spallation Neutron Source at Oak Ridge National Laboratory is an ideal candidate for high pressure neutron total scattering as it boasts the most intense neutron flux among beamlines specialized for high pressure work. The methodology for performing such an experiment using this beamline requires few modifications to a normal diffraction experiment. High quality data can be acquired in as rapidly as 60 minutes and the data quality results in a transformed pair distribution function with a real space resolution of $0.17\ to\ 0.22$ Å depending on the sample composition and pressure.

Introduction

Materials exposed to extreme pressure display unique physical and electronic properties that result from the complex structural distortions, disorder, and phase transformations that are induced. Notable high pressure transitions have resulted in, super hard materials[130], electronic super conductors[131], and high energy density materials [132].

These resulting property changes have increased interest in fabricating next generation materials with similar structural modifications using high pressure synthesis routes [133] or through exposure to other extreme conditions. Understanding the underlying structural changes responsible for these unique properties at high pressure, is crucial for developing these methods. Structural characterization *in situ* at high pressure, however, is limited and modifications are often difficult to measure with standard x-ray diffraction techniques as they are insensitive to low Z elements, which are often critical to these transformations. Furthermore, if the structural distortions do not appear in the average long range structure few techniques are available for accurately determining local atomic and mesoscale arrangements. Currently, structural characterization across multiple length scales is commonly achieved at high pressure through a combination of synchrotron x-ray scattering techniques [134, 135], and Raman[136] or infrared[137] spectroscopy. Neutron total scattering, a technique that captures structural information simultaneously across all length scale with an increased sensitivity to low Z elements, can potentially provide valuable insight on the structure of materials at extreme pressure.

Neutron total scattering reveals both the long-range repeating structure of a materials and the local cation arrangements. This is possible through accurately measuring both the Bragg and diffuse scattering contributions from a sample. Once obtained this pattern can be Fourier transformed into real space as a Pair Distribution Function (PDF), a histographic representation of the interatomic spacing within a sample. Pair distribution functions can be used to model both the short range structure through small box modeling and the mesoscale structure through coupling with the long range Bragg diffraction through

large box modelling. A successful Neutron total scattering experiment, however, requires a high neutron flux, wide detector coverage, and extensive background measurements. These measurements at ambient conditions or at temperature extremes have become increasingly accessible at user facilities and have led to significant breakthroughs in materials science. For example, a leading instrument in this regard is NOMAD at the Spallation Neutron Source at Oak Ridge National Laboratory[84]. This instrument has enabled significant scientific contributions to the structure of light atom species on nanomaterials[138, 139], materials quenched from extreme conditions such as swift heavy ion irradiation[140] and high pressure[141], as well as, structural-property relationships in catalysts[142] and battery materials[143].

Performing similar measurements *in situ* at high pressure inside a Paris Edinburg (PE) cell [144] was initially demonstrated by Klotz et al. in 2002[145] on amorphous water ice. Experimental methodologies for high pressure total scattering experiments have been previously formalized for experiments on PEARL[146] at ISIS and on D4C[147] at Institut Laue-Langevin and these instruments have been successfully used to characterize many glassy materials[148] and more recently demonstrated for crystalline materials [149]. Published works[150-159], however, have remained rare compared to other total scattering techniques due to the increased complexity of these experiments that are unique to high pressure. These challenges are a result of the methods through which extreme pressure is applied to a sample, which can cause significant changes to the sample as it is crushed.

Neutron diffraction experiments at high pressure are most commonly performed using a PE Cell to apply pressure. Inside the PE cell the sample is contained inside a metal

gasket, often made from the null scattering alloy $Ti_{68}Zr_{32}$ (referred to as TiZr), and pressure is applied through two anvils which compress the sample inside the gasket under heavy loads. For high pressures, the anvils may move as much as a millimeter during compression which results in changes the solid angles between the detectors and the incoming neutron beam and deforms the sample and gasket as volume decreases under load. The gasket deformation is significant and can increase the outer diameter from an initial 14.5 mm to 16.5 mm under heavy loads (~90 tons), increasing the neutron path length through TiZr by as much as 4mm. These changes to the geometry and sample holder require a unique background measurement to be acquired for every pressure step that a sample is measured at. Furthermore, the required amount of compression to reach a given pressure is dependent on the mechanical properties unique to the sample and gasket; therefore, it is not possible to measure the background independent of a sample as is common in ambient conditions. Previously reported experimental methods for total scattering at high pressure solve this issue in one of two ways (1) linear interpolation of a new empty gasket and multiple compressed gaskets quenched from pressure emptied of their original sample [147] (2) measurement of a strong incoherent scatterer, Vanadium, in a gasket *in situ* at a load that results in the same anvil separation as the sample measurement[146].

We have investigated performing similar experiments on SNAP at the Spallation Neutron Source at Oak Ridge National Laboratory. The SNAP beam line has the most intense neutron flux amongst instruments that specialize in high pressure work. Additionally, Spallation neutron sources provide a significantly higher flux of neutrons at high energy, which is crucial for resolving features at high Q. The in-plane scattering

geometry of the SNAP instrument also enables accurate measurements at low Q ranges (Q < 1.5 $Å^{-1}$) that aren't possible to measure on instruments with a transverse beam path. The open nature of the sample stage of the instrument also allows for the potential of measuring the anvil separation inside the PE press to aid in reproducing the same instrument geometry and gasket deformation for the background measurements at pressure.

In order to benchmark the potential of the SNAP beamline for acquiring meaningful pair distribution functions of crystalline materials, an oxide system with structural heterogeneity across length scales was chosen to highlight the distinct local phase captured by pair distribution function analysis from the average structure determined through long range diffraction. $Y_2Zr_2O_7$ was chosen due to its strong neutron scattering and low absorption. The average structure of this material is defect fluorite, a rock salt derivative in the $Fm\bar{3}m$ space group. The Yttrium and Zirconium cations both occupy the *4a* site with an average coordination number of 7 and the Oxygen anion fills 7/8ths of the *8c* site in the space group. Previous studies on defect fluorite, however, have reported that the short-range structure is more ordered than what is suggested by the long range data, with additional peaks present in Raman[160, 161] and x-ray absorption data[162]. This local ordering was determined through neutron total scattering to be best represented by a local orthorhombic Weberite-type ($C222_1$) phase [140]. In the Weberite-like structure, cations are split among three distinct sublattices. Two of these layers are ordered, with different repeating motifs of trivalent cations in 8 coordinated *4b* sites and tetravalent cations in 6 coordinated *4b* sites. These two distinct layers are connected through a layer filled with

mixed 7 coordinated *8c* sites. The anions are distributed amongst three sets of *4c* sites with a constitutional vacancy on a fourth and 2 sets of *8c* sites.

To capture the complete structure of defect fluorite, therefore, a structural probe must be able to measure not only the long-range average structure, but also the unique local cation arrangements that appear locally. While this capability on NOMAD has been used to study this structure in detail, it is possible to accomplish the same task using the collimated 750 micron beam at SNAP, which would unlock both potential high-pressure experiments on heterogenous crystal structures and allow for significantly smaller sample masses to be required for neutron total scattering experiments.

Methods

Neutron Total Scattering Methodology

NOMAD

To provide a reference for the data produced at SNAP, an ideal experimental PDF of $Y_2Zr_2O_7$ was measured using the NOMAD instrument [84]. Polycrystalline $Y_2Zr_2O_7$ powder was loaded into 3mm quartz capillaries (0.1mm wall thickness) to a height of at least 1.5 cm. The loaded capillary was measured on NOMAD as a part of its mail in program and was exposed for 45 minutes (4.5 C) at 100K. The data was reduced using the AutoNOM program, which is an automated data reduction suite that increases user throughput. The automated nature requires the program to be agnostic of chemistry, density, and volume of the sample, which produces PDFs that are not on absolute scale and must therefore be numerically scaled to an S(Q).

These simplified PDFs, however, can be produced from total scattering patterns that require only measurements of (1) the sample $[I_{sample}(Q)]$, (2) the sample holder/instrument $[I_{holder}(Q)]$, (3) an ideal incoherent scatterer $[I_{IS}(Q)]$, Eq 1a, which can then be scaled to and S(Q), Eq 1b, using the quantity, <b> (the average neutron scattering length of the sample).

$$I(Q) = \frac{I_{sample}(Q) - I_{holder}(Q)}{I_{IS}(Q)} \quad \text{Eq[1a]}$$

$$S(Q) = \frac{I(Q) + < b >^2 - < b^2 >}{< b >^2} \quad \text{Eq[1b]}$$

A primarily incoherent neutron scatterer, $[I_{IS}(Q)]$, is used to normalize the data by the number of produced neutrons at each energy. After spallation, the neutrons are moderated by decoupled, poisoned, supercritical hydrogen, which is necessary to produce neutrons with a wide range of energies. The neutron energy spectrum is unique to the instrument and sample position. Measurement of an incoherent scatterer, such as Vanadium, produces an energy profile of the neutron source. On NOMAD $I_{IS}(Q)$, is determined using a Vanadium rod, which is positioned in the same location as the sample and doped with Nb to remove any remaining coherent scattering signal. The contributions of the Quartz sample holder and features of the instrument are removed from the sample measurement $[I_{sample}(Q)]$ by measuring an empty 3mm quartz capillary also positioned in the same location as the sample. Reproducing the exact measurement position is crucial as any changes will cause artifacts in the transformed PDF.

SNAP

$Y_2Zr_2O_7$ powder was measured on SNAP in a Paris Edinburgh cell with single toroidal, cubic Boron Nitride anvils at ambient conditions and at high pressure inside a fully encapsulated TiZr gasket, chosen for its null scattering properties. For all measurements, the west and east detector banks were positioned at 50° and 105° respectively. The chopper was set to 1.8 Å and the neutron beam was collimated with a 750 micron slit mounted on the lower anvil. For experiments at ambient conditions, the number of required measurements is consistent with a NOMAD experiment with a TiZr sample holder. $I_{sample}(Q)$ is the $Y_2Zr_2O_7$ in a TiZr Gasket and $I_{holder}(Q)$ is an empty TiZr Gasket measured in the PE Cell. $I_{IS}(Q)$ was determined through measuring Vanadium powder in a TiZr gasket. This setup requires an additional step of subtracting the empty TiZr gasket measurement $[I_{IS}(Q) = I^{Ambient}_{Vanadium\ Powder}(Q) - I^{Ambient}_{TiZr\ Gasket}(Q)]$, but ensures the Vanadium is in the same location as the sample. Powder was chosen over solid vanadium to simplify gasket loadings and requires additional data processing to remove the small coherent peaks. All ambient measurements were performed with an oil pressure of 50 bar to securely close the PE cell without significantly increasing pressure.

High pressure total scattering on SNAP, however, requires additional measurements as shown in Eq 2.

$$I(Q) = \frac{I^{HP}_{sample}(Q) - \frac{I^{HP\ Spacing}_{Vanadium\ Powder}(Q)}{I^{Ambient}_{Vanadium\ Powder}(Q)} * I^{Ambient}_{TiZr\ Gasket}(Q)}{I^{Ambient}_{Vanadium\ Powder}(Q) - I^{Ambient}_{TiZr\ Gasket}(Q)} \quad \text{[Eq 2]}$$

The incoherent scatterer term $I_{IS}(Q)$ is the same as measurements at ambient conditions. The significant complication is $I_{holder}(Q)$ at high pressure. $I^{HP}_{holder}(Q)$ cannot be directly measured as applying load to an empty gasket will cause significantly different gasket

deformation than high pressure sample, $I^{HP}_{sample}(Q)$, as TiZr will deform into the internal empty sample chamber. The high pressure empty is approximated using measurements of Vanadium powder in a TiZr gasket. If the Vanadium powder is measured at the same compression as the sample, $I^{HP\ Spacing}_{Vanadium\ Powder}$, the contributions of the gasket and features of the instrument in $I^{HP}_{sample}(Q)$ can be approximated by $\frac{I^{HP\ Spacing}_{Vanadium\ Powder}(Q)}{I^{Ambient}_{Vanadium\ Powder}(Q)} * I^{Ambient}_{TiZr\ Gasket}(Q)$. Dividing $I^{HP\ Spacing}_{Vanadium\ Powder}$ by the ambient measurement $I^{Ambient}_{Vanadium\ Powder}(Q)$ removes the Vanadium incoherent scattering contribution and multiplying by $I^{Ambient}_{TiZr\ Gasket}(Q)$ removes the ambient TiZr gasket contribution in $I^{Ambient}_{Vanadium\ Powder}(Q)$. The same $I^{HP}_{holder}(Q)$ pattern could also be obtained by dividing $I^{HP\ Spacing}_{Vanadium\ Powder}$ by $I_{IS}(Q)$. The more complex representation was chosen as the quotient $\frac{I^{HP\ Spacing}_{Vanadium\ Powder}(Q)}{I^{Ambient}_{Vanadium\ Powder}(Q)}$ produces a straightforward visualization of the changes to the sample gasket induced through compression.

For the approximation of $I^{HP}_{holder}(Q)$ to be accurate, the exact same gasket compression, HP spacing, for the sample must be achieved when compressing vanadium powder. The required pressure to compress vanadium powder to match the gasket deformation is dependent on the bulk modulus of the sample compared to the bulk modulus of vanadium and the initial packing fraction of both. The required vanadium pressure is, in practice, difficult to estimate, and it is assumed that the gasket deformation is the same as the sample measurement when the anvil separation during the vanadium measurement is the same the anvil separation during the sample measurement. Determining the anvil separation for each measurement is required for correctly estimating the background. To

simplify this measurement, it was performed optically by affixing reflective plates to the anvils. The plates were mounted on the anvils in an arbitrary location, but the location was identical for all optical measurements. The optical measurement was performed by analyzing the contrast of a vertical slice of pixels from the optical image of the two anvils. The affixed reflective plate causes a significant spike in pixel brightness and the number of pixels between the spikes was counted. Each pixel was determined to 7 microns in real space.

Data Collection:

Data of the sample were collected at ambient conditions, 50 bar, for 4 hours (~20 C of proton charge). The oil pressure was then increased to 600 bar, approximately 6 GPa, and after the anvil spacing was recorded optically, data of the sample were collected for 12 hours (~60 C of proton charge)[$I_{sample}^{Ambient}(Q), I_{sample}^{HP}(Q)$]. The cell was then depressurized, and the sample removed. An empty TiZr gasket was then mounted in the PE Cell and 50 bar of oil pressure was applied. Data of the TiZr gasket was collected for 2 hours (~10 C of proton charge) [$I_{TiZr\ Gasket}^{Ambient}(Q)$]. The PE cell was then loaded with Vanadium powder in a TiZr gasket under an initial load of 50 Bar and a 2 hour exposure was collected. The cell was then pressurized to 300 Bar, 420 Bar, and 640 Bar with 2 hour measurements at each pressure step to characterize gasket deformation with pressure and to for use in approximating [$I_{holder}^{HP}(Q)$]. The anvil spacing as a function of pressure for the vanadium powder measured optically is shown in Figure 6.1.

Data Processing:

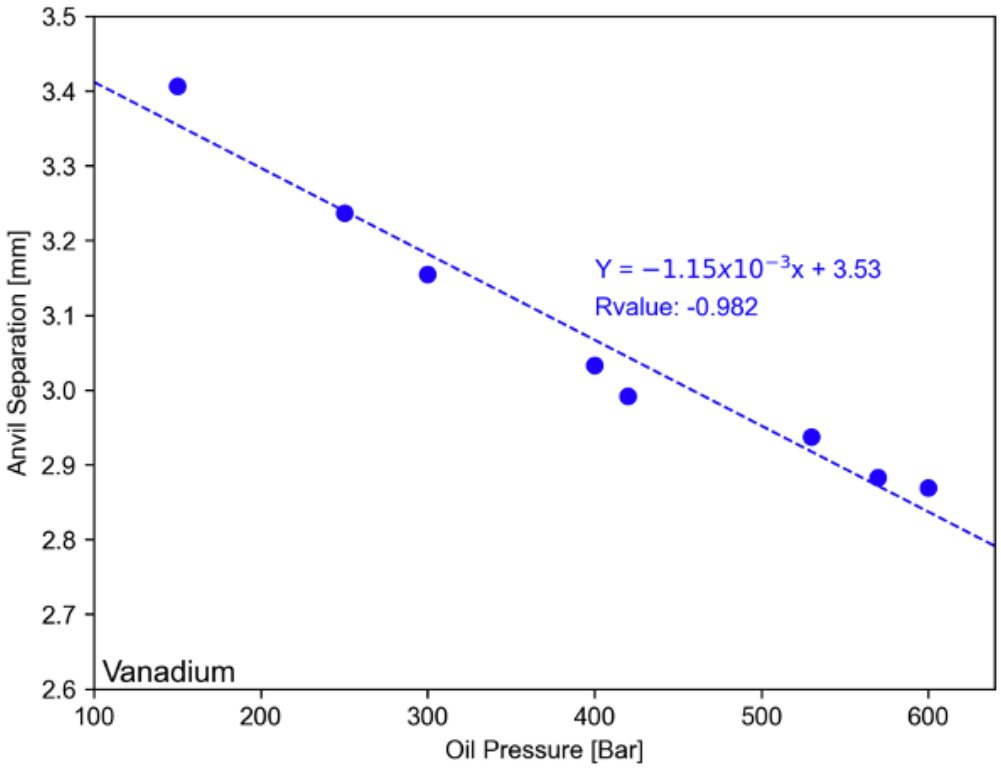

Figure 6.1: Measured single toroidal anvil separation in a Paris Edinburgh Cell as a function of oil pressure for vanadium powder encapsulated in a TiZr Gasket

The contributions of the instrument and sample container must be carefully removed from the collected sample data to create a total scattering pattern with a meaningful Fourier transform. This is especially challenging for samples at high pressure as the compression of the sample in the PE press changes these contributions. The two dominant effects on the background with increasing pressure are (1) reduction in the detector area illuminated by the sample with decreasing anvil separation and (2) increasing radial thickness of the TiZr gasket from plastic deformation. The effect of the changing detector illumination area with decreasing anvil separation is shown in Figure 6.2. At small anvil separations, the amount of detectable sample scattering is significantly decreased, whereas instrument contributions are not affected as severely. This causes a change in the high Q behavior of the data collected at high pressure from the relative increase in instrument contributions. To highlight the issue, two masks were applied to collected vanadium powder data at ambient conditions and at high pressure which removed instrument contributions. The blue curve is the data with a broad mask applied and the green curve is the data with a significant amount of phi space masked out. At ambient conditions, Figure 6.*2a*, the high Q behavior of the data is the same regardless of the mask that is applied. When the anvil separation is small, Figure 6.*2b*, the relative increase in instrument scattering causes a noticeable bump in the diffuse scattering at $Q > 8\ \text{Å}^{-1}$, which can be masked out to recover the ambient high Q behavior. It is important, therefore, to create a mask using the high pressure sample measurement which is then applied to the to the Vanadium powder and empty instrument measurements used to make a total scattering pattern to keep the relative instrument contributions and scaling consistent.

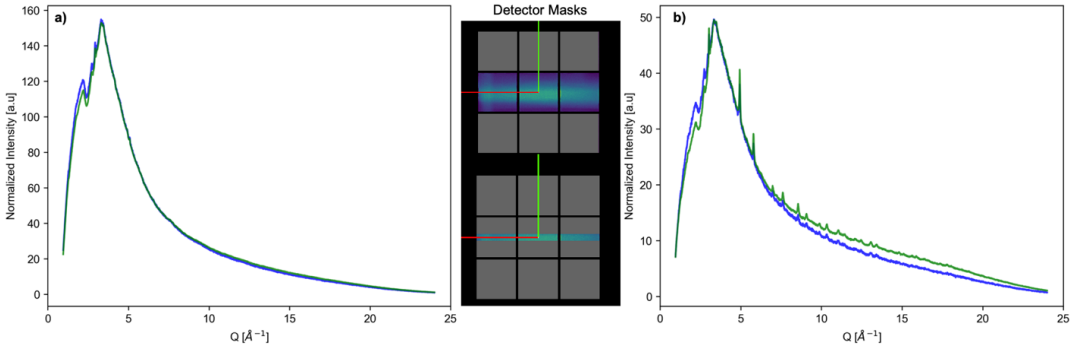

Figure 6.2: Vanadium powder measurements at a) ambient conditions and b) at anvil separation recorded for a sample measured at 8Gpa. The green curve represents the captured spectrum when using the top detector mask. The blue curve represents the results when using the bottom detector mask. The data represented by the blue curve is scaled for comparison.

The other consideration is the additional attenuation of low energy neutrons by the increased radial gasket thickness upon compression. The effect of increasing gasket thickness on the neutron energy spectrum can be characterized by the ratio $\frac{I^{HP\ Spacing}_{Vanadium\ Powder}(Q)}{I^{Ambient}_{Vanadium\ Powder}(Q)}$, this quotient at different amounts of compression (i.e *HP Spacing*) are shown in Figure 6.3. With increasing compression and therefore increasing gasket thickness the number of transmitted neutrons decreases; the trend is similar for all compressions. The magnitude of the decrease in neutron transmission at a given compression is highly dependent on Q which is related to neutron energy. At low Q, the number of transmitted neutrons is greatly decreased and as Q increases the amount of transmitted neutron increases exponentially. This behavior is an artifact of the binning procedure and transformation to Q space and is different when plotted as a function of neutron energy or d-spacing. This variation with Q space at the same anvil separation suggests Q independent scaling of background measurements are inaccurate and will distort the pattern.At a fixed Q or neutron energy, the relationship between transmitted neutrons and compression is linear. The linear behavior between different spacing reaffirms that the plastic deformation of the gasket can also be approximated by a linear interpolation of recovered gaskets from high pressure [147].

The data processing was performed using Mantid Workbench [163]. Data were loaded into mantid, normalized by proton charge (to account for variations in power level of the proton beam on the liquid mercury target), binned, and converted into Q space using SNAPRed. The incoming neutron spectrum as a function of Q spacing was determined using the ambient Vanadium powder measurement.

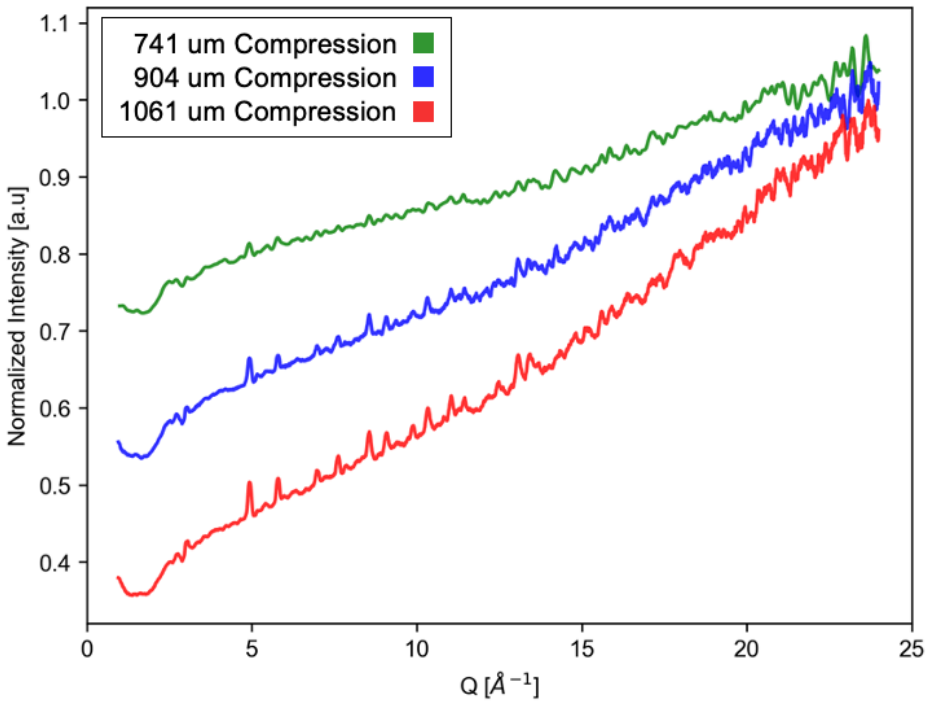

Figure 6.3: Effect of gasket compression on the measured neutron spectrum from Vanadium powder. Anvil spacing was measured from a fixed arbitrary point on the anvil with an initial measured spacing of 3.896 mm.

After the background and gasket enclosure were subtracted from the vanadium powder any vanadium peaks were removed and the noise reduced to create a spectrum for normalizing the collected data, which is referred to later as the "instrument vanadium" measurement or $I_{IS}(Q)$. For ambient measurements in the PE Cell, the sample data and empty gasket measurements were normalized by dividing by the instrument Vanadium, shown in Figure 6.4*a*. The empty gasket, $I^{Ambient}_{TiZr\ Gasket}(Q)$, was then subtracted from the sample measurement, $I^{Ambient}_{sample}(Q)$, to create a total scattering pattern of the sample S(Q), Figure 6.4*b*.

For measurements at high pressure, first a detector mask was produced for the high pressure sample measurement, $I^{HP}_{sample}(Q)$, to minimize the instrument background as shown in Figure 6.2. That mask was then applied to all measurements used to create the high pressure S(Q) [$I^{HP}_{sample}(Q)$, $I^{Ambient}_{TiZr\ Gasket}(Q)$, $I^{Ambient}_{Vanadium\ Powder}(Q)$, $I^{HP\ Spacing}_{Vanadium\ Powder}(Q)$] to maintain a consistent illuminated detector area, which is necessary for a consistent scale factor. The change in the gasket from deformation at pressure was corrected for using vanadium powder measurements. The vanadium powder measured at the same anvil spacing as the high pressure sample measurement was divided by the ambient vanadium powder measurement to create a unitless pressure correction $\frac{I^{HP\ Spacing}_{Vanadium\ Powder}(Q)}{I^{Ambient}_{Vanadium\ Powder}(Q)}$, as shown in Figure 6.5*b*. The correction was then multiplied by the ambient empty gasket measurement to create a background pattern for the high pressure sample measurement [$I^{HP}_{holder}(Q)$], green trace in Figure 6.5*c*. The sample and background patterns were then normalized by dividing by the instrument vanadium, Figure 6.4*c*.

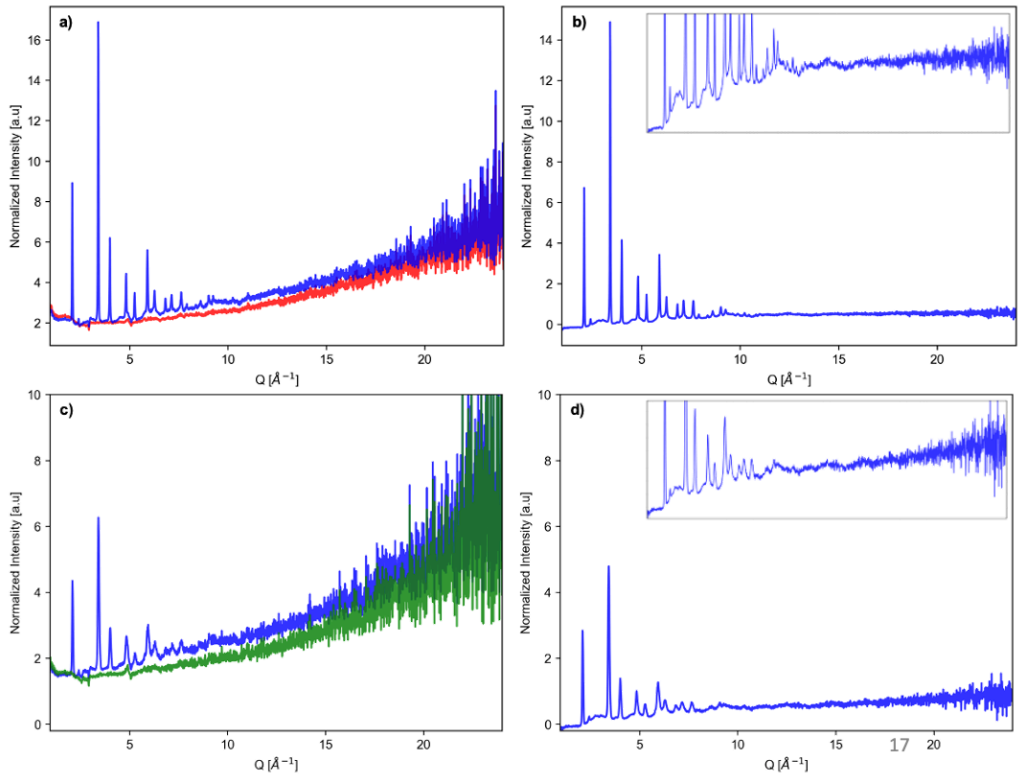

Figure 6.4: Highlight of the data analysis procedure on SNAP. a) Normalized intensity of $Y_2Zr_2O_7$ (blue) and an empty gasket (red) at ambient pressure. b) The resulting pattern of $Y_2Zr_2O_7$ after the empty gasket is subtracted. The insert highlights the diffuse scattering. c) Normalized intensity of $Y_2Zr_2O_7$ (blue) and a corrected empty gasket (green) at 6 GPa. d) The resulting pattern of $Y_2Zr_2O_7$ at 6GPa after the empty gasket is subtracted. The insert highlights the diffuse scattering.

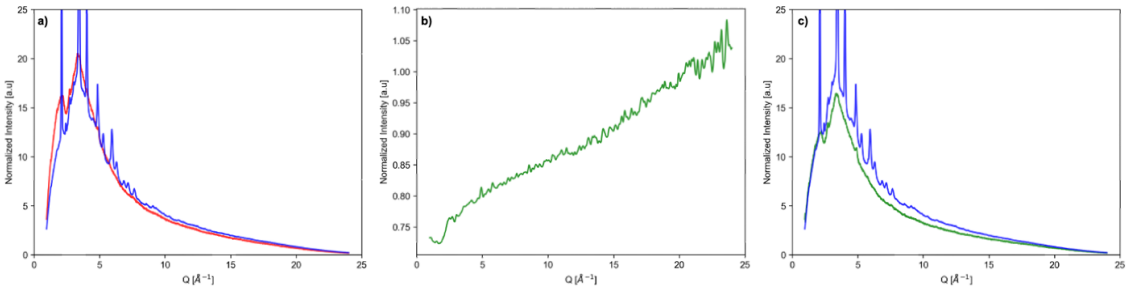

Figure 6.5: Gasket deformation correction at high pressure. (a) blue is the $Y_2Zr_2O_7$ sample collected at 6 Gpa and red is the ambient empty gasket measurement. (b) green is vanadium powder measured at the same spacing divided by ambient vanadium powder. (c) blue is the $Y_2Zr_2O_7$ sample collected at 6 Gpa and green is the empty gasket measurement multiplied by the vanadium quotient shown in (b)

The high pressure background was then subtracted to form a total scattering pattern for the high pressure $Y_2Zr_2O_7$ sample as shown in Figure 6.4*d*.

The processed total scattering patterns were then transformed into pair distribution functions, G(r), using the S(Q) to G(r) program StoG, distributed in RMCProfile [80, 81]. The data were first rebined from Q_{min} = 0.98 to a Q_{max} = 24.0 using bins with width 0.01 $Å^{-1}$. The data were then scaled and Fourier transformed, eq 3, into a pair distribution function.

$$G(r) = \frac{2}{\pi}\int_{Q_{min}}^{Q_{max}} Q[S(Q) - 1]\sin(Qr)dQ \qquad \text{Eq [3]}$$

where Q represents the scattering vector, $4\pi\sin(\theta)/\lambda$, with neutrons of wavelength λ, scattered through angle θ, with the pair distance *r* in real space. The initial integration was performed over a Q range that was dependent on the instrument with, 0.2 to 24 $Å^{-1}$ for the NOMAD measurement, and 0.98 to 24 $Å^{-1}$ for SNAP. A Fourier filter was applied to remove oscillations below 1.8 Å. The scaled and Fourier filtered total scattering patterns are shown in Figure 6.6.

SNAP Characteristics: Ambient Condition Pair Distribution Functions

The potential resolution in real space of PDFs collected at SNAP was tested by repeating the integration represented by equation 2 with different integration limits, as shown in Figure 6.7 for $Y_2Zr_2O_7$ measured in the PE Cell at ambient conditions. The lower integrand of 0.98 $Å^{-1}$ was maintained while the upper limit was increased from 6 to 24 $Å^{-1}$.

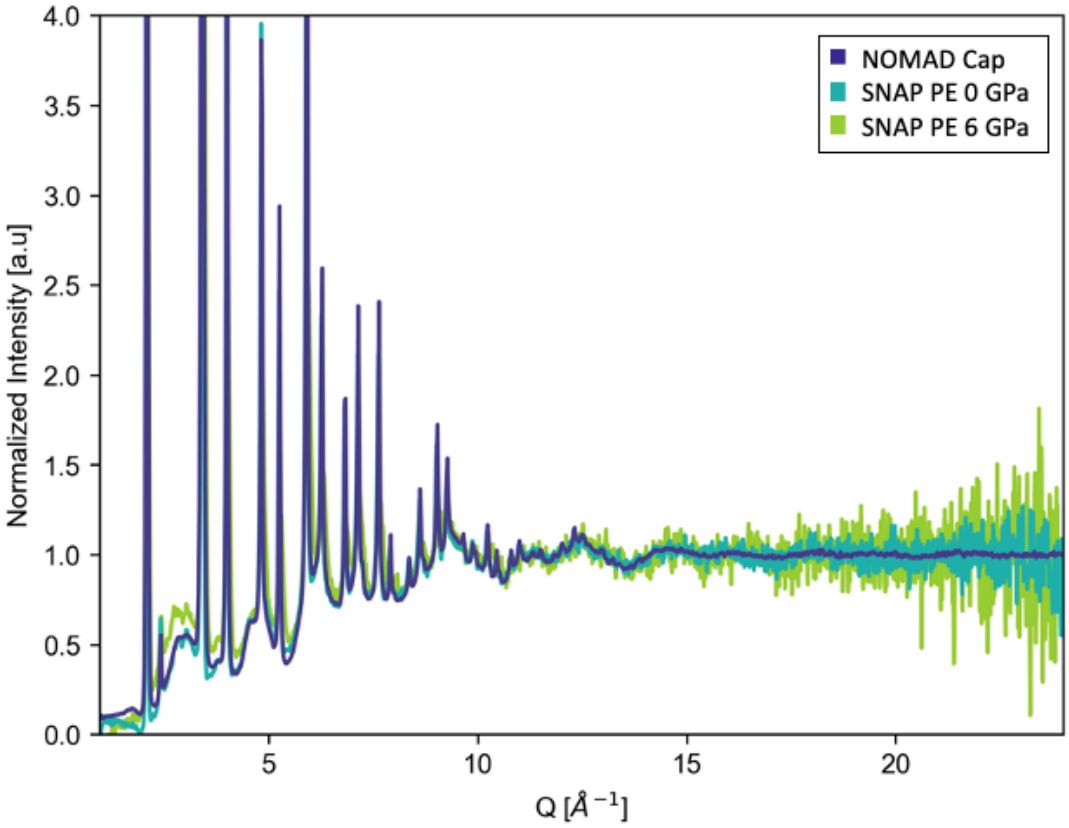

Figure 6.6: Post processing neutron S(Q) for $Y_2Zr_2O_7$ collected in a capillary at NOMAD and in a PE Press at ambient conditions and at 6 GPa. Data has been scaled and Fourier filtered.

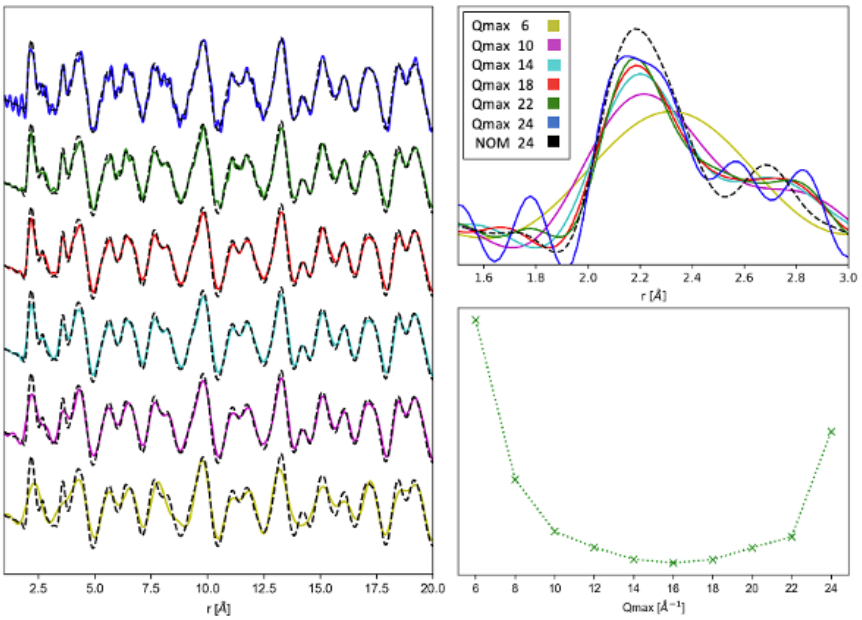

Figure 6.7: Integrated PDFs for $Y_2Zr_2O_7$ measured in a PE Cell at ambient conditions. The right panel shows the integrated SNAP patterns with different upper integration limits (Q_{max}) in color with the integration performed on NOMAD data in dashed black lines. The upper left panel is the same data plotted with no offset and the first peak highlighted. The lower left panel is the summed absolute difference between each SNAP PDF and the NOMAD PDF reference.

Increasing the maximum Q value of the limit used in the integration will increase the resolution of the calculated PDF, however, the counting statistics at higher Q are significantly lower, which can introduce noise into the PDF.

These effects were quantified by comparing PDFs integrated at different limits to a PDF create with data collected in a capillary at NOMAD integrated to the max integrand possible at SNAP of 0.98 to 24 $Å^{-1}$. The NOMAD PDF is assumed to be an accurate representation of an experimental PDF of $Y_2Zr_2O_7$. The summed absolute difference between the NOMAD and SNAP integrations with increasing Q_{max} integrands from 0 to 50 Å in real space is shown by the green curve in Figure 6.7. As Q_{max} increases the difference decreases as peaks become less broad with increasing resolution. The potential improvement in PDF quality is outweighed by the additional noise introduced into the pattern at high Q starting at a Q_{max} of 18 $Å^{-1}$ where the difference between the SNAP and NOMAD patterns begins to increase. The difference continues to increase as Q_{max} increases past 18 $Å^{-1}$.

The intensity of noise in the transformed PDF is also dependent on measurement time. Time filtering, which creates a pattern that consists only of detector events that occur before a certain time, was applied to the collected sample data to show the effect of measurement time on the final integrated PDF, shown in Figure 6.8. The vanadium powder measurements used for post processing and normalization of the data were not time filtered. The ratio of the measurement time of the sample with respected to the empty gasket is depended on the ratio of the respective measured intensities [164].

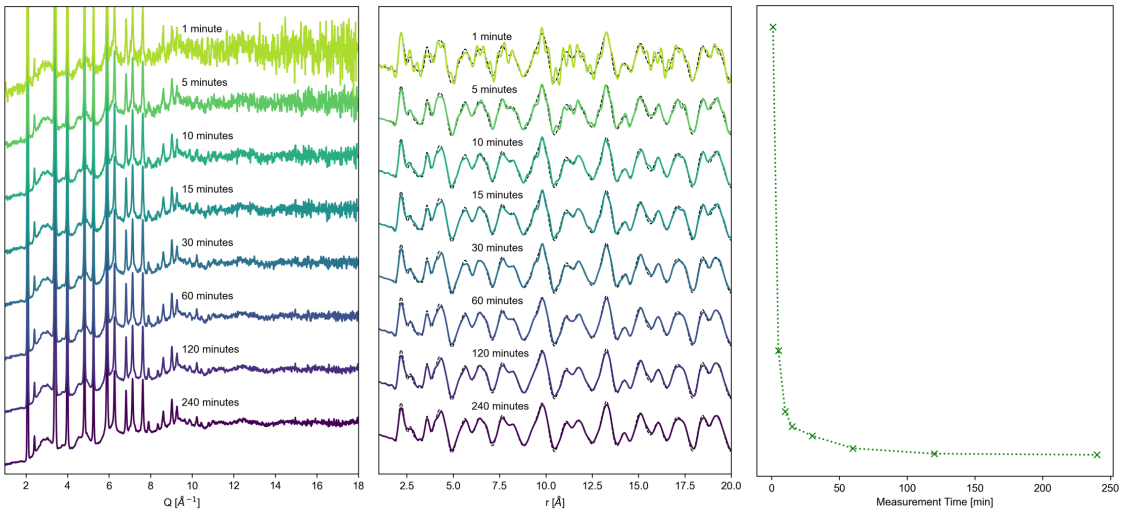

Figure 6.8: Neutron total scattering patterns (left) and transformed pair distribution functions (middle) for $Y_2Zr_2O_7$ loaded in a PE Cell at ambient conditions collected for varying measurement times, which are denoted above each pattern. The summed absolute difference between each pair distribution function collected at SNAP and a NOMAD reference are represented by the green curve on the right plot.

For $Y_2Zr_2O_7$ the optimal ratio of the counting times is approximated one, therefore, the time filter was applied equally to the sample measurement and the empty gasket measurement. The collected data were processed to form a total scattering pattern, shown in the left plot of Figure 6.8. These total scattering patterns were transformed in StoG provided in RMCProfile using a Q_{max} of 18 $Å^{-1}$, which were compared to an experimental PDF from NOMAD with the difference represented by the green summed difference curve in the right plot of Figure 6.8. The difference between the generated PDFs from SNAP and the NOMAD reference decreases sharply with increasing measurement time. The collected patterns from SNAP continue to improve with increasing measurement time. These improvements, however, are less noticeable for measurements longer than 60 minutes (5 C of charge).

SNAP Characteristics: High Pressure Pair Distribution Functions

The potential PDFs generated from data collected at SNAP are also affected by applying pressure, which changes the instrument geometry, as well as, the gasket radial thickness through plastic deformation. The resolution in real space at pressure was investigated in a similar manner to ambient conditions by varying the upper integrand of the Fourier transform described in equation 2 as shown in Figure 6.9. Applying pressure increased the noise present in the collected data and the noise is more pronounced at lower Q when compared to the data collected at ambient conditions.

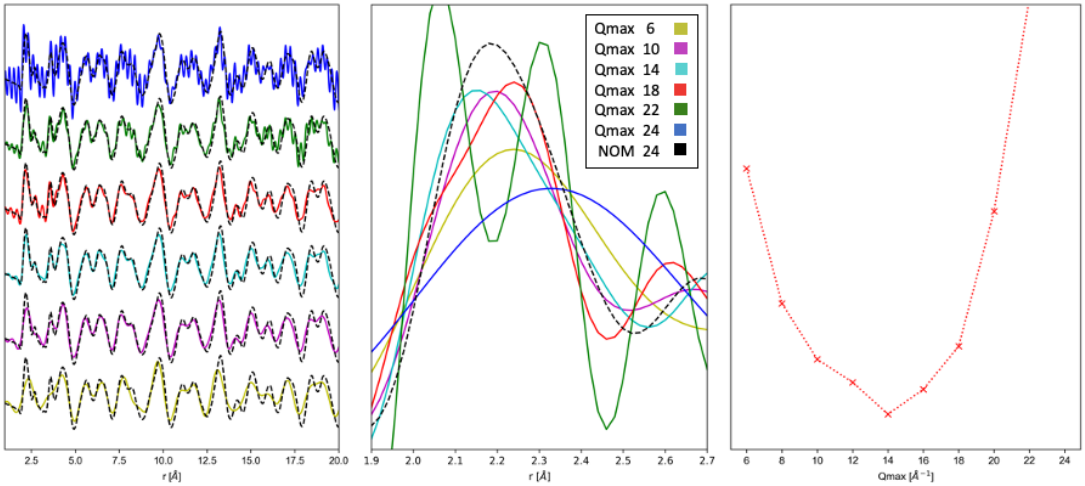

Figure 6.9: Integrated PDFs for $Y_2Zr_2O_7$ measured in a PE Cell at6 GPa. The right panel shows the integrated SNAP patterns with different upper integration limits (Q_{max}) in color with the integration performed on NOMAD data in dashed black lines. The middle panel is the same data plotted with no offset and the first peak highlighted. The right panel is the summed absolute difference between each SNAP PDF and the NOMAD PDF reference.

The summed absolute difference between the high pressure PDFs on SNAP, integrated with different upper integrands (Q_{max}), and the NOMAD reference are shown by the red line in the right panel of Figure 6.9. The difference decreases with increasing Q_{max} and the lowest difference is when the SNAP PDFs are integrated with a Q_{max} of 14 $Å^{-1}$, which is a reduction in resolution in real space when compared to the measurements in a PE Cell at ambient conditions. As Q_{max} increases past 14 $Å^{-1}$, the noise in the generated PDFs on SNAP increases causing a sharp increase in the difference from the NOMAD reference PDF, staring at 16 $Å^{-1}$. The left panel of Figure 6.9 suggests that a significant portion of the increased difference seen in the right panel is at greater distances in r space as the generated PDFs with a Q_{max} of 14 $Å^{-1}$(cyan) and 18 $Å^{-1}$ (red) do not show a dramatic increase in noise.

The effect of applying load on the sample on the required measurement time for generating quality PDFs was also investigated using a similar process to the measurements at ambient conditions, Figure 6.10. The time filtering was kept the same for the sample measurement time and empty gasket measurement time and the full vanadium measurement was used for post processing. The collected data were Fourier transformed in StoG using an upper integrand (Qmax) of 16 $Å^{-1}$ to minimize noise while focusing on increasing PDF resolution in real space. The transformed PDFs were compared to a PDF generated from data collected at nomad at ambient conditions. The summed absolute difference is shown in the red curve in the right panel of Figure 6.10. There is a dramatic increase in the similarity between the collected PDFs on SNAP to the NOMAD reference with increasing counting time.

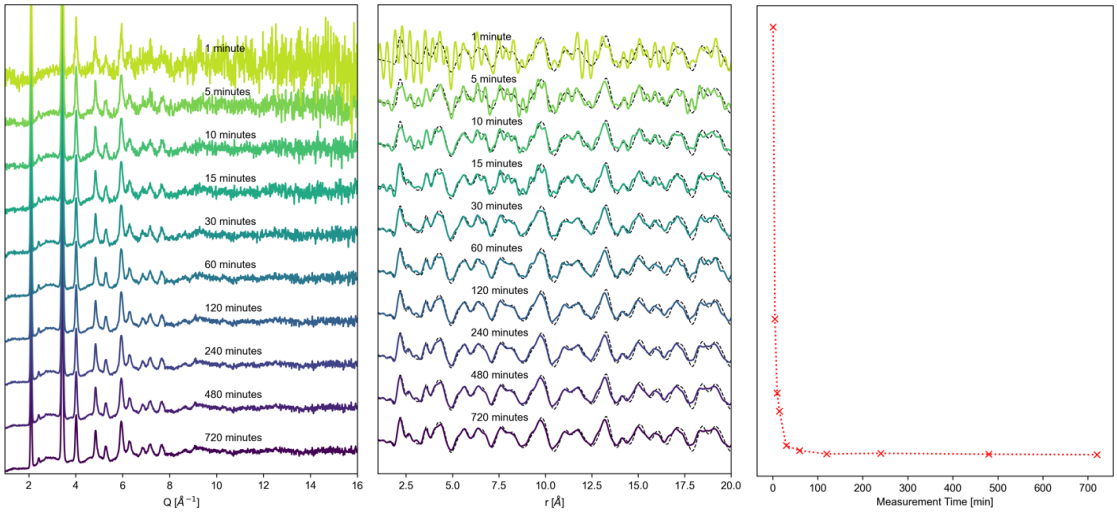

Figure 6.10: Neutron total scattering patterns (left) and transformed pair distribution functions (middle) for $Y_2Zr_2O_7$ loaded in a PE Cell at 6 GPa collected for varying measurement times for the sample and empty gasket, which are denoted above each pattern. The summed absolute difference between each pair distribution function collected at SNAP and a NOMAD reference are represented by the red curve on the right plot.

The improvement with increasing counting time is less significant after 60 minutes of counting and addition sample measurement time after the max empty gasket measurement of 120 minutes provides no additional reduction in noise.

In both the high pressure Q range analysis and measurement time investigation at high pressure the absolute summed differences between the SNAP and NOMAD capillaries are significantly higher at 6 GPa than at ambient conditions. Although no significant structural changes are expected at this pressure, the high shear stress created by pressurizing with no pressure medium will cause strain broadening[165] that increases the difference from the ambient NOMAD data especially at greater distances in real space, r. To account for these changes, both the neutron diffraction patterns, and generated PDFs were also fit with a simulated structure using small box modeling to verify the structure at pressure, shown in Figure 6.11.

Discussion

Using the SNAP beamline, the structural heterogeneity of $Y_2Zr_2O_7$ was successfully measured at ambient conditions in a PE Cell. This capability was also preserved at high pressure (~6 GPa) with some degradation in PDF quality. The quality of the generated $Y_2Zr_2O_7$ PDFs on SNAP, however, is highly depended on measurement time and the usable Q range for the Fourier transformation. The lowest noise in the transformed PDFs was achieved using a Q range of 0.98 to 16 $Å^{-1}$ at ambient conditions and 0.98 to 14 $Å^{-1}$ at high pressure. Increasing the Q_{max} used in the integration will improve resolution in real space but will increase the likelihood that noise is introduced into the transformed pattern.

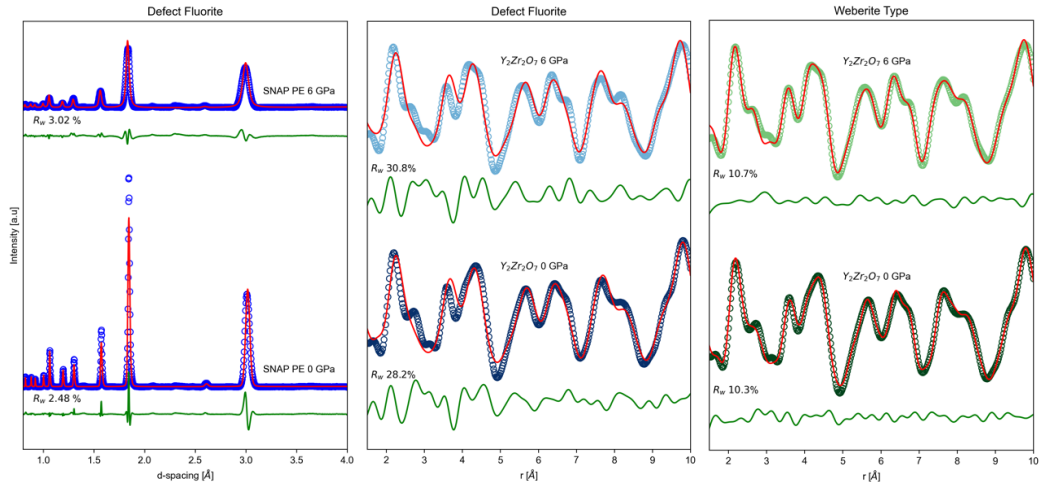

Figure 6.11: Refinement results for defect fluorite and Weberite type structures on collected SNAP data in a PE press and Ambient (lower plot) and high pressure (top plot). The left panel is the long-range Bragg diffraction data, represented by blue circles, fit with a defect fluorite structure, in red. The middle panel is the local PDF data, represented by blue circles, fit with a defect fluorite structure, in red. The right panel in the local PDF data, represented by green circles, fit with a Weberite type structure, in red. The difference between the observed and calculated patterns is shown below in green. The ambient and high pressure data shown were acquired for 60 minutes and used integration limits of 0.98 to 18 $Å^{-1}$ and 0.98 to 14 $Å^{-1}$

These values for the integration will be dependent on the scattering strength of the loaded sample as stronger scatters will have a better sample to noise ratio at higher Q values. For $Y_2Zr_2O_7$, the coherent scattering cross section of the individual constituents (Y:7.55b, Zr:6.44b, O:4.232b) and density of 5.65 $\frac{g}{cm^3}$ results in an above average reaction rate for scattering among complex oxides; therefore, for experiments on similar materials at SNAP a Q_{max} of around 14 to 18 $Å^{-1}$ is expected to produce the cleanest PDF with a real space resolution of $\Delta r = \frac{\pi}{Q_{max}} = 0.17\ to\ 0.22$ Å. The required measurement time is depended on sample composition and sample container [164].

In an encapsulated TiZr gasket mounted on single toroidal anvils, a measurement time of one hour for the empty container and one hour for the $Y_2Zr_2O_7$ sample was sufficient to produce refinable PDFs, Figure 6.11. Increasing the measurement time, produced diminished improvement to the pattern past this point, Figures 6.8 and 6.10. The increased neutron flux at the Spallation Neutron Source has significantly shortened the length of high pressure total scattering experiments compared to similar experiments performed using reactor sources. With a strong scattering sample, a complete set of measurement including the empty container and vanadium can be acquired within a few hours as opposed to the roughly 24 hours that was previously required for each individual measurement [149]. The dramatic improvement in measurement time from the increased neutron flux does not appear have as much of an influence on the high Q data as would be expected, especially with the increased neutron flux at high energies from a spallation source. The usable Q_{max} of the data collected at SNAP, 14 to 18 $Å^{-1}$, is comparable to other

high pressure total scattering experiments at PEARL ($Q_{max} \cong 19.6$ Å^{-1} [146]) and D4C ($Q_{max} \cong 15.45$ Å^{-1} [147]).

The noise at high Q in the reduced data is particularly sensitive to the background subtraction method as the scattering strength of the sample decreases with Q making it less pronounced from the instrument background. It is therefore crucial that the same instrument geometry and gasket deformation is achieved, *HP Spacing* , for the encapsulated vanadium powder background measurement $I_{Vanadium\ Powder}^{HP\ Spacing}(Q$ used to calculate $\frac{I_{Vanadium\ Powder}^{HP\ Spacing}(Q)}{I_{Vanadium\ Powder}^{Ambient}(Q)}$. In this experiment, measuring this separation optically was insufficient to consistently reproduce the gasket deformation accurately. In practice, gaskets will deform differently even at the same anvil separation depending on how much of the internal volume of the gasket is filled by a sample or vanadium powder when loading. The difficulty in completely filling the internal volume for powder samples is dependent on the pellet pressing process, which creates a dense powder compact that is the same shape and volume as the sample chamber in the gasket. Whether a pellet pressing is successful is highly dependent on the grain size, hardness, and texture of the starting sample powder. It is, therefore, often more accurate to select a vanadium powder background measurement based on the deformation of the sample gasket, which can be deconvolved from a comparison of the ambient and high pressure measurement.

The changes to the diffuse scattering intensity from gasket deformation in the high pressure sample measurement were highlighted by analyzing the ratio $\frac{I_{Sample}^{HP}(Q)}{I_{Sample}^{Ambient}(Q)}$ (the high pressure sample pattern divided by the ambient sample pattern), which was then compared

to $\frac{I^{HP\ Spacing}_{Vanadium\ Powder}(Q)}{I^{Ambient}_{Vanadium\ Powder}(Q)}$ previously shown in Figure 6.3. The divided sample data $\frac{I^{HP}_{Sample}(Q)}{I^{Ambient}_{Sample}(Q)}$ shows the same behavior as gasket correction $\frac{I^{HP\ Spacing}_{Vanadium\ Powder}(Q)}{I^{Ambient}_{Vanadium\ Powder}(Q)}$, Figure 6.12, which is a result of the increased radial thickness of the gasket from plastic deformation during compression in both loadings. Along with these features, changes to the sample with increasing pressure are present in the sample quotients, $\frac{I^{HP}_{Sample}(Q)}{I^{Ambient}_{Sample}(Q)}$. The main contributions are (1) Bragg peak shifting, which causes the sharp spikes in the sample data at low Q (2) sample diffuse scattering changes, which cause short oscillations in Q and (3) sample density and packing fraction changes, which cause Q independent changes. These changes are distinct from the changes caused by gasket deformation, which while Q dependent, evolve significantly slower than sample variations.

Determining the ideal vanadium powder background measurement for a high pressure sample, therefore, should be done in a similar manner to the previously reported methodology on PEARL [146]. On PEARL, a similar pulsed TOF neutron high pressure instrument, the instrument geometry was not directly measured. Instead after sample measurements were performed, the matching encapsulated vanadium measurement was selected by testing how it affected data reduction. In practice, this required initially underestimating the pressure on the background vanadium taking a small measurement and performing the data reduction. If the produced pattern was not invariant with Q at high Q ~15-20 $Å^{-1}$ (i.e flat), the pressure was slightly increased, and a new short vanadium measurement was taken. Once the produced pattern satisfied the desired high Q behavior a long vanadium measurement was taken at that pressure to improve statistics.

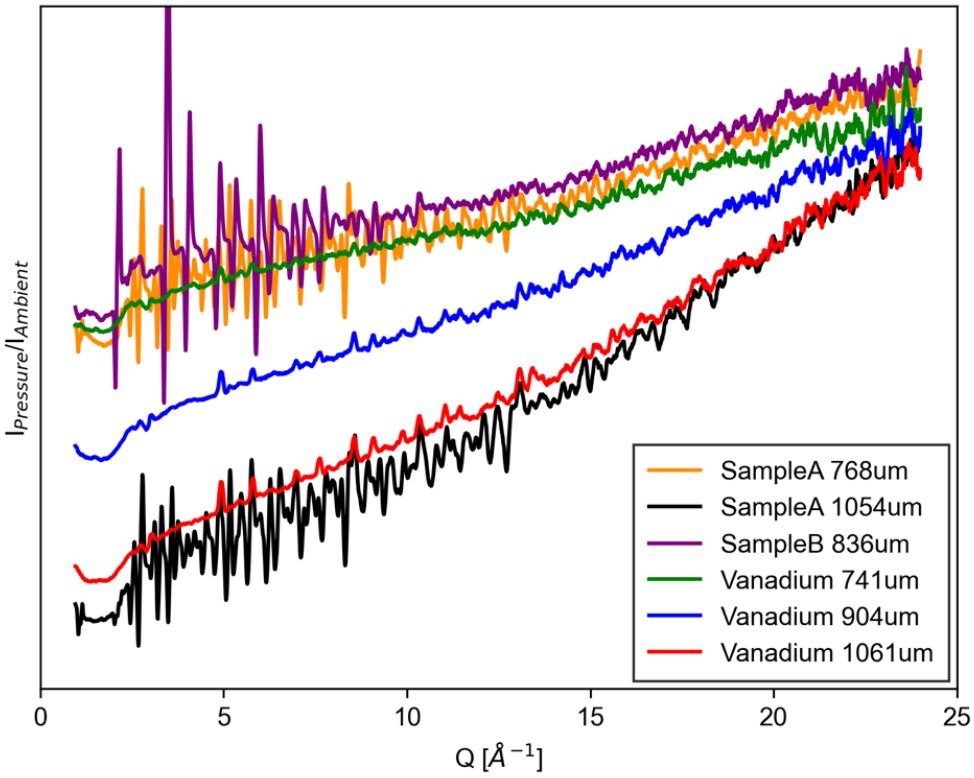

Figure 6.12: Examples of quotients of high pressure data over its respective ambient measurement. The green, blue, and red curves are the vanadium powder measurements from figure 3. The orange and black curves are sample A ($Y_2Ti_2O_7$), which was measured during the same beamtime as the purple curve (Sample B $Y_2Zr_2O_7$). Plotted data has been denoised to improve clarity.

This method can account for the variation in gasket deformation with different loadings; however, as shown in Figure 6.12 the high Q behavior is relatively insensitive to gasket changes compared to the changes to the intensity at low Q. Determining the vanadium pressure using high Q, is necessary on PEARL as the low Q range cannot be measured using a transverse instrument geometry. On SNAP, the same vanadium pressurization scheme should be followed, but instead of analyzing the high Q behavior of the produced pattern, the ratio of the high pressure vanadium measurement to the ambient vanadium measurement, $\frac{I^{HP\ Spacing}_{Vanadium\ Powder}(Q)}{I^{Ambient}_{Vanadium\ Powder}(Q)}$, should be used, Eq 4. When this ratio matches the ratio for the high pressure sample measurement over its ambient measurement at low and high Q, $\frac{I^{HP}_{Sample}(Q)}{I^{Ambient}_{Sample}(Q)}$, the gaskets must be deformed the same amount, and a long background measurement can be collected.

$$\frac{I^{HP}_{Sample}(Q)}{I^{Ambient}_{Sample}(Q)} \cong \frac{I^{HP\ Spacing}_{Vanadium\ Powder}(Q)}{I^{Ambient}_{Vanadium\ Powder}(Q)} \qquad \text{Eq[4]}$$

With the background properly subtracted, the integratable Q range of a measurement is only limited by the sample signal at high Q. To understand the potential limits of a measurement on SNAP, an ambient measurement of $Y_2Zr_2O_7$ was also performed in a 3mm diameter quartz capillary using the same 750 micron slit collimator. This setup removes the limit scattering angles and extra background signal of the PE Cell while maintaining a similarly reduced illuminated sample volume. Interestingly, measuring the sample outside the PE cell did not dramatically decrease the noise in the collected data, as shown in Figure 6.13*a*.

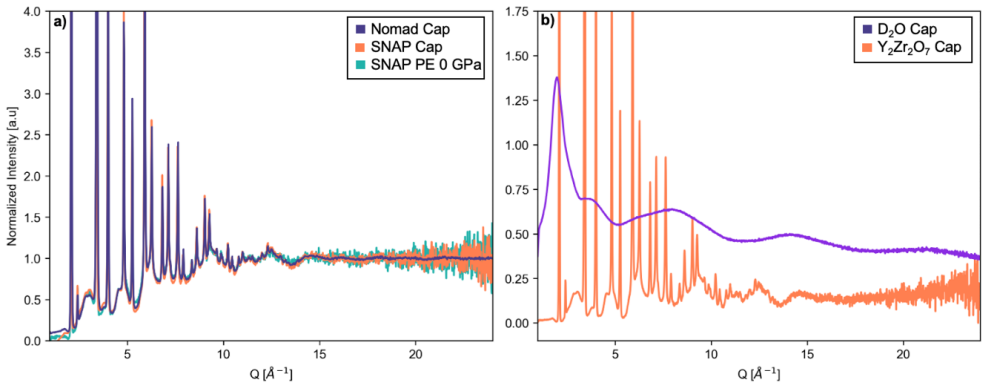

Figure 6.13: **a)** Back transformed neutron S(Q) for $Y_2Zr_2O_7$ collected in a capillary at NOMAD, in a capillary at SNAP, and in a PE Press at ambient conditions. Data has been scaled and Fourier filtered. **b)** Uncorrected neutron total scattering patterns of (orange) $Y_2Zr_2O_7$ powder acquired for 2 hours in a 3mm quartz capillary using a 750 micron slit collimator and (purple) D_2O liquid acquired for 2 hours in a 2mm thin walled quartz capillary using a 3mm circular collimator.

This suggests that the limiting factor in data quality is the sample signal itself and not the PE Cell and instrument setup. The samples signal is low due to the small sample volume and is not an inherent limitation of the SNAP instrument, which can be seen comparing to other samples measured without these volume limitations. A measurement of D_2O in a 2mm thin walled capillary using a larger 3mm circular collimator with the same detector positions is shown in purple in Figure 6.13*b*. The D_2O sample has significantly less noise at high Q due to the samples increased atomic number density and larger illuminated volume. This was confirmed by time filtering the D_2O sample to have roughly the same number of coherent neutron scattering events as the $Y_2Zr_2O_7$ and the resulting pattern had a similar amount of noise.

Characterization of $Y_2Zr_2O_7$ Defect Fluorite

Sample Synthesis

The $Y_2Zr_2O_7$ powder was synthesized through the solid state reaction shown in equation 5. The reactants, Y_2O_3 and ZrO_2, were purchased from Alfa Aesar with cation purities of 99.99% and 99.7% respectively.

$$Y_2O_3 + 2\ ZrO_2 \rightarrow Y_2Zr_2O_7 \qquad \text{Eq [5]}$$

The starting powders were calcined at 800 °C for 8 hours. The powders were then mixed in a mortar and pestle and then milled under ethanol with WC tools using a RETCH PM200 planetary ball mill at 300 rpm for 6 hours with 1 minute breaks after every 15 minutes to prevent sample heating. After milling the powders were calcined again as above and pressed into ½" pellets under uniaxial load at 2 tonns. The pellets were initially sintered at

1200 °C for 48 hours than ground, milled, calcined and pressed in the same manner as before again. These new pellets were then sintered at 1100 °C for 10 hours, then ramped to 1600 °C for 72 hours, and finally down to 1300 °C for 48 hours. The pellets were then reground, and the reaction verified through laboratory XRD and Raman spectroscopy. The powder was prepared for loading into the PE cell by forming a dense pellet through pressing 220 mg of powder in a custom die that matches the sample chamber of an encapsulated gasket.

Data Analysis

Rietveld refinement was performed on the collected neutron diffraction patterns using the GSASII[87] software package. The long-range data was modeled using an isometric disordered fluorite structure, Table 6.1, with 5 parameters: the scale factor, unit cell parameter (a=b=c), and one atomic displacement parameter for each crystallographic site ($U_{11}=U_{22}=U_{33}$). In the disordered structure A and B cations shared the available sites, so a single ADP was used for both the A and B cations and a second was used for the Oxygen anion. The short-range structure of the samples were analyzed using small box modelling in PDFgui[88]. The pair distribution functions were modeled using both a defect fluorite and a Weberite type structure, Table 6.1. The Weberite type model requires 28 total parameters: scale factor, 3 unit cell parameters ($a \neq b \neq c$), 8 structural position parameters, and 15 atomic displacement parameters.

Table 6.1: Atomic positions of $Y_2Zr_2O_7$ in the defect fluorite and Weberite Type structures, bold positional coordinates are free parameters that are fit during refinement.

Wyckoff Equipoint (CN)	Site Occupant	x	y	z
Defect Fluorite $Fm\bar{3}m$ (# 225)				
4*a* (7)	$Y_{0.5}$ $Zr_{0.5}$	0	0	0
8*c*	$O_{0.875}$	0.25	0.25	0.25
Weberite-Type $C222_1$ (# 20)				
4*b* (8)	Y	0	**0.4908**	0.25
8*c* (7)	$Y_{0.5}$ $Zr_{0.5}$	**0.2338**	**0.2421**	**0.4933**
4*b* (6)	Zr	0	**-0.0081**	0.25
8*c*	O	**0.1380**	**0.2062**	**0.7591**
8*c*	O	**0.6231**	**0.2687**	**0.7778**
4*a*	O	**0.3816**	0	0
4*a*	O	**0.6616**	0	0
4*a*	O	**-0.0799**	0	0

Results

The collected neutron diffraction patterns and transformed pair distribution functions for $Y_2Zr_2O_7$ are shown in Figure 6.11. The long range diffraction data shown in the left panel of Figure 6.11 shows a slight peak shift with increasing pressure to a lower d-spacing as the cell volume reduces. The peak intensity reduces drastically at high pressure and the peaks become broader. The broadening is especially significant at low d-spacing, where some peaks become broad enough to no longer be distinguishable from the background. The peak broadening and shifting is expected for samples under pressure with no pressure medium [166]. The effect of pressure on the pair distribution function are more subtle, as shown in the left two panels of Figure 6.11. The peaks in the PDF broaden under increasing pressure from increased strain [165]. The most apparent differences with pressure are changes to the shape of the broad peaks between 4-5 Å where the most intense point of the peak shifts to lower r and the broad peaks between 6-7 Å and 7-9 Å where the peak shoulders become more distinct with pressure.

The effect of increasing pressure and changing sample environment on the refined long range structure parameters was determined through Rietveld refinement in the GSASII software package [87]. The refinements of the diffraction patterns collected at SNAP are accurately modeled using a defect fluorite model, red curves in the left panel of Figure 6.11. The most distinct differences between the calculated diffraction pattern and the observed pattern are in the peak intensity and shape at 3 angstrom and 1.8 angstrom. The model underestimates the broadness of the peaks and intensity. The collected peaks themselves are also asymmetric, which is common for moderated pulsed neutron sources

[167]. The weighted agreement factor, R_w, for each of the refinements on SNAP are very low, suggesting excellent agreement between the model and the observed data.

The generated neutron PDFs from the SNAP data were fit using small box modeling using the PDFGUI software package[88]. The defect fluorite model used to fit the long range diffraction patterns is a poor representation of the local structure, as shown in the middle panel of Figure 6.11. The long range model is unable to reproduce the shoulder on the peak at 2.1 Å and does not capture the relative intensities and positions of the peaks at 3.8 and 4.5 Å. At higher r the defect fluorite model reproduces the data more accurately. These deviations at low r are captured by the Weberite type model shown in the right panel of Figure 6.11. The data at high pressure is also accurately modeled using this structure, despite the previously noted difference to the ambient PDF, with a reasonably low weighted agreement factor.

Behavior of Weberite during Compression

Although confined to a resolution of $0.17\ to\ 0.22$ Å in real space, the local structure of defect fluorite was refinable in both the ambient and high pressure measurements using small box modelling, as shown in Figure 6.11. The local Weberite-type phase in defect fluorite has been extensively reported; however, this is the first study of the changes to a local structure under pressure. Upon compression, the unit cell of local orthorhombic Weberite-Type phase compress by different amounts, with the largest reduction in size in the b-axis ($\frac{\Delta C}{C_0}$ = -0.41%, $\frac{\Delta a}{a_0}$ = -0.67%, $\frac{\Delta b}{b_0}$ = -1.16%). This is in contrast with the long range cubic structure which compresses isotopically. The local structure fit the high pressure data

with no significant distortions to the polyhedra. At 6 GPa, $Y_2Zr_2O_7$, is significantly below the transition pressure to a its high pressure orthorhombic phase (27.3 GPa), so no significant changes are expected compared to ambient conditions[168].

Conclusions

The SNAP beamline at the Spallation Neutron Source at Oak Ridge National Laboratory is an ideal beamline for total scattering at high pressure. In experiments on $Y_2Zr_2O_7$ pressurized to 6 GPa using single toroidal anvils in a PE Cell, the long range and distinct short range structures were able to be characterized through Rietveld refinement and small box modelling. The increased neutron flux from the SNS compared to other high pressure beamlines greatly reduced the required measurement time to approximately 60 minutes; however, the usable Q-range for Fourier transform remains similar to other high pressure neutron diffraction instruments. Depending on the scattering strength of the sample, an integratable Q range of 0.98 to 14 - 18 $Å^{-1}$ is expected for compositions of a similar density and scattering length as $Y_2Zr_2O_7$ (5.65 $\frac{g}{cm^3}$ Y:7.55b, Zr:6.44b, O:4.232b).

The experimental methodology for performing these measurements on SNAP is similar to other neutron TOF spectrometers. The two SNAP detector banks should be set to 50° and 105° and the chopper to 1.8 Å. The most significant complication when performing total scattering at pressure is accurately capturing the instrument and sample holder contributions for subtraction at pressure. This was accomplished by crushing vanadium powder in an encapsulated gasket to the same amount of deformation as the sample. Determining the amount of deformation by comparing the change in the intensity of the diffuse scattering upon compression across Q in both the sample and vanadium

powder is the best way to reproduce the sample background conditions. The required pressure for the vanadium powder background measurement cannot easily be predicted as it is dependent on the physical properties of the sample and the quality of the sample loading; therefore, it is best to first underestimate the required vanadium pressure and slowly increase it taking measurements and comparing with the sample measurement. This procedure may be more difficult to follow for samples that must be loaded at pressure as is the case for gas loadings as the initial sample gasket deformation from the sample loading will not be possible to measure.

There is potential to simplify this experimental procedure further through using different methods to estimate the background instead of using a direct measurement. These methods may include approximating the empty gasket using interpolation of less exact vanadium powder gasket measurements using a linear combination of other vanadium powder gasket measurements or through deconvolving the signal from the sample itself. Further work is also required to improve the signal to noise ratio at higher Q ranges, this may be achieved through denoising post measurement or adjusting the instrument setup to illuminate more sample powder. For example, using a larger collimator and switching to neutron transparent anvils would boost the signal significantly but will result in a more complicated background subtraction. In its current form, however, total scattering *in situ* at pressure is attainable on SNAP and the data is sufficient quality to aid in many future scientific discoveries.

Chapter 7

Conclusions, and

Future Perspectives

The results presented in this dissertation on the local structure of spinel oxides disordered through extreme conditions are a continuation of extensive debate on the structure of both pristine and disordered spinel. Despite being the first solved complex oxides structure in 1915, the structure of Spinel ($MgAl_2O_4$) has been seriously debated on numerous occasions. All the major debates on the structure of $MgAl_2O_4$ have the same root cause, inability to accurately measure the structure through conventional diffraction techniques. The ideal technique to determine the structure of spinel is one that can easily distinguish between Mg, Al, and O and can measure both the long range diffraction and local atomic arrangements simultaneously. In the previous 30 years, significant developments in total scattering experiments and the development of high flux spallation neutron sources have created a viable measurement technique that can completely describe the disordered spinel structure, neutron total scattering[169]. Using neutron total scattering, the structure of $MgAl_2O_4$ can be accurately determined across lengths scales and with increasing disorder. This modern advanced characterization technique encourages the reexamination of previous noted structural discrepancies in the spinel structure and enables the accurate determination of the spinel structure disordered through extreme conditions.

Neutron total scattering analysis on the spinel structure was first reported by Shamblin *et al.* in 2016[140] and expanded upon by O'quinn *et. al*. in 2017[107]. Using this advanced technique, they determined that increasing inversion, determined by measuring the average structure, resulted in a growing local phase fraction of a tetragonal phase. This local cation ordering and resulting lower symmetry structure in partially inverted spinel may potentially explain previously noted discrepancies in physical property measurements,

calorimetry, and Raman spectroscopy. The formation of the tetragonal phase is a consequence of approximately balancing local charge in a disordered system, which is easily quantified using Pauling's second rule[74]. It is, therefore, likely that the same tetragonal structure would be present in all disordered spinel structures as it is a fundamental consequence of cation anti-site defects in the structure.

The work presented in this thesis is a continuation of this work on applying neutron total scattering techniques to the spinel structure. In chapter 4, the change in inversion with increasing temperature and local atomic structure was investigated for $MgAl_2O_4$ and $NiAl_2O_4$. This study found that for extrinsic disordering mechanisms, like temperature, increasing inversion is directly linked to an increase in local tetragonal phase. The finding by O'quinn *et. al* is therefore independent of potential intrinsic chemical effects that may arise from doping with Ni. The presences of a local cation ordering in thermally disordered spinel explains discrepancies noted in calorimetry on $MgAl_2O_4$. The study, however, was limited in temperature to 1000 °C which is low when compared to the geologic temperatures of interest for spinel. There is potential for future work at higher temperatures when furnace capabilities are expanded at spallation neutron sources.

Although the tetragonal local structure has been consistent in mild intrinsic and extrinsic disordering, the local structure of spinel exposed to highly energetic transient environments was still not understood. In chapter 5, the spinel chemical solution series ($Mg_{(1-x)}Ni_xAl_2O_4$) was exposed to swift heavy ion irradiation to induce an extreme transient state. Using 2.2 GeV ions, enough samples mass (~100 mg) was produced to perform neutron total scattering. The quenched structure after exposure was highly inverted for all

chemical compositions and the increase in inversion was coupled to an increase in local tetragonal phase fraction. The quenched inverted structure, however, had additional defects not seen in previous milder disordering methods. These defects were additional octahedral disordered with cation Frenkels forming between the *4a* site and the normally vacant site. These octahedral defects are unique and do not suggest a transition to a rock salt phase as was reported for lower energy irradiations. The formed defects resemble the theorized inversion process itself, which may have been frozen in during the rapid quenching[129]. To fully understand the response of the spinel structure to swift heavy ion irradiation, significantly more experimental work is required. The structure appears to have a varied response depending on the ion energy and fluence[170]. At present, the energy of ion that can be used is limited to very high energies to produce enough sample mass for neutron total scattering. The mass requirements, however, are decreasing rapidly as neutron sources become brighter. There is also great potential in performing neutron total scattering at high pressure beamlines which have highly focused neutron beams, further reducing the mass requirements.

The other extreme of interest in geology is high pressure. The field of neutron total scattering *in situ* at high pressure is still actively being developed and experiments are uncommon in literature. In chapter 6, the results of a pilot experiment on total scattering at high pressure using the SNAP instrument at the Spallation Neutron Source are presented. Defect fluorite was used as a model system as its local structure is more distinct in neutron PDF than the local tetragonal spinel structure. The effect of pressure on a local Weberite-type phase in defect fluorite is presented. The local orthorhombic phase prefers to compress

along the B axis under pressure while the long range structure compresses isotropically. Distinguishing the local phase at high pressure, however, was successful and the methods and characteristics of the SNAP instrument are presented in the experimental methods section. The range of pressures at which neutron total scattering is possible is not known as this experiment only compressed to 6 GPa in a Paris Edinburgh cell with single toridal anvils. Pressure will increase as further development is done on total scattering in other high pressure devices, which allow for smaller sample volumes.

At present, even after 110 years of previous work, there is still much to be done to completely understand the spinel structure and the increased availability of intense neutron diffraction beamlines will likely accelerate this process. The work presented in this dissertation is focused on the ionic compounds $MgAl_2O_4$ and $NiAl_2O_4$; however, the family of compounds that can adopt the spinel structure is extremely varied. These compounds can have unique local structures[75] and will most likely display a different behavior when exposed to extreme conditions. Additionally, many of the discrepancies previously reported in physical property measurements has not been reassessed considering the new $P4_122$ local structure, which could be explored with additional modelling work. Most importantly, how this local structure fits in with the larger picture of disordering in rock salt derived oxides is still unknown as many other disordered oxides in neighboring oxides families have not been investigated locally using total scattering.

List of References

1. Zhao, Q.; Yan, Z.; Chen, C.; Chen, J., Spinels: controlled preparation, oxygen reduction/evolution reaction application, and beyond. *Chemical reviews* **2017,** *117* (15), 10121-10211.

2. Cho, Y.; Lee, S.; Lee, Y.; Hong, T.; Cho, J., Spinel-layered core-shell cathode materials for Li-ion batteries. *Advanced Energy Materials* **2011,** *1* (5), 821-828.

3. Sonoyama, N.; Kawamura, K.; Yamada, A.; Kanno, R., Electrochemical luminescence of rare earth metal ion doped MgIn2O4 electrodes. *Journal of the Electrochemical Society* **2006,** *153* (3), H45.

4. Kaczmarczyk, J.; Zasada, F.; Janas, J.; Indyka, P.; Piskorz, W.; Kotarba, A.; Sojka, Z., Thermodynamic stability, redox properties, and reactivity of Mn3O4, Fe3O4, and Co3O4 model catalysts for N2O decomposition: resolving the origins of steady turnover. *ACS Catalysis* **2016,** *6* (2), 1235-1246.

5. Phanichphant, S., Cellulose-precursor synthesis of nanocrystalline Co0. 5Cu0. 5Fe2O4 spinel ferrites. *Materials Research Bulletin* **2012,** *47* (2), 473-477.

6. Belous, A.; Ovchar, O.; Durilin, D.; Krzmanc, M. M.; Valant, M.; Suvorov, D., High-Q microwave dielectric materials based on the spinel Mg2TiO4. *Journal of the American Ceramic Society* **2006,** *89* (11), 3441-3445.

7. Ueda, N.; Omata, T.; Hikuma, N.; Ueda, K.; Mizoguchi, H.; Hashimoto, T.; Kawazoe, H., New oxide phase with wide band gap and high electroconductivity, MgIn2O4. *Applied physics letters* **1992,** *61* (16), 1954-1955.

8. Asif Khan, M.; Sun, C.; Yang, J.; Chen, Q.; Lim, B.; Zubair Anwar, M.; Osinsky, A.; Temkin, H., Cleaved cavity optically pumped InGaN–GaN laser grown on spinel substrates. *Applied physics letters* **1996,** *69* (16), 2418-2420.

9. Wu, J.; Wang, X.; Zheng, W.; Sun, Y.; Xie, Y.; Ma, K.; Zhang, Z.; Liao, Q.; Tian, Z.; Kang, Z., Identifying and interpreting geometric configuration-dependent activity of spinel catalysts for water reduction. *Journal of the American Chemical Society* **2022,** *144* (41), 19163-19172.

10. Garg, R.; Rajagopalan, N.; Pyeon, M.; Goenuellue, Y.; Fischer, T.; Khanna, A. S.; Mathur, S., Plasma CVD grown Al2O3 and MgAl2O4 coatings for corrosion protection applications. *Surface and Coatings Technology* **2018,** *356*, 49-55.

11. Duan, Y.; Li, X.; Sun, N.; Ni, H.; Tkachev, S. N.; Mao, Z., Single-crystal elasticity of MgAl2O4-spinel up to 10.9 GPa and 1000 K: Implication for the velocity structure of the top upper mantle. *Earth and Planetary Science Letters* **2018,** *481*, 41-47.

12. Ball, J. A.; Murphy, S. T.; Grimes, R. W.; Bacorisen, D.; Smith, R.; Uberuaga, B. P.; Sickafus, K. E., Defect processes in MgAl2O4 spinel. *Solid state sciences* **2008,** *10* (6), 717-724.

13. Weeks, R. A.; Sonder, E., Electrical Conductivity of Pure and Fe-Doped Magnesium-Aluminum Spinel. *Journal of the American Ceramic Society* **1980,** *63* (1-2), 92-95.

14. Yamanaka, T.; Takéuchi, Y., Order-disorder transition in MgAl2O4 spinel at high temperatures up to 1700 C. *Zeitschrift für Kristallographie-Crystalline Materials* **1983,** *165* (1-4), 65-78.

15. Peterson, R. C.; Lager, G. A.; Hitterman, R. L., A time-of-flight neutron powder diffraction study of MgAl2O4 at temperatures up to 1273 K. *American Mineralogist* **1991,** *76* (9-10), 1455-1458.

16. O'Neill, H. S. C.; Navrotsky, A., Simple spinels; crystallographic parameters, cation radii, lattice energies, and cation distribution. *The American mineralogist* **1983,** *68* (1-2), 181-194.

17. Laguna-Bercero, M. A.; Sanjuán, M. L.; Merino, R. I., Raman spectroscopic study of cation disorder in poly- and single crystals of the nickel aluminate spinel. *Journal of physics. Condensed matter* **2007,** *19* (18), 186217-186217.

18. Bragg, W. H., The Structure of Magnetite and the Spinels. *Nature* **1915,** *95* (2386), 561-561.

19. Nishikawa, S. H.; Ocirc; Ji, Structure of Some Crystals of Spinel Group. *Tokyo Sugaku-Buturigakkwai Kizi Dai 2 Ki* **1915,** *8* (7), 199-209_1.

20. Sickafus, K. E.; Wills, J. M.; Grimes, N. W., Structure of Spinel. *Journal of the American Ceramic Society* **1999,** *82* (12), 3279-3292.

21. Saberi, A.; Golestani-Fard, F.; Sarpoolaky, H.; Willert-Porada, M.; Gerdes, T.; Simon, R.; Liebscher, C., Development of MgAl2O4 spinel coating on graphite surface to improve its water-wettability and oxidation resistance. *Ceramics international* **2009,** *35* (1), 457-461.

22. Tsai, D.; Wang, C.; Yang, S.; Hsu; SE, Hot isostatic pressing of MgAl2O4 spinel infrared windows. *Material and manufacturing process* **1994,** *9* (4), 709-719.

23. Bocanegra, S. A.; Ballarini, A. D.; Scelza, O. A.; de Miguel, S. R., The influence of the synthesis routes of MgAl2O4 on its properties and behavior as support of dehydrogenation catalysts. *Materials chemistry and physics* **2008,** *111* (2-3), 534-541.

24. Suzuki, I.; Kumazawa, M., Anomalous thermal expansion in spinel MgAl 2 O 4: A possibility for a second order phase transition? *Physics and Chemistry of Minerals* **1980,** *5*, 279-284.

25. Gobbi, G. C.; Christoffersen, R.; Otten, M. T.; Miner, B.; Buseck, P. R.; Kennedy, G. J.; Fyfe, C. A., DIRECT DETERMINATION OF CATION DISORDER IN MgAl2O4 SPINEL BY HIGH-RESOLUTION 27Al MAGIC-ANGLE-SPINNING NMR SPECTROSCOPY. *Chemistry Letters* **1985,** *14* (6), 771-774.

26. Wood, B. J.; Kirkpatrick, R. J.; Montez, B., Order-disorder phenomena in MgAl2O4spinel. *American Mineralogist* **1986,** *71* (7-8), 999-1006.

27. Callen, H. B.; Harrison, S.; Kriessman, C., Cation distributions in ferrospinels. Theoretical. *Physical Review* **1956,** *103* (4), 851.

28. Navrotsky, A.; Kleppa, O., The thermodynamics of cation distributions in simple spinels. *Journal of Inorganic and nuclear Chemistry* **1967,** *29* (11), 2701-2714.

29. Shannon, R., Acta Crystallogr., Sect. A: Cryst. Phys., Diffr., Theor. Gen. Crystallogr. *Acta Crystallogr. Sect. A: Cryst. Phys., Diffr., Theor. Gen. Crystallogr* **1976,** *32*, 751.

30. Redfern, S. A. T.; Harrison, R. J.; O'Neill, H. S. C.; Wood, D. R. R., Thermodynamics and kinetics of cation ordering in MgAl2O4 spinel up to 1600 °C from in situ neutron diffraction. *American Mineralogist* **1999,** *84* (3), 299-310.

31. Schmocker, U.; Waldner, F., The inversion parameter with respect to the space group of MgAl2O4 spinels. *Journal of physics. C, Solid state physics* **1976,** *9*, L235.

32. O'Neil, H. S. C.; Dollase, W. A.; Ross, C. R., Temperature dependence of the cation distribution in nickel aluminate (NiAl2O4) spinel, a powder XRD study. *Physics and chemistry of minerals* **1991,** *18* (5), 302-319.

33. Roelofsen, J. N.; Peterson, R. C.; Raudsepp, M., Structural variation in nickel aluminate spinel (NiAl2O4). *American Mineralogist* **1992,** *77* (5-6), 522-528.

34. Ringwood, A.; Reid, A., Olivine-spinel transformation in MgMnGeO4, FeMnGeO4 and CoMnGeO4. *Journal of Physics and Chemistry of Solids* **1970,** *31* (12), 2791-2793.

35. Liu, L. g., Disproportionation of MgAl2O4 spinel at high pressures and temperatures. *Geophysical Research Letters* **1975,** *2* (1), 9-11.

36. Ringwood, A. E.; Reid, A. F., High pressure transformations of spinels (I). *Earth and Planetary Science Letters* **1968,** *5*, 245-250.

37. Catti, M.; Fava, F. F.; Zicovich, C.; Dovesi, R., High-pressure decomposition of MCr 2 O 4 spinels (M= Mg, Mn, Zn) by ab initio methods. *Physics and Chemistry of Minerals* **1999,** *26*, 389-395.

38. Reid, A.; Ringwood, A., Newly observed high pressure transformations in Mn3O4, CaAl2O4, and ZrSiO4. *Earth and Planetary Science Letters* **1969,** *6* (3), 205-208.

39. Wang, C. y., Constitution of the lower mantle as evidenced from shock wave data for some rocks. *Journal of Geophysical Research* **1968,** *73* (20), 6459-6476.

40. Liu, L.-G., A new high-pressure phase of spinel. *Earth and Planetary Science Letters* **1978,** *41* (4), 398-404.

41. Irifune, T.; Fujino, K.; Ohtani, E., A new high-pressure form of MgAl2O4. *Nature* **1991,** *349* (6308), 409-411.

42. Finger, L. W.; Hazen, R. M.; Hofmeister, A. M., High-pressure crystal chemistry of spinel (MgAl2O4) and magnetite (Fe3O4): comparisons with silicate spinels. *Physics and Chemistry of Minerals* **1986,** *13* (4), 215-220.

43. Pavese, A.; Artioli, G.; Hull, S., In situ powder neutron diffraction of cation partitioning vs. pressure in Mg0. 94Al2. 04O4 synthetic spinel. *American Mineralogist* **1999,** *84* (5-6), 905-912.

44. Levy, D.; Pavese, A.; Hanfland, M., Synthetic MgAl2O4 (spinel) at high-pressure conditions (0.0001–30 GPa): A synchrotron X-ray powder diffraction study. *American Mineralogist* **2003,** *88* (1), 93-98.

45. Kudoh, Y.; Kuribayashi, T.; Mizobata, H.; Ohtani, E.; Sasaki, S.; Tanaka, M., Pressure dependence of u parameter in ringwoodite up to 7.9 GPa. *Journal of Mineralogical and Petrological Sciences* **2007,** *102* (1), 8-11.

46. Nestola, F.; Boffa Ballaran, T.; Balic-Zunic, T.; Princivalle, F.; Secco, L.; Dal Negro, A., Comparative compressibility and structural behavior of spinel MgAl2O4 at high pressures: The independency on the degree of cation order. *American Mineralogist* **2007,** *92* (11-12), 1838-1843.

47. Méducin, F.; Redfern, S. A.; Le Godec, Y.; Stone, H. J.; Tucker, M. G.; Dove, M. T.; Marshall, W. G., Study of cation order-disorder in MgAl2O4 spinel by in situ

neutron diffraction up to 1600 K and 3.2 GPa. *American Mineralogist* **2004,** *89* (7), 981-986.

48. Hurley, G. F.; Bunch, J. M., Swelling and thermal diffusivity changes in neutron-irradiated ceramics. *Am. Ceram. Soc. Bull.; (United States)* **1980,** *59:4*, Medium: X; Size: Pages: 456-458 2009-12-16.

49. Hurley, G. F.; Kennedy, J. C.; Clinard, F. W.; Youngman, R. A.; McDonell, W. R., Structural properties of MgO AND MgAl2O4, after fission neutron irradiation near room temperature. *Journal of Nuclear Materials* **1981,** *103*, 761-765.

50. Clinard Jr, F.; Hurley, G.; Hobbs, L., Neutron irradiation damage in MgO, Al2O3 and MgAl2O4 ceramics. *Journal of Nuclear Materials* **1982,** *108*, 655-670.

51. Sickafus, K.; Larson, A.; Yu, N.; Nastasi, M.; Hollenberg, G.; Garner, F.; Bradt, R., Cation disorder in high dose, neutron-irradiated spinel. *Journal of Nuclear Materials* **1995,** *219*, 128-134.

52. Yu, N.; Sickafus, K. E.; Nastasi, M., First observation of'amorphization in single-crystal MgA12O4 spinel. *Philosophical magazine letters* **1994,** *70* (4), 235-240.

53. Devanathan, R.; Sickafus, K. E.; Yu, N.; Nastasi, M., Structure of the metastable state in ion-irradiated magnesio-aluminate spinel. *Philosophical magazine letters* **1995,** *72* (3), 155-161.

54. Sickafus, K. E.; Yu, N.; Nastasi, M., Radiation resistance of the oxide spinel: the role of stoichiometry on damage response. *Nuclear Instruments and Methods in Physics Research Section B: Beam Interactions with Materials and Atoms* **1996,** *116* (1), 85-91.

55. Ishimaru, M.; Afanasyev-Charkin, I. V.; Sickafus, K. E., Ion-beam-induced spinel-to-rocksalt structural phase transformation in MgAl 2 O 4. *Applied Physics Letters* **2000,** *76* (18), 2556-2558.

56. Chauvin, N.; Albiol, T.; Mazoyer, R.; Noirot, J.; Lespiaux, D.; Dumas, J.; Weinberg, C.; Menard, J.; Ottaviani, J., In-pile studies of inert matrices with emphasis on magnesia and magnesium aluminate spinel. *Journal of Nuclear Materials* **1999,** *274* (1-2), 91-97.

57. Nordlund, K.; Zinkle, S. J.; Sand, A. E.; Granberg, F.; Averback, R. S.; Stoller, R. E.; Suzudo, T.; Malerba, L.; Banhart, F.; Weber, W. J., Primary radiation damage: A review of current understanding and models. *Journal of Nuclear Materials* **2018,** *512*, 450-479.

58. Duffy, D.; Daraszewicz, S.; Mulroue, J., Modelling the effects of electronic excitations in ionic-covalent materials. *Nuclear Instruments and Methods in Physics Research Section B: Beam Interactions with Materials and Atoms* **2012,** *277*, 21-27.

59. Tracy, C. L.; Lang, M.; Zhang, F.; Trautmann, C.; Ewing, R. C., Phase transformations in Ln 2 O 3 materials irradiated with swift heavy ions. *Physical Review B* **2015,** *92* (17), 174101.

60. Afra, B.; Rodriguez, M.; Trautmann, C.; Pakarinen, O.; Djurabekova, F.; Nordlund, K.; Bierschenk, T.; Giulian, R.; Ridgway, M. C.; Rizza, G., SAXS investigations of the morphology of swift heavy ion tracks in α-quartz. *Journal of Physics: Condensed Matter* **2012,** *25* (4), 045006.

61. Wiss, T.; Matzke, H., Heavy ion induced damage in MgAl2O4, an inert matrix candidate for the transmutation of minor actinides. *Radiation Measurements* **1999,** *31* (1), 507-514.

62. Zinkle, S.; Skuratov, V., Track formation and dislocation loop interaction in spinel irradiated with swift heavy ions. *Nuclear Instruments and Methods in Physics Research Section B: Beam Interactions with Materials and Atoms* **1998,** *141* (1-4), 737-746.

63. Yasuda, K.; Yamamoto, T.; Shimada, M.; Matsumura, S.; Chimi, Y.; Ishikawa, N., Atomic structure and disordering induced by 350áMeV Au ions in MgAl2O4. *Nuclear Instruments and Methods in Physics Research Section B: Beam Interactions with Materials and Atoms* **2006,** *250* (1-2), 238-244.

64. Simeone, D.; Dodane-Thiriet, C.; Gosset, D.; Daniel, P.; Beauvy, M., Order–disorder phase transition induced by swift ions in MgAl2O4 and ZnAl2O4 spinels. *Journal of Nuclear Materials* **2002,** *300* (2), 151-160.

65. Sickafus, K. E., Comment on 'Order–disorder phase transition induced by swift ions in MgAl2O4 and ZnAl2O4 spinels' by D. Simeone et al., J. Nucl. Mater. 300 (2002) 151–160. *Journal of nuclear materials* **2003,** *312* (1), 111-123.

66. Baldinozzi, G.; Simeone, D.; Gosset, D.; Surblé, S.; Mazérolles, L.; Thomé, L., Why ion irradiation does not lead to the same structural changes in normal spinels ZnAl2O4, MgAl2O4 and MgCr2O4? *Nuclear Instruments and Methods in Physics Research Section B: Beam Interactions with Materials and Atoms* **2008,** *266* (12-13), 2848-2853.

67. Preudhomme, J.; Tarte, P., Studies of spinels. VII. Order-disorder transition in the inverse germanate spinels Zn2− x (Co, Ni) xGeO4 (x≃ 1). *Journal of Solid State Chemistry* **1980,** *35* (2), 272-277.

68. Hardy, A.; Lecerf, A.; Rault, M.; Villiers, G., Preparation, crystal, and magnetic properties of manganese orthotitanate Mn2TiO4. *CR Acad. Sci. Paris* **1964,** *259*, 3462-3465.

69. Ivanov, V. G.; Abrashev, M. V.; Iliev, M. N.; Gospodinov, M. M.; Meen, J.; Aroyo, M. I., Short-rangeB-site ordering in the inverse spinel ferriteNiFe2O4. *Physical review. B, Condensed matter and materials physics* **2010,** *82* (2), 024104.

70. Stevanović, V.; d'Avezac, M.; Zunger, A., Universal Electrostatic Origin of Cation Ordering in A2BO4 Spinel Oxides. *Journal of the American Chemical Society* **2011,** *133* (30), 11649-11654.

71. O'Quinn, E. C.; Shamblin, J.; Perlov, B.; Ewing, R. C.; Neuefeind, J.; Feygenson, M.; Gussev, I.; Lang, M., Inversion in Mg1–xNixAl2O4 Spinel: New Insight into Local Structure. *Journal of the American Chemical Society* **2017,** *139* (30), 10395-10402.

72. Yoshioka, S.; Yasuda, K.; Matsumura, S.; Sugiyama, T.; Kobayashi, E., Transition of Cationic Local Structures in Mg1-xNixAl2O4. *The Journal of Physical Chemistry C* **2021,** *125* (9), 5269-5277.

73. Pauling, L., THE PRINCIPLES DETERMINING THE STRUCTURE OF COMPLEX IONIC CRYSTALS. *Journal of the American Chemical Society* **1929,** *51* (4), 1010-1026.

74. O'Quinn, E. C.; Sickafus, K. E.; Ewing, R. C.; Baldinozzi, G.; Neuefeind, J. C.; Tucker, M. G.; Fuentes, A. F.; Drey, D.; Lang, M. K., Predicting short-range order and correlated phenomena in disordered crystalline materials. *Science Advances* **2020,** *6* (35), eabc2758.

75. Liu, J.; Wang, X.; Borkiewicz, O. J.; Hu, E.; Xiao, R.-J.; Chen, L.; Page, K., Unified View of the Local Cation-Ordered State in Inverse Spinel Oxides. *Inorganic chemistry* **2019,** *58* (21), 14389-14402.

76. Elias, I.; Soon, A.; Huang, J.; S. Haynes, B.; Montoya, A., Atomic order, electronic structure and thermodynamic stability of nickel aluminate. *Physical Chemistry Chemical Physics* **2019,** *21* (47), 25952-25961.

77. Hirtz, J.; O'Quinn, E. C.; Gussev, I. M.; Neuefeind, J. C.; Lang, M., Cation Short-Range Ordering of MgAl2O4 and NiAl2O4 Spinel Oxides at High Temperatures via In Situ Neutron Total Scattering. *Inorganic Chemistry* **2022,** *61* (42), 16822-16830.

78. Jacob, K.; Alcock, C., Activities and their relation to cation distribution in NiAl2O4-MgAl2O4 spinel solid solutions. *Journal of Solid State Chemistry* **1977,** *20* (1), 79-88.

79. Porta, P.; Stone, F.; Turner, R., The distribution of nickel ions among octahedral and tetrahedral sites in NiAl2O4-MgAl2O4 solid solutions. *Journal of Solid State Chemistry* **1974,** *11* (2), 135-147.

80. Zhang, Y.; Eremenko, M.; Krayzman, V.; Tucker, M. G.; Levin, I., New capabilities for enhancement of RMCProfile: instrumental profiles with arbitrary peak

shapes for structural refinements using the reverse Monte Carlo method. *Applied Crystallography* **2020,** *53* (6), 1509-1518.

81. Tucker, M. G.; Keen, D. A.; Dove, M. T.; Goodwin, A. L.; Hui, Q., RMCProfile: reverse Monte Carlo for polycrystalline materials. *Journal of Physics: Condensed Matter* **2007,** *19* (33), 335218.

82. Egami, T.; Billinge, S. J., *Underneath the Bragg peaks: structural analysis of complex materials*. Newnes: 2012; Vol. 16.

83. Lorch, E., Neutron diffraction by germania, silica and radiation-damaged silica glasses. *Journal of Physics C: Solid State Physics* **1969,** *2* (2), 229.

84. Neuefeind, J.; Feygenson, M.; Carruth, J.; Hoffmann, R.; Chipley, K. K., The Nanoscale Ordered MAterials Diffractometer NOMAD at the Spallation Neutron Source SNS. *Nuclear Instruments and Methods in Physics Research Section B: Beam Interactions with Materials and Atoms* **2012,** *287*, 68-75.

85. Ziegler, J. F.; Ziegler, M. D.; Biersack, J. P., SRIM–The stopping and range of ions in matter (2010). *Nuclear Instruments and Methods in Physics Research Section B: Beam Interactions with Materials and Atoms* **2010,** *268* (11-12), 1818-1823.

86. Rietveld, H. M., The Rietveld method. *Physica Scripta* **2014,** *89* (9), 098002.

87. Toby, B. H.; Von Dreele, R. B., GSAS-II: the genesis of a modern open-source all purpose crystallography software package. *Journal of Applied Crystallography* **2013,** *46* (2), 544-549.

88. Farrow, C. L.; Juhas, P.; Liu, J. W.; Bryndin, D.; Božin, E. S.; Bloch, J.; Proffen, T.; Billinge, S. J. L., PDFfit2 and PDFgui: computer programs for studying nanostructure in crystals. *Journal of Physics: Condensed Matter* **2007,** *19* (33), 335219.

89. Bragg, W. H., XXX. The structure of the spinel group of crystals. *The London, Edinburgh, and Dublin Philosophical Magazine and Journal of Science* **1915,** *30* (176), 305-315.

90. Nishikawa, S., Structure of some crystals of spinel group. *Proceedings of the Tokyo Mathematico-Physical Society. 2nd Series* **1915,** *8* (7), 199-209_1.

91. Peters, J.; Standley, K. J., The Dielectric Behaviour of Magnesium Manganese Ferrite. *Proceedings of the Physical Society* **1958,** *71* (1), 131.

92. Lotgering, F. K., Ferromagnetism in spinels: CuCr2S4 and CuCr2Se4. *Solid State Communications* **1964,** *2* (2), 55-56.

93. Callen, E., Magnetic Properties of Magnetite. *Physical Review* **1966,** *150* (2), 367-376.

94. Grimes, N.; Collett, A., Correlation of Infra-Red Spectra with Structural Distortions in the Spinel Series Mg (CrxAl2− x) O4. *physica status solidi (b)* **1971,** *43* (2), 591-599.

95. Henning, J.; Van den Boom, H., ESR Investigations of Nearest-Neighbor Cr 3+-Cr 3+ Interactions in Cr-Doped Spinel Mg Al 2 O 4. *Physical Review B* **1973,** *8* (5), 2255.

96. Hwang, L.; Heuer, A.; Mitchell, T., On the space group of MgAl2O4 spinel. *Philosophical Magazine* **1973,** *28* (1), 241-243.

97. Heuer, A. H.; Mitchell, T. E., Further discussion on the space group of spinel. *Journal of Physics C: Solid State Physics* **1975,** *8* (23), L541.

98. Mishra, R.; Thomas, G., Structural phase transition in the spinel MgA12O4. *Foundations of Crystallography* **1977,** *33* (4), 678-678.

99. Tokonami, M.; Horiuchi, H., On the space group of spinel, MgAl2O4. *Acta Crystallographica Section A* **1980,** *36* (1), 122-126.

100. Smith, P. P. K., Note on the space group of spinel minerals. *Philosophical Magazine B* **1978,** *38* (1), 99-102.

101. Rouse, K. D.; Thomas, M. W.; Willis, B. T. M., Space group of the spinel structure: A neutron diffraction study of MgAl2O4. *Journal of Physics C: Solid State Physics* **1976,** *9* (9), L231.

102. Samuelsen, E. J., Note on the space group of magnetite. *Journal of Physics C: Solid State Physics* **1974,** *7* (7), L115.

103. Samuelsen, E. J.; Steinsvoll, O., On the space group of spinel. *Journal of Physics C: Solid State Physics* **1975,** *8* (21), L427.

104. Zhang, L.; Ji, G.-F.; Zhao, F.; Meng, C.-M.; Wei, D.-Q., The first-principle studies of the crystal phase transitions: Fd3m-MgAl2O4→F4-3m-MgAl2O4. *Physica B: Condensed Matter* **2011,** *406* (3), 335-338.

105. Ye, F.; Liu, Y.; Whitfield, R.; Osborn, R.; Rosenkranz, S., Implementation of cross correlation for energy discrimination on the time-of-flight spectrometer CORELLI. *Applied Crystallography* **2018,** *51* (2), 315-322.

106. Toby, B. H.; Von Dreele, R. B., GSAS-II: the genesis of a modern open-source all purpose crystallography software package. *Applied Crystallography* **2013,** *46* (2), 544-549.

107. O'Quinn, E. C.; Shamblin, J.; Perlov, B.; Ewing, R. C.; Neuefeind, J.; Feygenson, M.; Gussev, I.; Lang, M., Inversion in Mg1–x Ni x Al2O4 Spinel: New insight into local structure. *Journal of the American Chemical Society* **2017,** *139* (30), 10395-10402.

108. Schmocker, U.; Waldner, F., The inversion parameter with respect to the space group of MgAl2O4 spinels. *Journal of Physics C: Solid State Physics* **1976,** *9* (9), L235.

109. Nield, V. M.; Keen, D. A., *Diffuse neutron scattering from crystalline materials*. Oxford University Press: 2001; Vol. 14.

110. Dove, M. T.; Tucker, M. G.; Keen, D. A., Neutron total scattering method: simultaneous determination of long-range and short-range order in disordered materials. *European Journal of Mineralogy* **2002,** *14* (2), 331-348.

111. Gibbs, G. V.; Ross, N. L.; Cox, D. F.; Rosso, K. M., Insights into the crystal chemistry of Earth materials rendered by electron density distributions: Pauling's rules revisited. *American Mineralogist* **2014,** *99* (5-6), 1071-1084.

112. Brown, I. D., Recent Developments in the Methods and Applications of the Bond Valence Model. *Chemical Reviews* **2009,** *109* (12), 6858-6919.

113. Pauling, L., Atomic Radii and Interatomic Distances in Metals. *Journal of the American Chemical Society* **1947,** *69* (3), 542-553.

114. Hill, R. J.; Craig, J. R.; Gibbs, G. V., Systematics of the spinel structure type. *Physics and Chemistry of Minerals* **1979,** *4* (4), 317-339.

115. Guo, J.; Lou, H.; Zhao, H.; Wang, X.; Zheng, X., Novel synthesis of high surface area MgAl2O4 spinel as catalyst support. *Materials Letters* **2004,** *58* (12-13), 1920-1923.

116. Thackeray, M. M., Exploiting the spinel structure for Li-ion battery applications: a tribute to John B. Goodenough. *Advanced Energy Materials* **2021,** *11* (2), 2001117.

117. L. Thomé, A. G., J. Jagielski, F. Garrido, T. Thomé, Radiation stability of ceramics: Test cases of zirconia and spinel. *Vacuum* **2007,** *81* (10), 1264-1270.

118. Uberuaga, B. P.; Tang, M.; Jiang, C.; Valdez, J. A.; Smith, R.; Wang, Y.; Sickafus, K. E., Opposite correlations between cation disordering and amorphization resistance in spinels versus pyrochlores. *Nature Communications* **2015,** *6* (1), 8750.

119. Clinard, F. W.; Dienst, W.; Farnum, E. H., Issues related to mechanical properties of neutron-irradiated ceramics. *Journal of Nuclear Materials* **1994,** *212-215*, 1075-1080.

120. Ohzuku, T.; Ueda, A.; Yamamoto, N., Zero-strain insertion material of Li [Li1/3Ti5/3] O 4 for rechargeable lithium cells. *Journal of the Electrochemical Society* **1995,** *142* (5), 1431.

121. Itoh, N.; Duffy, D.; Khakshouri, S.; Stoneham, A., Making tracks: electronic excitation roles in forming swift heavy ion tracks. *Journal of Physics: Condensed Matter* **2009,** *21* (47), 474205.

122. Pellerin, N.; Dodane-Thiriet, C.; Montouillout, V.; Beauvy, M.; Massiot, D., Cation sublattice disorder induced by swift heavy ions in MgAl2O4 and ZnAl2O4 spinels: 27Al solid-state NMR study. *The Journal of Physical Chemistry B* **2007,** *111* (44), 12707-12714.

123. Gussev, I. M.; O'Quinn, E. C.; Tucker, M.; Ewing, R. C.; Overstreet, C.; Neuefeind, J.; Everett, M.; Zhang, Q.; Sprouster, D.; Olds, D., Systematic study of short- and long-range correlations in RE 3 TaO 7 weberite-type compounds by neutron total

scattering and X-ray diffraction. *Journal of Materials Chemistry A* **2023,** *11* (16), 8886-8903.

124. Momma, K.; Izumi, F., VESTA: a three-dimensional visualization system for electronic and structural analysis. *Applied Crystallography* **2008,** *41* (3), 653-658.

125. Gosset, D.; Simeone, D.; Dutheil, M.; Bouffard, S.; Beauvy, M., Structural evolutions of spinels under ions irradiations. *Journal of the European Ceramic Society* **2005,** *25* (12), 2677-2681.

126. Simeone, D.; Dodane-Thiriet, C.; Gosset, D.; Daniel, P.; Beauvy, M., Order–disorder phase transition induced by swift ions in MgAl2O4 and ZnAl2O4 spinels. *Journal of nuclear materials* **2002,** *300* (2-3), 151-160.

127. Yasuda, K.; Yamamoto, T.; Etoh, M.; Kawasoe, S.; Matsumura, S.; Ishikawa, N., Accumulation of radiation damage and disordering in MgAl2O4 under swift heavy ion irradiation: Dedicated to Prof. Dr.-Ing. Heinrich Wollenberger on the occasion of his 80th birthday. *International journal of materials research* **2011,** *102* (9), 1082-1088.

128. Lang, M.; Devanathan, R.; Toulemonde, M.; Trautmann, C., Advances in understanding of swift heavy-ion tracks in complex ceramics. *Current Opinion in Solid State and Materials Science* **2015,** *19* (1), 39-48.

129. Restrepo, O. A.; Arnache, Ó.; Mousseau, N., An approach to understanding the formation mechanism of NiFe2O4 inverse spinel. *Materialia* **2024,** *33*, 102031.

130. Le Godec, Y.; Courac, A.; Solozhenko, V. L., High-pressure synthesis of superhard and ultrahard materials. *Journal of Applied Physics* **2019,** *126* (15), 151102.

131. Flores-Livas, J. A.; Boeri, L.; Sanna, A.; Profeta, G.; Arita, R.; Eremets, M., A perspective on conventional high-temperature superconductors at high pressure: Methods and materials. *Physics Reports* **2020,** *856*, 1-78.

132. Eremets, M. I.; Gavriliuk, A. G.; Trojan, I. A.; Dzivenko, D. A.; Boehler, R., Single-bonded cubic form of nitrogen. *Nature materials* **2004,** *3* (8), 558-563.

133. Zhang, L.; Wang, Y.; Lv, J.; Ma, Y., Materials discovery at high pressures. *Nature Reviews Materials* **2017,** *2* (4), 17005.

134. Chapman, K. W.; Chupas, P. J.; Halder, G. J.; Hriljac, J. A.; Kurtz, C.; Greve, B. K.; Ruschman, C. J.; Wilkinson, A. P., Optimizing high-pressure pair distribution function measurements in diamond anvil cells. *Journal of Applied Crystallography* **2010,** *43* (2), 297-307.

135. Shen, G.; Mao, H. K., High-pressure studies with x-rays using diamond anvil cells. *Reports on Progress in Physics* **2017,** *80* (1), 016101.

136. Goncharov, A. F., Raman Spectroscopy at High Pressures. *International Journal of Spectroscopy* **2012,** *2012* (1), 617528.

137. Hemley, R.; Goncharov, A.; Lu, R.; Struzhkin, V.; Li, M.; Mao, H., High-pressure synchrotron infrared spectroscopy at the National Synchrotron Light Source. *Il Nuovo Cimento D* **1998,** *20*, 539-551.

138. Charles, D. S.; Feygenson, M.; Page, K.; Neuefeind, J.; Xu, W.; Teng, X., Structural water engaged disordered vanadium oxide nanosheets for high capacity aqueous potassium-ion storage. *Nature Communications* **2017,** *8* (1), 15520.

139. Wang, H.-W.; Naguib, M.; Page, K.; Wesolowski, D. J.; Gogotsi, Y., Resolving the Structure of Ti3C2Tx MXenes through Multilevel Structural Modeling of the Atomic Pair Distribution Function. *Chemistry of Materials* **2016,** *28* (1), 349-359.

140. Shamblin, J.; Feygenson, M.; Neuefeind, J.; Tracy, C. L.; Zhang, F.; Finkeldei, S.; Bosbach, D.; Zhou, H.; Ewing, R. C.; Lang, M., Probing disorder in isometric pyrochlore and related complex oxides. *Nature Materials* **2016,** *15* (5), 507-511.

141. Fitzgibbons, T. C.; Guthrie, M.; Xu, E.-s.; Crespi, V. H.; Davidowski, S. K.; Cody, G. D.; Alem, N.; Badding, J. V., Benzene-derived carbon nanothreads. *Nature Materials* **2015,** *14* (1), 43-47.

142. Cao, B.; Veith, G. M.; Neuefeind, J. C.; Adzic, R. R.; Khalifah, P. G., Mixed Close-Packed Cobalt Molybdenum Nitrides as Non-noble Metal Electrocatalysts for the Hydrogen Evolution Reaction. *Journal of the American Chemical Society* **2013,** *135* (51), 19186-19192.

143. Rong, X.; Liu, J.; Hu, E.; Liu, Y.; Wang, Y.; Wu, J.; Yu, X.; Page, K.; Hu, Y.-S.; Yang, W.; Li, H.; Yang, X.-Q.; Chen, L.; Huang, X., Structure-Induced Reversible Anionic Redox Activity in Na Layered Oxide Cathode. *Joule* **2018,** *2* (1), 125-140.

144. Besson, J. M.; Nelmes, R. J.; Hamel, G.; Loveday, J. S.; Weill, G.; Hull, S., Neutron powder diffraction above 10 GPa. *Physica B: Condensed Matter* **1992,** *180-181*, 907-910.

145. Klotz, S.; Hamel, G.; Loveday, J.; Nelmes, R.; Guthrie, M.; Soper, A., Structure of high-density amorphous ice under pressure. *Physical review letters* **2002,** *89* (28), 285502.

146. Salmon, P. S.; Drewitt, J. W.; Whittaker, D. A.; Zeidler, A.; Wezka, K.; Bull, C. L.; Tucker, M. G.; Wilding, M. C.; Guthrie, M.; Marrocchelli, D., Density-driven structural transformations in network forming glasses: a high-pressure neutron diffraction study of GeO2 glass up to 17.5 GPa. *Journal of Physics: Condensed Matter* **2012,** *24* (41), 415102.

147. Drewitt, J. W.; Salmon, P. S.; Barnes, A. C.; Klotz, S.; Fischer, H. E.; Crichton, W. A., Structure of GeO 2 glass at pressures up to 8.6 GPa. *Physical Review B—Condensed Matter and Materials Physics* **2010,** *81* (1), 014202.

148. Salmon, P. S.; Zeidler, A., Networks under pressure: the development of in situ high-pressure neutron diffraction for glassy and liquid materials. *Journal of Physics: Condensed Matter* **2015,** *27* (13), 133201.

149. Playford, H. Y.; Tucker, M. G.; Bull, C. L., Neutron total scattering of crystalline materials in the gigapascal regime. *Applied Crystallography* **2017,** *50* (1), 87-95.

150. Klotz, S.; Strässle, T.; Saitta, A.; Rousse, G.; Hamel, G.; Nelmes, R.; Loveday, J.; Guthrie, M., In situ neutron diffraction studies of high density amorphous ice under pressure. *Journal of Physics: Condensed Matter* **2005,** *17* (11), S967.

151. Strässle, T.; Saitta, A.; Godec, Y. L.; Hamel, G.; Klotz, S.; Loveday, J.; Nelmes, R., Structure of dense liquid water by neutron scattering to 6.5 GPa and 670 K. *Physical review letters* **2006,** *96* (6), 067801.

152. Guthrie, M.; Tulk, C. A.; Molaison, J.; dos Santos, A. M., Local structural motifs and extended-range order in liquid and solid ammonia under pressure. *Physical Review B—Condensed Matter and Materials Physics* **2012,** *85* (18), 184205.

153. Zeidler, A.; Wezka, K.; Rowlands, R. F.; Whittaker, D. A.; Salmon, P. S.; Polidori, A.; Drewitt, J. W.; Klotz, S.; Fischer, H. E.; Wilding, M. C., High-pressure transformation of SiO 2 glass from a tetrahedral to an octahedral network: A joint approach using neutron diffraction and molecular dynamics. *Physical review letters* **2014,** *113* (13), 135501.

154. Wezka, K.; Salmon, P. S.; Zeidler, A.; Whittaker, D. A. J.; Drewitt, J. W. E.; Klotz, S.; Fischer, H. E.; Marrocchelli, D., Mechanisms of network collapse in GeO2 glass: high-pressure neutron diffraction with isotope substitution as arbitrator of competing models. *Journal of Physics: Condensed Matter* **2012,** *24* (50), 502101.

155. Wezka, K.; Bouzid, A.; Pizzey, K. J.; Salmon, P. S.; Zeidler, A.; Klotz, S.; Fischer, H. E.; Bull, C. L.; Tucker, M. G.; Boero, M., Density-driven defect-mediated network collapse of GeSe 2 glass. *Physical Review B* **2014,** *90* (5), 054206.

156. Bouzid, A.; Pizzey, K. J.; Zeidler, A.; Ori, G.; Boero, M.; Massobrio, C.; Klotz, S.; Fischer, H. E.; Bull, C. L.; Salmon, P. S., Pressure-induced structural changes in the network-forming isostatic glass GeSe 4: An investigation by neutron diffraction and first-principles molecular dynamics. *Physical Review B* **2016,** *93* (1), 014202.

157. Khanna, A.; Kaur, A.; Tyagi, S.; Funnell, N. P.; Bull, C. L., In situ high pressure neutron diffraction and Raman spectroscopy of 20BaO–80TeO 2 glass. *RSC advances* **2020,** *10* (69), 42502-42511.

158. Gammond, L. V.; Zeidler, A.; Youngman, R. E.; Fischer, H. E.; Bull, C. L.; Salmon, P. S., Transformations to the aluminum coordination environment and network

polymerization in amorphous aluminosilicates under pressure. *The Journal of Chemical Physics* **2024,** *161* (7).

159. Mohammadi, H.; Zeidler, A.; Youngman, R. E.; Fischer, H. E.; Salmon, P. S., Pressure dependent structure of amorphous magnesium aluminosilicates: The effect of replacing magnesia by alumina at the enstatite composition. *The Journal of Chemical Physics* **2024,** *160* (6).

160. Poulsen, F. W.; Glerup, M.; Holtappels, P., Structure, Raman spectra and defect chemistry modelling of conductive pyrochlore oxides. *Solid State Ionics* **2000,** *135* (1), 595-602.

161. Glerup, M.; Nielsen, O. F.; Poulsen, F. W., The Structural Transformation from the Pyrochlore Structure, A2B2O7, to the Fluorite Structure, AO2, Studied by Raman Spectroscopy and Defect Chemistry Modeling. *Journal of Solid State Chemistry* **2001,** *160* (1), 25-32.

162. Blanchard, P. E. R.; Clements, R.; Kennedy, B. J.; Ling, C. D.; Reynolds, E.; Avdeev, M.; Stampfl, A. P. J.; Zhang, Z.; Jang, L.-Y., Does Local Disorder Occur in the Pyrochlore Zirconates? *Inorganic Chemistry* **2012,** *51* (24), 13237-13244.

163. Arnold, O.; Bilheux, J. C.; Borreguero, J. M.; Buts, A.; Campbell, S. I.; Chapon, L.; Doucet, M.; Draper, N.; Ferraz Leal, R.; Gigg, M. A.; Lynch, V. E.; Markvardsen, A.; Mikkelson, D. J.; Mikkelson, R. L.; Miller, R.; Palmen, K.; Parker, P.; Passos, G.; Perring, T. G.; Peterson, P. F.; Ren, S.; Reuter, M. A.; Savici, A. T.; Taylor, J. W.; Taylor, R. J.; Tolchenov, R.; Zhou, W.; Zikovsky, J., Mantid—Data analysis and visualization package for neutron scattering and μ SR experiments. *Nuclear Instruments*

and Methods in Physics Research Section A: Accelerators, Spectrometers, Detectors and Associated Equipment **2014,** *764*, 156-166.

164. Salmon, P. S.; Zeidler, A.; Fischer, H. E., Optimizing the counting times for sample-in-container scattering experiments. *Journal of Applied Crystallography* **2016,** *49* (6), 2249-2251.

165. Herlihy, A.; Geddes, H. S.; Sosso, G. C.; Bull, C. L.; Ridley, C. J.; Goodwin, A. L.; Senn, M. S.; Funnell, N. P., Recovering local structure information from high-pressure total scattering experiments. *Journal of Applied Crystallography* **2021,** *54* (6), 1546-1554.

166. Singh, A. K., X-ray diffraction from solids under nonhydrostatic compression—some recent studies. *Journal of Physics and Chemistry of Solids* **2004,** *65* (8-9), 1589-1596.

167. Ikeda, S.; Carpenter, J. M., Wide-energy-range, high-resolution measurements of neutron pulse shapes of polyethylene moderators. *Nuclear Instruments and Methods in Physics Research Section A: Accelerators, Spectrometers, Detectors and Associated Equipment* **1985,** *239* (3), 536-544.

168. Li, H.; Tao, Q.; Li, N.; Tang, R.; Zhao, Y.; Zhu, H.; Zhu, P.; Wang, X., Pressure-induced structural transition of Y2Zr2O7. *Journal of Alloys and Compounds* **2016,** *660*, 446-449.

169. Keen, D. A., Total scattering and the pair distribution function in crystallography. *Crystallography Reviews* **2020,** *26* (3), 143-201.

170. Beauvy, M.; Dalmasso, C.; Thiriet-Dodane, C.; Simeone, D.; Gosset, D., Damages in ceramics for nuclear waste transmutation by irradiation with swift heavy ions.

Nuclear Instruments and Methods in Physics Research Section B: Beam Interactions with Materials and Atoms **2006,** *242* (1), 557-561.

Vita

John Michael Hirtz was born on February 2nd, 1997, in Oak Ridge, Tennessee. He has remained in East Tennessee and attended Farragut High School, graduating in 2015. After graduation, he attended the University of Tennessee where he completed a Bachelor of Science (B.S.) degree in Nuclear Engineering in 2019. As an undergraduate student John joined Dr. Maik Lang's research group as an undergraduate research assistant. Following graduation, John immediately started as a graduate research assistant in Dr. Lang's group while working towards his Doctor of Philosophy (PhD) degree in Nuclear Engineering, which was completed in 2025. During his graduate work John authored and coauthored multiple peer reviewed publications.